

Comprehensive Review about Methane Adsorption in Shale Nanoporous Media

Wanyang Pang, Yingnan Wang, and Zhehui Jin*

Cite This: *Energy Fuels* 2021, 35, 8456–8493

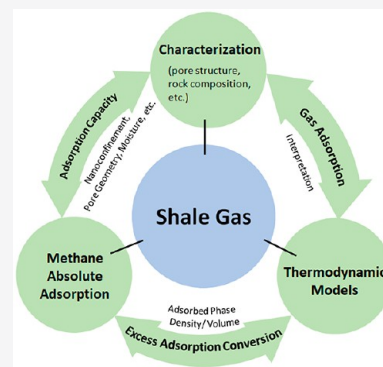
Read Online

ACCESS |

Metrics & More

Article Recommendations

ABSTRACT: Shale/tight gas plays an increasingly important role to meet the growing global energy demand and reduce carbon emissions. Unlike conventional reservoirs, shale formations are subject to rock heterogeneity and have pore size distributions ranging from sub-1 nm to a few micrometers. Thanks to the large number of nanosized pores, adsorbed methane capacity plays a dominant role in total shale gas-in-place. Methane adsorption behaviors can vary drastically in micropores and mesopores, and rock surface type may also greatly affect its adsorption. In this review, we provide a systematic discussion on measurements of shale rock properties including rock compositions and pore structures such as specific surface area (SSA) and pore size distribution (PSD), which are important parameters for methane adsorption in shale nanoporous media. We also provide in-depth discussions on experimental measurements on methane (excess) adsorption in shale nanoporous media, methane adsorption behavior characterization based on molecular simulations, and various excess-adsorption-to-absolute-adsorption conversion methods. We pay particular attention to the assumptions and working mechanisms proposed in various interpretation methods which are embedded in pore structures (SSA and PSD) and absolute adsorption characterizations. In the end, we summarize the key challenges in the methane adsorption characterization in shale media.



1. INTRODUCTION

As a relatively clean energy source compared to coal, natural gas has become an important building block to reduce carbon emissions.¹ The demand for natural gas has gradually increased in the past several decades, accounting for 24% of global energy consumption in 2018.² Thanks to the technological advancements such as hydraulic and horizontal fracturings,^{3,4} unconventional natural gas production from tight/shale formations plays a vital role in achieving energy security and reducing air pollution.⁵ In 2015, the Energy Information Administration (EIA) estimated that the technically recoverable shale/tight gas amount can be up to 215 trillion cubic meters (tcm).⁶ The United States (U.S.) is one of the global leaders in shale gas development with its shale gas production reaching 0.716 tcm in 2019, accounting for 75% of total U.S. dry natural gas production in the same year.⁷ Thanks to the shale/tight gas development, by 2017, the U.S. has become a net natural gas exporting country, and by 2050, U.S. shale gas production could account for more than 90% of its total dry natural gas production.⁷ On the other hand, China has the largest technically recoverable shale gas resource in the world which is estimated as 31.6 tcm.⁶ In addition, China is the second largest shale gas producing country after the U.S. in 2018.^{8,9} The shale gas production in China has gradually increased in the past years as it can alleviate China's heavy reliance on natural gas imports and assists its energy transition.² In addition to these two countries, shale gas resources are abundant worldwide, while

Canada¹⁰ and Argentina¹¹ are also producing shale gas in commercial quantities.¹² According to the report from EIA in 2013,^{13,14} the top four continents in terms of technically recoverable shale gas resources are North America (47.7 tcm), South America (40.5 tcm), Asia (39.7 tcm), and Africa (38.5 tcm). In addition, a number of countries have put efforts into shale gas exploration and exploitation, such as Poland,¹⁵ Pakistan,¹⁶ Australia,¹⁷ and South Africa.¹⁸

Shale formations, unlike conventional reservoirs, have characteristics of low porosity and low permeability due to their complex microstructures and pore systems.^{19,20} Typically, the permeability of shale rock is extremely low, ranging from nanodarcy (nD) to a few microdarcy (mD).²¹ The pores in shale have a broad range of size distributions from sub-1 nm to a few micrometers,²² while they are generally classified into micropores (pore size smaller than 2 nm), mesopores (pore size between 2 and 50 nm), and macropores (pore size larger than 50 nm).²³ In addition, shale media consist of organic and inorganic matters.^{23,24} The inorganic matters include, clay minerals,

Received: January 31, 2021

Revised: April 15, 2021

Published: April 30, 2021



carbonates, and sandstones, which are generally hydrophilic.²³ On the other hand, as the main constituent of organic matters, kerogen, which originates from sedimentary rocks by the decomposition of buried organic matters,²⁵ is insoluble in polar organic solvents.^{25,26} It has been shown that in the presence of CO₂ and hydrocarbons, kerogen can swell to varying degrees.²⁷ Both organic and inorganic matters in shale can contain a significant number of nanoscale pores, which greatly contribute to methane (the main constituent of natural gas) adsorption in shale. On the other hand, the moisture content in shale formations is non-negligible,²⁸ and the presence of (formation) water can occupy pore space and block pore throats.²⁹ Gas sorption in shale media generally consists of free gas existing mesopores, macropores, and fractures; adsorbed gas which fills pore throats or adsorbed on the pore surface due to strong fluid–surface interaction; and absorbed gas which is dissolved within kerogen matrix.³⁰ Among them, adsorbed gas is estimated to account for 20%–85% of total shale gas-in-place (GIP).³¹ Therefore, the accurate determination of shale gas adsorption is imperative to gas storage capacity estimation and well productivity.²⁴

It has been reported that shale pore structures have a significant influence on gas storage and transport mechanisms.^{32,33} Various laboratory techniques including scanning electron microscopy (SEM),^{21,34} field emission electron microscopy (FE-SEM),^{22,35} focused ion beam scanning electron microscopy (FIB-SEM),^{36,37} transmission electron microscopy (TEM),^{22,38} atomic force microscopy (AFM),^{34,39,40} nano-CT, and nanotransmission X-ray microscopy^{41,42} have been applied to characterize pore types, shapes, and distributions. In terms of pore size characterizations, measurements such as mercury injection capillary pressure (MICP),^{21–23} nuclear magnetic resonance (NMR),^{43–45} and small-angle neutron scattering (SANS)^{46–49} have been widely used. In addition, gas adsorption measurements such as low-pressure N₂ adsorption/desorption analysis and CO₂ adsorption⁵⁰ associated with various thermodynamic models such as the Barret–Joyner–Halenda (BJH) method,^{51,52} nonlocal density functional theory (NLDFT),^{32,53} Brunauer–Emmett–Teller (BET) method,^{23,54,55} and Dubinin–Radushkevich (DR) model^{47,56,57} are applied to obtain pore size distribution (PSD), specific surface area (SSA), and pore volume (PV). Each of the above-mentioned methods has its own advantages and disadvantages,³³ while varying thermodynamic assumptions applied may result in drastically different interpretations.⁵⁸

The geophysical properties of shale rocks have been generally characterized by total organic carbon (TOC) analysis,^{59–61} rock-*eval* pyrolysis,^{62–65} and X-ray diffraction (XRD) experiments^{66–69} to determine the TOC content, thermal maturity, and chemical compositions. Generally, the adsorbed methane amount has a positive correlation with the TOC content in shale samples,^{23,70,71} while clay minerals can also significantly contribute to shale gas adsorption.²³ In addition, experimental studies have reported that methane adsorption in shale significantly decreases due to the presence of moisture.^{23,70,72,73} On the other hand, the burial depth of shale reservoirs generally ranges from 800 to 7000 m,^{74–79} leading to a temperature gradient from 20 to 30 K/km^{1,78,80} and a pressure gradient around 100–150 bar/km,^{75,80–83} resulting in typical shale reservoir temperature and pressure up to 450 K^{57,78,80} and 700 bar,^{83–86} respectively. As a result, a high-pressure and high-temperature gas adsorption measurement is necessary to mimic the *in situ* condition and describe the accurate adsorption

behaviors.^{87,88} However, most shale gas adsorption measurements are limited to relatively moderate pressure conditions.⁵⁷ Moreover, the current gas adsorption measurements can obtain the excess adsorption from a *macroscopic* perspective, while the absolute adsorption amount which represents the actual adsorption amount needs to be converted.^{89–91} Generally, thermodynamic models such as Langmuir,^{80,87,92–96} supercritical Dubinin–Radushkevich (SDR),^{57,87,97–99} BET or supercritical BET (SBET),^{100–103} simplified local-density (SLD),^{104–106} and Ono–Kondo (OK) model^{107–109} are applied for methane absolute adsorption conversion. All these models are built upon their own specific assumptions, which carry different degrees of limitations. In addition, the methane adsorption in kerogen is reported to contribute up to 22% of the total gas amount in shale.^{110,111} However, the effect of gas adsorption has been rarely taken into account to convert the measured excess adsorption into the absolute adsorption due to the difficulties in distinguishing absorption and adsorption which occur simultaneously during gas adsorption measurements.^{112,113}

While it is challenging for experiments to directly observe an adsorption mechanism under nanoscale, statistical thermodynamic approaches such as Monte Carlo (MC) simulation, molecular dynamics (MD) simulation, and density functional theory (DFT) enable researchers to take into account the characteristics of adsorbates as well as adsorbents and investigate gas adsorption mechanisms in shale from a *microscopic* perspective. The adsorption properties such as adsorption amount and density distributions have been studied by explicitly considering the effect of organic/inorganic matters,^{114,115} pressure/temperature conditions,⁹⁹ confinement,^{116,117} pore structure,^{33,118} and moisture content.^{28,119–121} In addition, these statistical thermodynamic approaches have also been applied to study the conversion of excess adsorption into absolute adsorption.^{99,100,122} Although these approaches provided important insights into the conversion of excess adsorption to absolute adsorption, daunting challenges still remain in current studies due to the complex shale media characteristics including rock heterogeneity and pore size heterogeneity.

In the past, there have been a number of excellent review papers about shale studies, including pore structure characterizations,³³ gas adsorption and diffusion,^{123,124} various applied adsorption models,¹²⁵ gas transport,^{124,126} and CO₂ enhanced gas recovery.¹²⁷ Our review mainly focuses on the recent progress on the shale gas absolute adsorption estimation, especially converted from the excess adsorption. As shale rock properties as well as PSD and SSA play a crucial role in the gas adsorption behaviors, we provide in-depth discussions about commonly used characterization methods, while paying particular attention to the inherent assumptions and working mechanisms proposed in the interpretation methods.

The remainder of this review is organized as follows. In **Section 2**, we discuss shale pore structure characterization and rock composition analysis. In **Section 3**, we first discuss several commonly applied experimental measurements on PSD and SSA characterization including the SANS/UANS method, NMR, MICP, and widely used gas (N₂ and CO₂) adsorption/desorption experiments. Then, some typical interpretation methods for adsorption/desorption isotherms are discussed. In **Section 4**, we briefly discuss general characteristics of methane adsorption in shale and various factors which impact methane adsorption capacity. In **Section 5**, we first introduce the

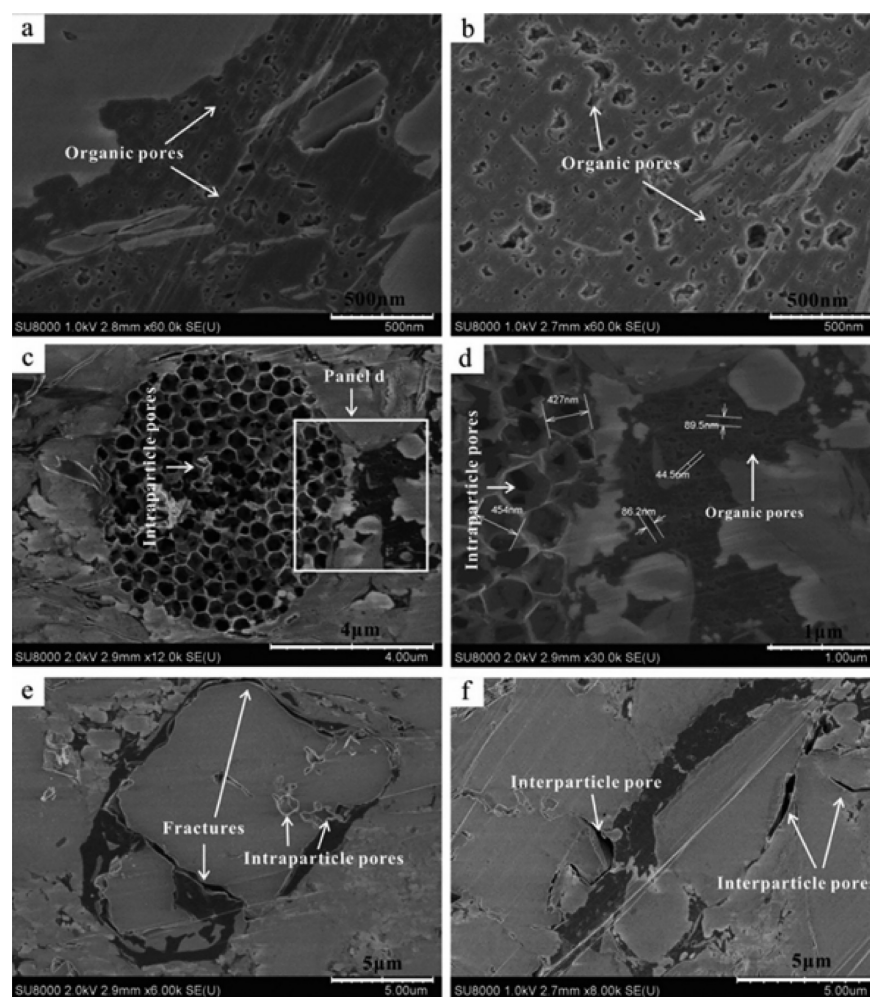


Figure 1. FE-SEM images of various pore types in high-maturity Longmaxi shale samples. Reproduced from Cao et al.¹⁴⁶ with permission. Copyright (2016) Elsevier.

concepts of excess and absolute adsorption and two commonly used adsorption measurements from a *macroscopic* perspective. Then, we illustrate the understanding about methane adsorption behaviors in shale nanoporous media by molecular simulations from a *microscopic* perspective. In the end, a number of commonly used excess-adsorption-to-absolute-adsorption conversion methods are systematically analyzed. In Section 6, we summarize key conclusions of current understandings and challenges in shale gas studies.

2. GENERAL CHARACTERISTICS OF SHALE ROCKS

As pore structures and rock compositions play important roles in methane adsorption in shale media, in this section, we briefly discuss recent advances, while more details about pore structure and imaging techniques can be referred to other review papers.^{33,128}

2.1. Characterization of Pore Structure. Nanoscale imaging via SEM has been applied to study pore structure, pore morphologies, and their distributions within organic matter (OM) and host minerals.¹²⁹ While SEM can directly detect the locations and types of pores, it has difficulties capturing most of the pores smaller than 5 nm, while only providing pore characteristics within the specific observation area in the samples.¹³⁰ In addition, a two-dimensional SEM cannot reveal the pore connectivity.¹³¹ Other direct imaging techniques,

including scanning transmission electron microscopy (STEM)¹³² (detecting pores as small as 2 nm), AFM⁴⁰ (detecting pores smaller than 2 nm), and helium ion microscopy (HIM)¹³³ (detecting pores as small as 1 nm), have a higher resolution. Some typical pore types identified in SEM images are shown in Figure 1. The classification of pores in terms of pore morphologies can be divided into the interparticle and intraparticle pores between and within the inorganic matter matrix, respectively, and organic intraparticle pores according to Loucks et al.¹³⁴ Micropores and mesopores can also be identified as shown in Figure 2. Organic intraparticle pores are commonly observed¹³⁵ in various shapes including slit, elliptical, triangular, and square^{22,135–137} (Figure 3), while micropores and mesopores are also observed in an inorganic matrix (Figure 4). In addition, Elgmati et al.¹³⁸ observed various types of porosities in shale samples from Fayetteville formations including interparticular, intergranular, kerogen, vuggy, pyrite frambloids, and fractures by SEM. They found that kerogen is porous which contains a large number of pores with sizes in the range of 5–100 nm, while inorganic matter is closely packed. Klaver et al.¹³⁹ analyzed porosity and pore connectivity of organic-rich Posidonia shale samples via mercury intrusion porosimetry and broad ion beam milling (BIB) with SEM imaging. They observed that the majority of pores are connected via a pore throat smaller than 10 nm.¹³⁹ In addition to these

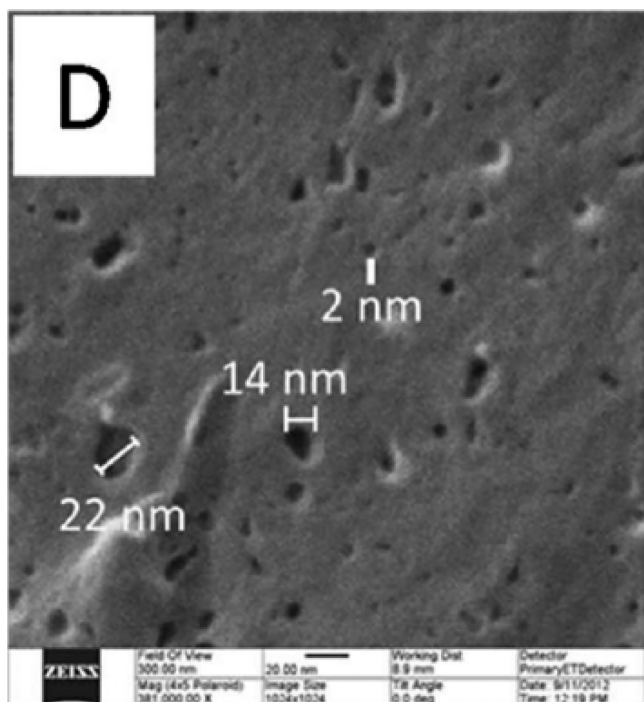


Figure 2. Helium ion microscopy image of Devonian shale samples. Reproduced from King et al.¹³⁵ with permission. Copyright (2015) American Chemical Society.

direct observation methods, fractal analysis which is an indirect method has been applied to study shale pore structures. Yang et

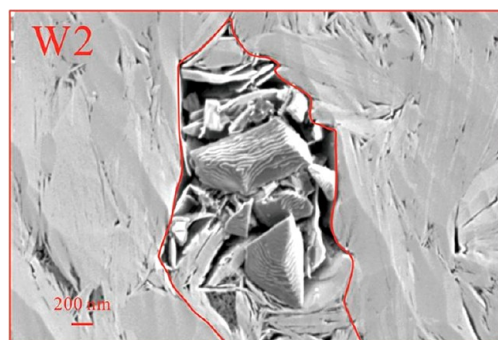


Figure 4. SEM image of pores in inorganic matrix in Wufeng–Longmaxi shale. Reproduced from Chen et al.¹⁴⁷ with permission. Copyright (2019) Elsevier.

al.¹⁴⁰ characterized the fractal properties of shale samples from the Low Cambrian Niutitang formations and found that the organic matter and micropores have a great impact on fractal dimension. In addition, the nano-CT method has been widely used in characterizing spatial distributions of pores and fractures in shale samples and their connectivity.^{141,142} The determination and segmentation of different rock compositions are based on the gray values.¹⁴³ Figure 5 presents the construction of 3D spatial distributions of organic matter and pores in shale samples from Ordos basin.¹⁴⁴ The larger microsized pores are regarded as the main pathway to connect pores. It is found that pores are mostly located in organic matter with a better connectivity. Generally, the resolution of nano-CT is around 60–80 nm. Tang et al.¹⁴⁵ compared the porosity of Silurian Longmaxi Formation shale samples obtained from nano-CT and

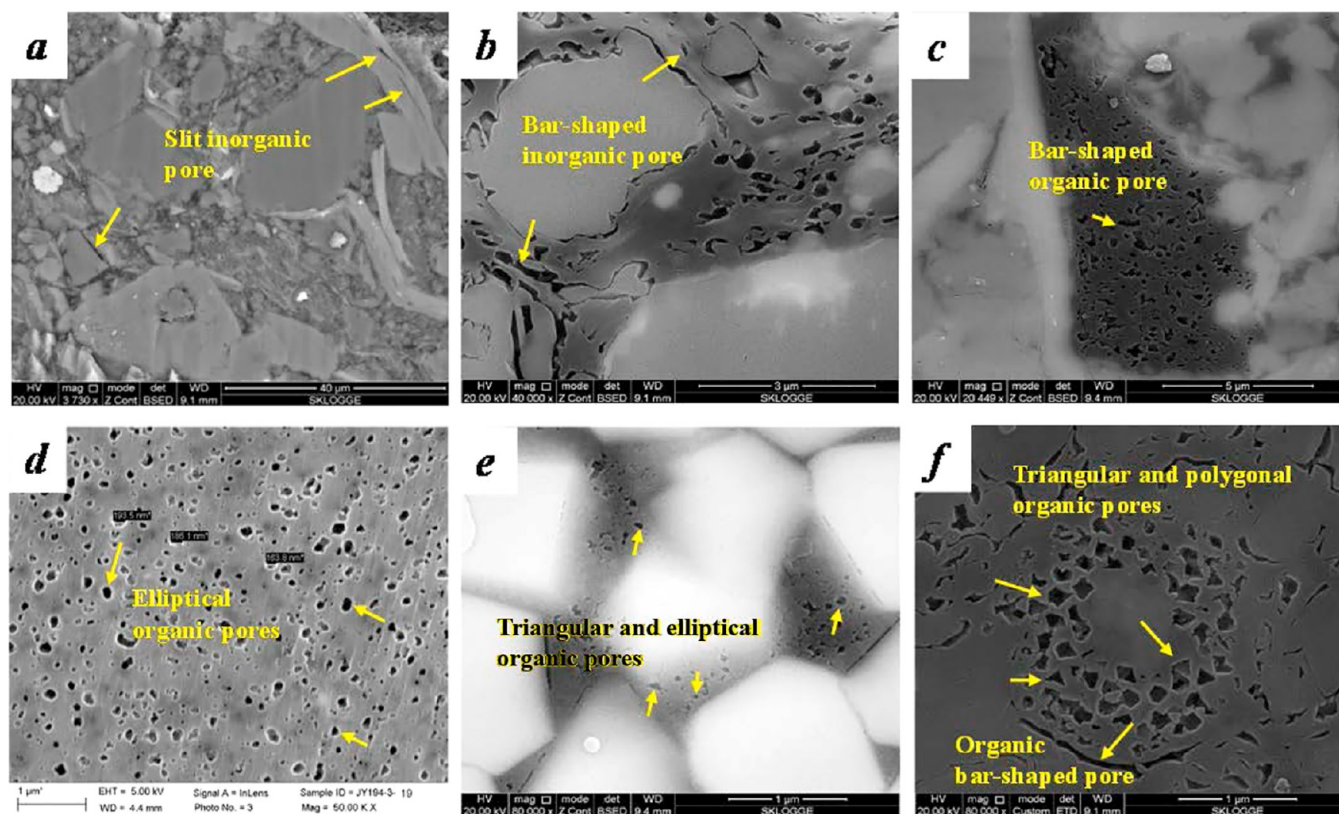


Figure 3. Different morphology of Longmaxi shale pores in the Sichuan Basin. Reproduced from Liu et al.¹⁴³ with permission. Copyright (2020) Elsevier.

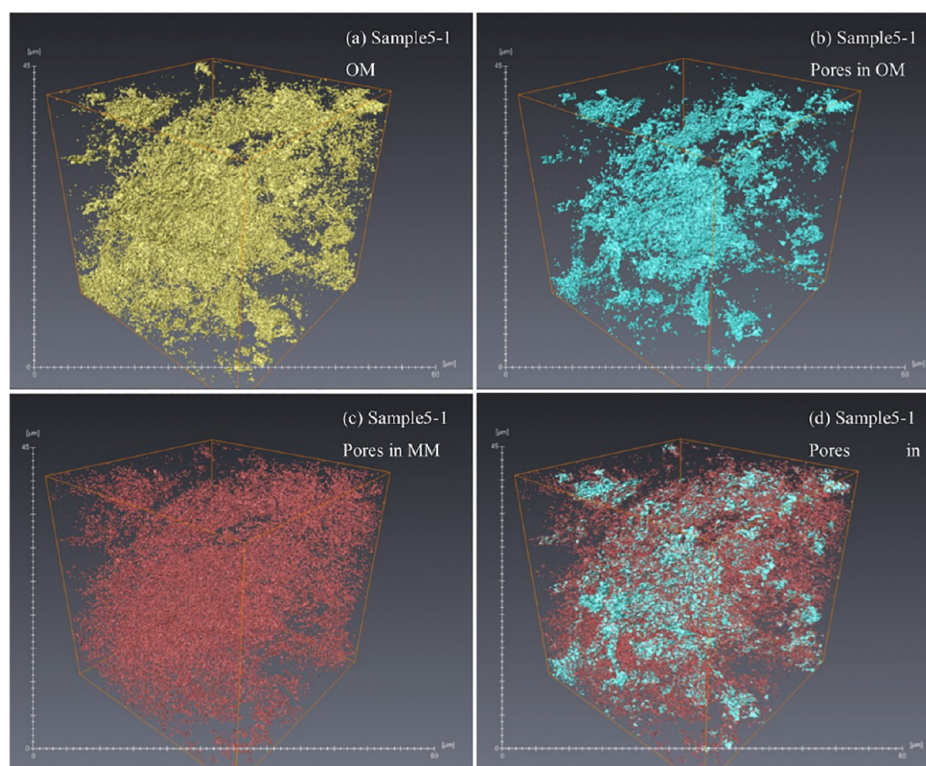


Figure 5. 3D nanoscale views of organic matter and pore distributions in shale sample: (a) organic matter distribution, (b) distribution of pores within organic matter, (c) distribution of pores within inorganic mineral matrix, and (d) distribution of all pores. Reproduced from Guo et al.¹⁴⁴ with permission. Copyright (2015) Elsevier.

FIB-SEM nanoporosity, observing a large proportion of porosity contributed to by pores under 65 nm. Yang et al.¹⁴³ found that the porosity of connected pores is larger than 1% in Upper Cretaceous Nenjiang shale, and the total porosity, especially the connected porosity, can be roughly determined by nano-CT.

2.2. Compositional Characterization of Shale Rocks.

On the basis of the depositional environment, shale can be divided into marine shale, continental shale, and translational shale.¹⁴⁸ The total organic content (TOC) in organic-rich shale varies in different formations,^{149–152} while it is reported that the content of brittle minerals including quartz, feldspar, calcite, and dolomite in marine shale is less than that in continental shale which is easier to create fractures.¹⁴⁸ Both organic and inorganic matters can exist in shale, each showing different structural properties.¹¹⁴ Clay minerals are one of the main constituents of inorganic matters which contributes to gas adsorption in shales by providing significant micropore volume and adsorption sites.^{132,153} The type and structure of clay minerals play key roles in gas adsorption, while the mineral composition can be analyzed through X-ray diffraction (XRD) patterns.^{67,68} Clay minerals consist of a Si–O tetrahedral layer and Al–O octahedral layer. A double-layer structure consists of one Si–O tetrahedral layer and one Al–O octahedral layer such as kaolinite, while illite, chlorite, and montmorillonite form a three-layer structure with two Si–O tetrahedral sheets sandwiching one Al–O octahedral sheet.^{29,154} The silica atom and aluminum atom in the Si–O sheet and Al–O sheet can be replaced by aluminum and magnesium atoms to form negatively charged clay minerals such as montmorillonite and illite.^{99,155} A number of pore structure characterizations and compositional properties of shale samples from various formations are shown in Table 1. The reported TOC and clay content range from 0.01% to 37.8%

and 0.4% to 83.49%, respectively. In addition, the illite and illite/smectite interstratified clays are the dominant clay minerals. The N₂ BET surface area, micropore volume, and pore volume vary in different samples. Ji et al.²⁹ investigated the methane adsorption in clay-rich shale rocks and found that the adsorption capacity is in the order of montmorillonite > I–S (illite-smectite) mixed layer > kaolinite > chlorite > illite. On the other hand, Xiong et al.¹¹⁴ conducted methane adsorption in inorganic matter and found that the adsorption capacity in illite is higher than that in chlorite.

Kerogen can develop abundant micropores and mesopores, which provide large SSA for methane adsorption.¹⁵⁶ TOC, thermal maturity, and kerogen types are important factors controlling methane adsorption behaviors.^{29,157} There is an overall positive correlation between methane adsorption capacity and TOC, thanks to the large number of micropores present in kerogen providing a high surface area for adsorption as well as gas dissolution within the kerogen matrix.^{21,22,70} The kerogen pore network contains the majority of the adsorbed gas as well as some free gas.¹⁵⁸ In addition, it has been reported that in organic-rich marine shale, the majority of micropores are within kerogen, while inorganic matter mainly hosts mesopores with sizes ranging from 2 to 10 nm.^{159,160} Kuila and Prasad¹⁶¹ studied the PSD in clay minerals and shale rocks and found that the mineralogy can influence the PSD, while micropores and mesopores are influenced by the abundance of illite/smectite clay. Xiong et al.¹⁵⁰ reported the importance of clay in the development of micropores in translational shale, while the mesopores and macropores contribute to the total pore volume.

The development of micropores and mesopores in kerogen also depends on thermal maturity. As kerogen thermal maturity increases, the H/C and O/C atomic ratios decrease.¹¹⁴ The

Table 1. Compositional and Pore Structure Properties of Different Shale Samples from Various Formations

| Formation | Country | TOC (%) | Moisture (%) | R _o (%) | Clay content (wt %) | Dominant type of clay and its content | N ₂ BET surface area (m ² /g) | Micro pore volume (cm ³ /100g) | Pore volume (cm ³ /g) | Source |
|--|----------------|-------------|--------------|--------------------|---------------------|---|---|---|----------------------------------|-------------------------------|
| Gordondale Member Shale | Canada | 1.6–37.8 | 0.6–8.5 | 0.7–2.5 | 0.4–15.3 | – | 0–9.3 | 0.2–1.1 | – | Ross and Bustin ²³ |
| Fort Simpson Formation | Canada | 0.2–4.9 | 1.4–5.2 | 1.6–2.5 | 1.7–24.1 | – | 3.4–44.5 | 0.3–1.3 | – | Ross and Bustin ²³ |
| Permian Carynginia Formation | Australia | 0.23–3.03 | – | – | 27.9–50.8 | Mixed illite, illite/muscovite, trace smectite: 27.6–39.8 | Avg: 4.55 | Avg: 0.07 | – | Yuan et al. ¹⁶⁰ |
| Ordovician Goldwyer Formation | Australia | 0.98–4.28 | – | – | 58.03–83.49 | Mixed illite, illite/muscovite, trace smectite: 41.26–71.14 | Avg: 12.48 | Avg: 0.21 | – | Yuan et al. ¹⁶⁰ |
| Bakken Formation | America | 11.07–20.17 | – | – | 16.2–28.6 | – | Avg: 3.75 | Avg: 0.39 | – | Yuan et al. ¹⁶⁰ |
| Dalong Formation | China | 2.81–8.05 | – | – | 3–21.8 | Illite: 17 | 2.2–3.52 | – | 0.011–0.088 | Cao et al. ¹⁷⁸ |
| Longmaxi Formation | China | 2.69–4.59 | – | – | 34.8–47.9 | Illite: 27.2–39.7 | 17.83–29.49 | – | 0.025–0.052 | Cao et al. ¹⁷⁸ |
| Niutitang Formation | China | 2.54–3.71 | – | – | 45.2–53.7 | Illite: 27.8–35.8 | 20.12–29.49 | – | 0.053–0.071 | Cao et al. ¹⁷⁸ |
| Posidonia Shale | United Kingdom | 5.78–10.92 | – | – | 23–37 | Illite-rich mixed-layer illite–smectite: 18.5–26.2 | 19.4–26.2 | 0.16–1.16 | 0.0127–0.0684 | Reyer et al. ⁹⁶ |
| Shahejie Formation | China | 1.4–5.63 | – | 0.72–0.91 | 5–23 | – | 1.26–4.01 | 0.037–0.1 | 0.00232–0.00851 | Li et al. ⁷⁷ |
| Woodford Shale | America | 1.1–7.7 | – | – | 4.4–32 | – | 0.98–8.88 | – | – | Kibria et al. ¹⁷⁹ |
| Upper Permian Shanxi shale and Upper Carboniferous Benxi shale | China | 0.01–13.68 | – | 2.3–3.2 | 54.6–73.5 | Illite/smectite mixed layer: 3.2–25.6 | – | – | – | Xiong et al. ¹⁸⁰ |
| Ordos Basin translational shale | China | 1.31–3.82 | – | – | 40.7–58.4 | – | 15.82–26.818 | 0.2–0.9 | 0.02–0.073 | Xiong et al. ¹⁸⁰ |
| Ziliujing Formation | China | 0.97–1.72 | – | – | 41.3–54 | Illite/smectite mixed layer: 15.7–22.7 | 1.01–3.05 | – | – | Gao et al. ¹⁸⁰ |
| Milk River | Canada | 1.28 | – | 0.7 | – | – | 10.1 | 0.34 | 0.049 | Clarkson et al. ⁴⁷ |
| Duvernay shale | Canada | 3.84 | – | 1.4 | – | muscovite: 14.5 | 17 | 0.2 | 0.028 | Clarkson et al. ⁴⁷ |
| Eagle Ford | America | 2.63 | – | 1.65 | – | muscovite: 20.5 | 9.3 | 0.25 | 0.05 | Clarkson et al. ⁴⁷ |
| Muskwa | Canada | 2.95 | – | 1.6 | – | illite: 12.2 | 10–14 | 0.34–0.37 | 0.024–0.039 | Clarkson et al. ⁴⁷ |
| Woodford | America | 1.55–2.77 | – | 1.4 | – | muscovite: 18.6 | 2.5–7.9 | 0.23–0.34 | 0.0025–0.033 | Clarkson et al. ⁴⁷ |
| Barnett | America | 4.11 | – | 1.45 | – | illite: 9.3 | 13.9 | 0.36 | 0.044 | Clarkson et al. ⁴⁷ |
| Haynesville | America | 2.94 | – | 2.0 | – | muscovite: 27.5 | 13 | 0.4 | 0.049 | Clarkson et al. ⁴⁷ |
| Marcellus | America | 1.57 | – | 1.2 | – | muscovite: 5.2 | 2.1 | 0.14 | 0.016 | Clarkson et al. ⁴⁷ |

kerogen maturity could impact the methane adsorption in organic pores by influencing the pore generation. Hu¹⁵⁷ performed methane adsorption experiments in two isolated type II kerogens from Barnett shale samples and found a higher adsorption capacity in an overmature kerogen than that in an immature kerogen. They attributed such a phenomenon to the nanopores opening up by thermal degradation of kerogen during catagenesis,¹⁶² which would possibly increase the surface area in an overmature kerogen. Curtis et al.¹⁶³ used FIB-SEM to investigate the secondary organic porosity evolution in Woodford shale samples. They did not find the presence of organic porosity unless vitrinite reflectance (R_o) reached up to 0.9%, while the porosity in organic matter develops at a higher thermal maturity. They also mentioned that due to the complicated factors such as organic matter types, the porosity cannot be simply predicted from the maturity. In addition, Milliken et al.¹³⁰ investigated several shale samples from Marcellus formations with varying thermal maturities and concluded that TOC rather than maturity is the major controlling factor on pores in organic matter. For overmature shales, Wang et al.⁵⁹ studied the porosity in samples from Lower Cambrian shale and Upper Ordovician–Lower Silurian shale and reported a declining trend of organic matter porosity with R_o above 2%. They also found that in overmature shale, the increase in porosity with TOC is significant in samples with TOC < 5%, while the positive correlation becomes less obvious as TOC increases.

In addition, another important factor affecting adsorption capacity is the presence of moisture.^{29,164} Moisture is widely present under *in situ* conditions,^{165,166} and initial water saturation can be over 40% in some gas-bearing shale.¹⁶⁷ Passey et al.¹⁶⁸ reported that water can be preferentially adsorbed on the clay surface, which can greatly reduce methane adsorption.¹⁶⁹ Experimental studies have shown that water can be trapped in kerogen nanopores even for an overmatured kerogen.^{48,170} The water confined in small pores can form a water bridge and potentially block the micropore thoroughly,¹⁷¹ while the adsorbed water is less likely to block pore throats in large mesopores.¹⁷² As a result, the decreased adsorption capacity in organic-rich shale can range from 40% to 95% compared to dry conditions.^{23,72,173} Due to the hydrophilic nature of clay minerals, the existence of moisture is generally linked to water adsorption in clay.¹⁷⁴ Ross and Bustin²³ observed significant decreases in gas adsorption capacity in moisture-equilibrated illite and montmorillonite samples, while the adsorption capacity remains unchanged in kaolinite samples. On the other hand, a few experimental works^{175–177} observed no apparent correlation between adsorption capacity and moisture content. They generally proposed that the moisture adsorption mainly occurs in clay minerals, while the gas adsorption in organic matter is less affected. In addition, Feng et al.⁵⁴ reported that pore structure characteristics can be affected by moisture as the capillary water can block smaller pores and form water films in clays, while the decline in SSA in illite and montmorillonite can be up to 35%.

3. CHARACTERIZATION OF PORE SIZE DISTRIBUTION AND SPECIFIC SURFACE AREA

Unlike the conventional reservoirs, shale media typically has a PSD ranging from sub-1 nm to a few micrometers,²² while methane adsorption behaviors in micropores and mesopores can be drastically different.¹¹⁶ In addition, methane adsorption capacity in shale is correlated well with SSA.¹⁸¹ Therefore, the

accurate characterization of PSD and SSA is imperative to the estimation of methane adsorption capacity in shale.⁵⁰ In this section, we discuss commonly applied experimental measurements on PSD and SSA characterization as well as gas (N_2 and CO_2) adsorption/desorption isotherm-based measurements and their corresponding interpretation methods.

3.1. Commonly Applied Experimental Measurements. SEM which provides petrographic images as discussed in Section 2.1 can obtain a direct observation of pore morphology in shale rocks, while multiple characterization methods can quantify PSD and SSA. Generally, PSD and SSA are characterized by various techniques such as small-angle/ultrasmall angle neutron scattering techniques (SANS/USANS),^{46,182} nuclear magnetic resonance (NMR),^{183,184} mercury intrusion capillary pressure (MICP),^{47,185} and gas (N_2 and CO_2) adsorption/desorption.^{50,186} Each method is based on its own specific theoretical background to infer the corresponding pore structures.¹³³ Therefore, these techniques have their own advantages and limitations, while the combination of several methods are commonly applied for pore structure characterization.¹²⁸ We address the gas adsorption/desorption-based methods and their interpretation models exclusively in Section 3.2.

SANS/USANS have been widely used to study PSDs in coal and shale.^{46,182,187,188} In contrast to MICP, these methods conduct nondestructive measurements and can characterize pores ranging from micropores to macropores assuming a spherical geometry.¹⁸⁹ Moreover, the measurement is conducted under elevated pressure and temperature conditions without the influence of either fluid–surface interactions or percolation.⁴⁷ PSD and SSA can be interpreted via the regression of the polydisperse spheres (PDSP) model by identifying the characteristic power law of scattering intensity within the range of scattering vector Q , given as $Q = 4\pi\lambda^{-1} \sin(\theta)$ related to the neutron wavelength (λ) and scattering angle (2θ).¹³³ The slope in log–log scale is determined by the surface fractal dimensions.¹³³ The pore radius r can then be expressed by $r \approx 2.5/Q$.¹⁹⁰ Clarkson et al.⁴⁷ and Sun et al.⁴⁶ reported that the pore size characterized by SANS/USANS can range from 2.5 nm to 2.5 μm . Moreover, Clarkson et al.⁴⁷ conducted comparative measurements of SANS/USANS with gas adsorption techniques, and they found a reasonable agreement in terms of PSDs in North American shale. Bahadur et al.¹⁸² tested the Cretaceous shale samples by using SANS/USANS and found that both micropores and mesopores contribute to the porosity and SSA.

Nuclear-magnetic-resonance (NMR) measurement is one of nondestructive methods which injects low-viscosity fluids to characterize PSDs.^{45,183,184} By detecting specific atomic nuclei resonant frequencies of injected fluids, PSD is obtained by calibrating NMR T_2 (transverse relaxation time) spectra which reflects the fluids stored in pore space. The expression of T_2 spectra at the i th time constant can be given as $1/T_{2,i} = \rho_p S_i/V_i$, where ρ_p and S_i/V_i represent surface relaxivity ($\mu\text{m}/\text{ms}$) and the ratio of pore surface area to the pore volume (μm^{-1}), respectively.⁴³ The relationship between surface volume ratio and pore radius r (μm) can be expressed by using pore shape factor α as $S_i/V_i = \alpha/r$, while the possible pore geometry needs to be presumed. The shape factors for spherical, cylindrical, and slit pores are 3, 2, and 1, respectively (in a slit geometry, the pore radius is half of the pore width). Sigal¹⁹¹ conducted NMR measurements to obtain PSDs in organic shale reservoir rock samples by assuming spherical pores. The methane Langmuir adsorption isotherm is used to assist their T_2 spectra calibration

for PSD determination. The observed pore diameters range from 1 to 100 nm, with the pores smaller than 10 nm accounting for 20%–40% of total pore volume. However, they also pointed out that PSD would shift to smaller sizes if a slit geometry is presumed. In addition, the application of the Langmuir model which describes gas adsorption on a single energetically homogeneous surface as we discuss later is questionable in shale nanoporous media with rock heterogeneity.⁸⁸ Li et al.¹⁹² argued that the signals from H-containing components of shale rocks such as kerogen and connate water would affect the converted PSD from NMR T_2 spectra, while Liu et al.⁴³ deduced the signal of a shale matrix from the T_2 spectra.

MICP is widely applied in characterizing pore-throat size distribution (*not* pore size distribution) in both conventional and unconventional shale rocks.¹⁸⁵ Washburn's equation¹⁹³ which assumes a bundle of cylindrical tubes is applied to convert the mercury intrusion pressure to pore throat size in porous media, given as

$$D = \frac{-4\gamma \cos(\theta)}{P_i}$$

where D is the throat diameter, γ the interfacial tension between liquid mercury and a vacuum (480 dyn/cm at 20 °C), θ the contact angle in the mercury–vacuum–substrate system, and P_i the mercury intrusion pressure. The schematic representation is shown in Figure 6. The coefficient 4 is because a cylindrical

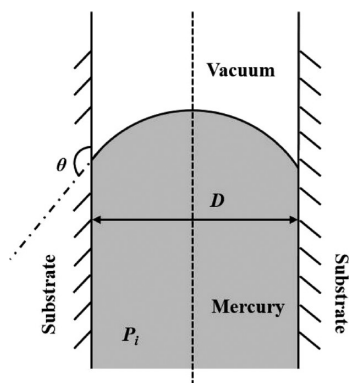


Figure 6. Schematic representation of MICP.

throat yields a spherical-type curved interface. While the contact angle in the mercury–vacuum–substrate system is one of the important parameters for the MICP analysis, the measurement is usually conducted in a mercury–vapor–substrate system and is reported to vary with different materials, for example, 128°–148° on glass¹⁹⁴ and 139°–160° on kaolinite.^{195,196} However, a fixed contact angle value as 130° or 140° has been generally used in MICP analysis for shale rock characterization.^{197,198} In addition, due to the compressibility and possible sample destruction under high intrusion pressure,^{43,47} the intrusion pressure should not exceed a certain value,¹⁶¹ and the lower limit of the pore throat diameter is around 3 nm, while the upper limit is around 200 μm .⁴⁷ Moreover, Sigal¹⁹¹ found that the mercury porosity obtained from the penetrated liquid mercury volume is about half of the helium porosity, indicating that mercury penetration is limited. Such underestimations of mesopore and macropore volumes arise from the shielding effect.¹⁹⁹

3.2. Gas Adsorption/Desorption and Their Interpretations. Low-pressure gas (N_2 and/or CO_2) adsorption/desorption isotherms have been widely used to characterize

PSD and SSA of shale samples and isolated kerogens.^{160,186} N_2 adsorption/desorption isotherms at 77 K for pressures up to its saturation pressure P_0 can detect pores of widths larger than 2 nm and up to 300 nm,⁴⁷ as N_2 has an insufficient penetration into micropores under low pressures.²⁰⁰ CO_2 adsorption at 273 K is used to quantify the micropore distributions in the range of 0.33–2 nm. Psarras et al.⁵⁰ reported that the underestimation of SSA and PV in the tested Eagle Ford shale samples can reach up to 28% and 68%, respectively, if only N_2 adsorption/desorption is applied, indicating the importance and necessity of combining CO_2 adsorption measurement. In a number of works,^{185,201,202} the SSA and PSD for micropores (<2 nm), mesopores (2–50 nm), and macropores (>50 nm) are characterized by using CO_2 adsorption, N_2 adsorption/desorption, and MICP, respectively. Six types of adsorption/desorption isotherms are suggested by IUPAC,²⁰³ including microporous materials (Type I), nonporous or microporous materials (Types II and III), mesoporous materials (Type IV), micro-to-mesoporous media with weak adsorbate–adsorbent interactions (Type V), and nonporous materials with smooth surfaces and layer-by-layer multilayer adsorption.^{204,205} In some cases, adsorption and desorption isotherms do not coincide with each other, yielding hysteresis loops. Figure 7 presents representative N_2 adsorption/desorption and CO_2 adsorption isotherms in organic-rich shale samples from the Sichuan Basin.²⁰⁶

In order to convert experimentally measured adsorption/desorption isotherms to SSA and PSD, interpretation methods are essential. The thermodynamic models such as Brunauer–Emmett–Teller (BET)²⁰⁷ and Barrett–Joyner–Halenda (BJH)²⁰⁸ methods have been widely used to obtain SSA and PSD based on N_2 adsorption/desorption isotherms. However, due to the strong fluid–surface interactions in nanoporous media, these models should be applied with caution.^{58,209} Nonlocal density functional theory (NLDFT) which can account for both fluid–fluid and fluid–surface interactions has been applied for PSD and SSA characterizations based on N_2 adsorption/desorption and CO_2 adsorption isotherms as recommended by IUPAC. Very recently, Shi et al.²¹⁰ summarized various PSD and SSA characterization methods used in nanoporous materials. In the following subsections, we explicitly discuss these thermodynamic models and their inherent assumptions as well as limitations.

3.2.1. Brunauer–Emmett–Teller (BET) Method. The BET method²⁰⁷ has been widely used to obtain SSA of porous media by interpreting N_2 adsorption isotherms in various engineering applications.^{161,211,212} The BET model is based on the extension of the monolayer Langmuir adsorption model, which intends to describe multilayer adsorption on a single energetically homogeneous surface.^{209,213} The schematic diagram of BET multilayer adsorption is shown in Figure 8(a). The basic assumptions²⁰⁷ in the BET model include: (a) The flat surface shows characteristics of geometrical and energetical homogeneity with equal surface density and energy for each site. (b) The adsorbate molecules physically adsorb on the surface in layers infinitely. (c) The adsorbate molecules only interact with adjacent layers without lateral interactions. (d) The enthalpy of adsorption for the first layer is constant and greater than the second (and higher). (e) The enthalpy of adsorption for the second (and higher) layers is the same as the enthalpy of liquefaction. The resulting BET equation is given as²⁰⁷

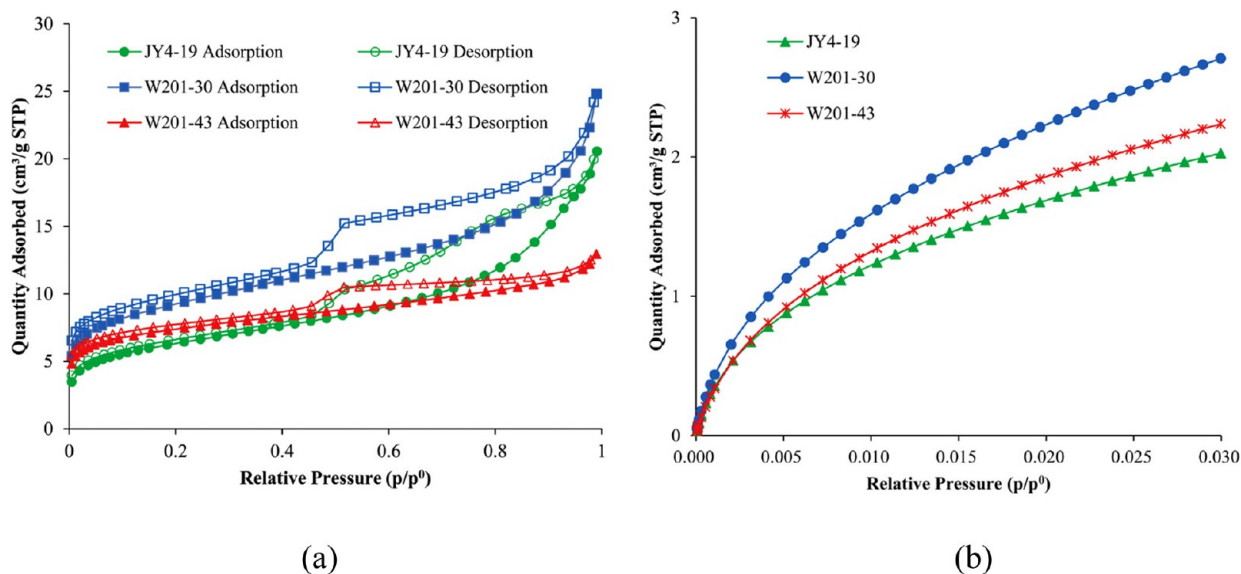


Figure 7. (a) N_2 adsorption/desorption isotherms. (b) CO_2 adsorption isotherm in organic-rich shale samples from the Sichuan Basin. Reproduced from Wei et al.²⁰⁶ with permission. Copyright (2014) Elsevier.

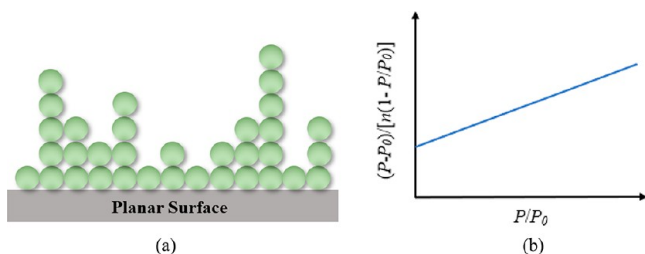


Figure 8. Schematic representations of (a) BET multilayer adsorption model and (b) BET linear plot.

$$\frac{P/P_0}{n(1 - P/P_0)} = \frac{1}{n_m k_0} + \frac{k_0 - 1}{n_m k_0} \left(\frac{P}{P_0} \right) \quad (1)$$

where P and P_0 are bulk pressure and saturation pressure of the adsorbate, respectively; n and n_m represent the total adsorption amount at pressure P and the monolayer capacity, respectively, and k_0 is related to the energetic of adsorption in the system, which can be given as

$$k_0 = \exp\left(\frac{E_1 - E_L}{RT}\right)$$

where E_1 represents the heat of adsorption for the first layer, and E_L is that for the second and higher layers and is equal to the heat of liquefaction. The right-hand side of eq 1, $\frac{P/P_0}{n(1 - P/P_0)}$, has a linear correlation with the term P/P_0 with the slope and intercept on the y -axis (Figure 8(b)) as $\frac{k_0 - 1}{n_m k_0}$ and $\frac{1}{n_m k_0}$, respectively. It is generally believed that in the relative pressure (P/P_0) range from 0.05 to 0.35,²¹⁴ N_2 monolayer adsorption occurs,²¹⁵ and then n_m and k_0 are obtained from the slope and intercept on the y -axis through a linear regression of BET plot. The BET SSA, S_{BET} , can then be obtained as

$$S_{BET} = n_m a^2 \quad (2)$$

where a^2 is the cross-sectional area of single N_2 molecule, which is generally given as 0.162 nm^2 .²⁰⁷ It is obtained by assuming that N_2 molecules are completely accommodated in the monolayer,

and the density is equal to the bulk liquid at 77 K with a hexagonal close packing.²⁰⁷

However, the BET model should be applied with cautions in nanoporous media.^{215,216} In principle, in the framework of the BET model, the adsorption occurs on a single energetically homogeneous surface. However, in shale nanoporous media, the rock heterogeneity is omnipresent, and the overlapped fluid–surface interactions in micropores and some small mesopores¹¹⁶ might cause overestimation of BET SSA.²¹⁷ The overestimation in the BET monolayer capacity in microporous materials, such as metal–organic frameworks (MOFs), which is described as “pore filling contamination”, has been well documented.²¹⁸ Despite the N_2 adsorption isotherm being purely determined by adsorbate–adsorbent and adsorbate–adsorbate interactions, the BET surface area is also dependent on the choice of cross-sectional area^{219,220} and pressure range for linear fitting.²¹⁴ Rouquerol et al.²²¹ proposed consistency criteria for N_2 adsorption isotherm analysis, which ensures a positive adsorption energy and an increased adsorption amount as pressure increases. In addition, surface chemistry²¹¹ and pore morphology^{211,219,222} are also reported to influence the BET surface area in silica and porous glasses by performing a grand canonical Monte Carlo (GCMC) simulation to mimic N_2 adsorption. On the other hand, as mentioned above, the BET model is conducted to interpret the N_2 adsorption isotherm, while N_2 might have limited access to micropores in shale.

The BET model has been widely used to measure SSA in shale samples. The measured BET SSA of shale rocks can range from 0.02 ²²³ to $34.33 \text{ m}^2/\text{g}$ ¹⁸⁵ for various samples in different formations, while the measured BET SSA in isolated kerogen can be up to over $300 \text{ m}^2/\text{g}$.¹⁴⁶ Not only the chemical compositions of organic and inorganic matters in shale are different but also different types of kerogen would result in different surface chemistries. Moreover, the kerogen pore surface is not smooth,²²⁴ carrying varying degrees of surface roughness. Kuila and Prasad¹⁶¹ recommended the use of consistency criteria proposed by Rouquerol et al.²²¹ Moreover, as the BET model only provides qualitative estimation of surface area, it should be used with cautions for quantitative

computation of the average pore diameter^{71,225} by combining the BET surface area and total pore volume.

3.2.2. *Barret–Joyner–Halenda (BJH) Model.* The BJH model is widely applied to obtain PSD in shale media by interpreting the N₂ adsorption/desorption isotherm at 77 K.^{80,161,226} The schematic representations of the BJH model are plotted in Figure 9.

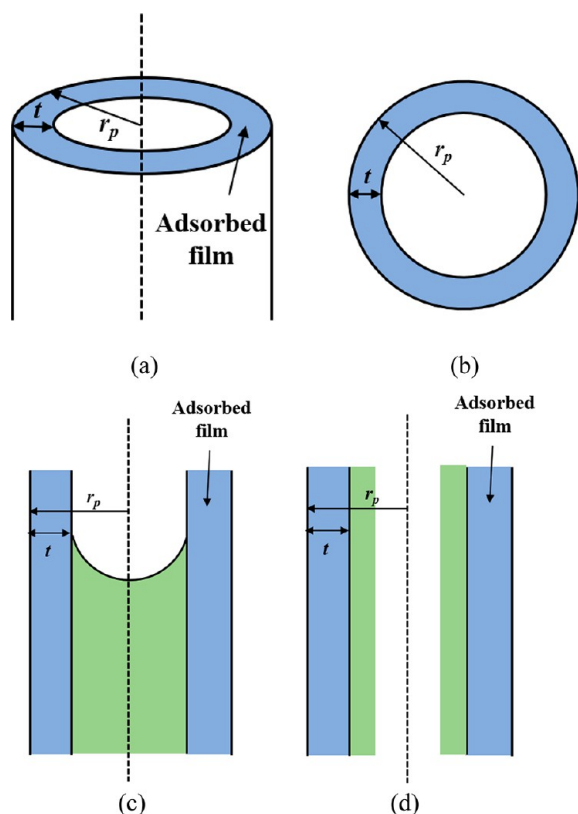


Figure 9. Schematic representations of (a) BJH model and (b) top view of BJH model and liquid–vapor interface in (c) evaporation and (d) condensation processes.

Within the framework of the BJH model, the fluids are confined in a cylindrical pore with a radius r_p (we note that other geometries such as slit are also possible), consisting of an adsorbed phase with a thickness of t on the pore surface and a free gas phase in the middle of the pore with a cylindrical geometry of radius $r_f = r_p - t$. The adsorbed phase is assumed as a homogeneous liquid phase with its density the same as the liquid N₂ density at P_0 and 77 K, and its thickness t increases as pressure increases.^{161,209} The free gas phase is homogeneous with its density the same as the bulk N₂ gas density at a given pressure. The onset capillary condensation/evaporation pressure P in the free gas phase is described by the simplified Kelvin equation,²²⁷ assuming a zero contact angle

$$\ln\left(\frac{P}{P_0}\right) = \frac{\alpha\gamma V_m^l}{RT(r_p - t)} \quad (3)$$

where V_m^l is the molar volume of liquid N₂ at 77 K and P_0 , γ is the bulk vapor–liquid N₂ interfacial tension at 77 K, R is the gas constant, T is the temperature, and α is the shape of the vapor–liquid interface. During N₂ adsorption, it is assumed that as pressure increases, t increases, and the shape of the vapor–liquid interface remains as the side of a cylinder. During N₂

desorptions, as pressure drops, the shape of the vapor–liquid interface remains as the part of a sphere. Therefore, $\alpha = 1$ and $\alpha = 2$ represent the condensation (adsorption) and evaporation (desorption) processes, respectively. The schematic representations of vapor–liquid interfaces are shown in Figure 9(c) and (d). In order to convert adsorption/desorption isotherms to PSD, knowledge of the adsorption layer thickness is necessary. The Harkins–Jura t-plot²²⁸ and α_s -plot²⁰⁶ have been applied to calculate t . Compared with the α_s -plot, the Harkins–Jura t-plot is more widely applied,²⁰⁶ which is given as

$$t = \left[\frac{0.1399}{0.034 - \log\left(\frac{P}{P_0}\right)} \right]^{1/2} \quad (4)$$

It should be noted that the parameters in the Harkins–Jura t-plot are obtained based on N₂ adsorption on aluminum hydroxides and oxides with a slit-shaped pore geometry at 78 K.^{229,230} Kruck et al.²³¹ reported that increasing t given in eq 4 by 0.3 nm can provide a good prediction for the pore diameter in MCM-41 ranging from 2 to 6.5 nm. In addition, Kuila et al.²³² showed that the discrepancy of differential pore volumes of using different thickness equations can be as high as 60%. Moreover, it has been revealed that there is an artificial peak around 4 nm in PSDs obtained by using desorption isotherms,^{80,201} due to the tensile strength effect (TSE) arising from the breaking of meniscus.²³³ Such a tensile strength effect is usually taking place in the pressure range of 0.45–0.55 P/P_0 , where there is a sudden drop in desorption isotherm,^{226,233} and results in delayed desorption due to the blocking effect of a narrow neck in ink-bottle shaped pores.

The BJH model is generally applied based on the assumption of cylindrical pores, whereas different pore shapes are observed in shale rock from SEM images as discussed in Section 2, indicating pore geometry disparity.¹⁹ The BJH model cannot accurately describe N₂ adsorption/desorption isotherms in micropores and small mesopores, where the capillary condensation/evaporation disappear.^{234,235} Coasne et al.²²² tested the validity of the BJH method for silica nanopores with different geometries (cylindrical, elliptical, and constricted pores) by using GCMC simulations. They found that the pore diameter from the BJH method is underestimated, which is consistent with experimental results for mesoporous silica of MCM-41 and SBA-15, in which the BJH method underestimates 20%–30% of PSDs in pores smaller than 10 nm.²³⁶ Ojeda et al.²³⁷ compared the PSD of SBA-15 between the BJH–Broekhoff and de Boer (BdB) model and NLDFT. The BdB model is proposed to modify the Kelvin equation by accounting for the attractive potential arising from the pore surface. They found a reasonable agreement between NLDFT and the BJH–BdB model and stated the importance of considering fluid–surface interaction for porous media with pores smaller than 10 nm. Xiong et al.³² reported differently shaped PSDs from the BJH model and NLDFT for shale rocks in the Wufeng Formation, while NLDFT can provide information about micropores and renders a wider range of PSD. They reported a multimodal PSD from NLDFT with peaks in 1.4, 3.8, and 10–30 nm, while a unimodal PSD is observed from the BJH method with peaks at 60–100 nm.

3.2.3. *Density Functional Theory (DFT).* Due to the accurate description of an inhomogeneous density profile and fluid–surface interaction, NLDFT can be a useful tool to obtain a more

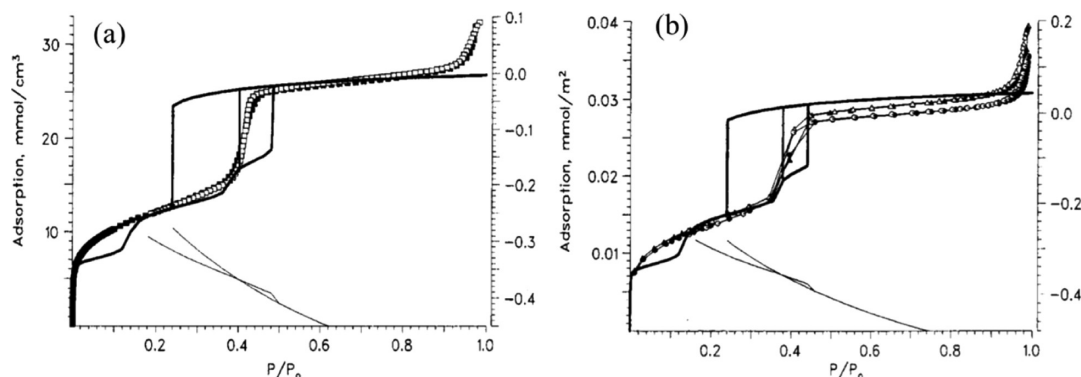


Figure 10. Comparisons of N₂ adsorption/desorption isotherms in MCM-41 from experimental measurements and NLDFT. Symbols are experimental measurements (closed symbols, adsorption; open symbols, desorption): (a) squares represent 4.6 nm cylindrical pores and (b) circles and triangles represent 4.32 and 4.47 nm cylindrical pores, respectively. Thick solid lines are NLDFT isotherms. Thin solid lines are grand potential from NLDFT. Right axis is for the grand potential. Reproduced from Ravikovitch et al.²³⁸ with permission. Copyright (1995) American Chemical Society.

accurate PSD. Within the framework of DFT, the grand potential Ω is related to the Helmholtz free energy and external potential, while Ω is minimized at an equilibrium for an open system, which is given as³⁰

$$\Omega_f[\rho_f(\mathbf{r})] = F[\rho_f(\mathbf{r})] - \int d\mathbf{r} \rho_f(\mathbf{r}) [\mu_f - U_{\text{ext}}(\mathbf{r})] \quad (5)$$

where $\rho_f(\mathbf{r})$ is the fluid density distribution at position \mathbf{r} , μ_f is the bulk fluid chemical potential, $F[\rho_f(\mathbf{r})]$ is the Helmholtz free energy functional, and $U_{\text{ext}}(\mathbf{r})$ is the external potential which is used to describe the fluid–surface interaction. The subscript “ f ” refers to fluids. We note that in eq 5, the surface is treated as an external field which is not affected by fluid distributions. The $F[\rho_f(\mathbf{r})]$ can be separated into the ideal term $F_{\text{id}}[\rho_f(\mathbf{r})]$ and the excess term $F_{\text{ex}}[\rho_f(\mathbf{r})]$

$$F[\rho_f(\mathbf{r})] = F_{\text{id}}[\rho_f(\mathbf{r})] + F_{\text{ex}}[\rho_f(\mathbf{r})] \quad (6)$$

where $F_{\text{id}}[\rho_f(\mathbf{r})] = k_B T \int d\mathbf{r} \rho_f(\mathbf{r}) [\ln(\Lambda_f^3 \rho_f(\mathbf{r})) - 1]$, and k_B is the Boltzmann constant, T is the absolute temperature, and Λ_f is the de Broglie thermal wavelength of fluid component.

At equilibrium, the grand potential functional reaches the minimum, and fluid density distributions are given as

$$\rho_f(\mathbf{r}) = \Lambda_f^{-3} \exp\left(-\frac{\beta \delta F_{\text{ex}}[\rho_f(\mathbf{r})]}{\delta \rho_f(\mathbf{r})} + \beta \mu_f - \beta U_{\text{ext}}(\mathbf{r})\right) \quad (7)$$

where δ represents the functional derivative, and $\beta = \frac{1}{k_B T}$. The bulk fluid chemical potential is given as

$$\mu_f = \mu_f^{\text{id}} + \mu_f^{\text{ex}} \quad (8)$$

where $\mu_f^{\text{id}} = k_B T \ln(\Lambda_f^3 \rho_{f,b})$ and μ_f^{ex} are ideal and excess term of chemical potential, respectively, and $\rho_{f,b}$ denotes the fluid bulk density. Combining eqs 7 and 8, the density distributions could be further simplified as

$$\rho_f(\mathbf{r}) = \rho_{f,b} \exp\left(-\frac{\beta \delta F_{\text{ex}}[\rho_f(\mathbf{r})]}{\delta \rho_f(\mathbf{r})} + \beta \mu_f^{\text{ex}} - \beta U_{\text{ext}}(\mathbf{r})\right) \quad (9)$$

Equation 9 can be solved by the Picard iteration.¹⁶⁹ Then, the average fluid density in a given pore i at pressure P , $\rho_{\text{ave},i}$ is given as

$$\rho_{\text{ave}}(P, V_i) = \frac{1}{V_i} \int_{V_i} d\mathbf{r} \rho_f(\mathbf{r}) \quad (10)$$

where V_i is the volume of pore i . DFT can also capture the hysteresis in the adsorption/desorption isotherms.²³⁸ Ravikovitch et al.²³⁸ claimed that the metastable condensation and the equilibrium transition branches in DFT correspond to adsorption (capillary condensation) and desorption (evaporation) in cylindrical micropores and mesopores in MCM-41 as depicted in Figure 10. Then, the total gas amount in the porous media $N_{\text{total}}(P)$ is given as

$$N_{\text{total}}(P) = \sum_i \rho_{\text{ave}}(P, V_i) \times V_i \quad (11)$$

PSD is obtained by fitting $N_{\text{total}}(P)$ from DFT to the experimentally measured adsorption/desorption isotherms.

Therefore, the accurate approximation of the excess Helmholtz free energy shown in eq 9 is crucial. Within the framework of NLDFT for PSD characterization, N₂ and CO₂ molecules are usually treated as a single-site Lennard-Jones (LJ) model.^{238–242} Then, the excess Helmholtz free energy can be further expressed as

$$F_{\text{ex}}[\rho_f(\mathbf{r})] = F_{\text{ex}}^{\text{rep}}[\rho_f(\mathbf{r})] + F_{\text{ex}}^{\text{att}}[\rho_f(\mathbf{r})] \quad (12)$$

where $F_{\text{ex}}^{\text{rep}}[\rho_f(\mathbf{r})]$ and $F_{\text{ex}}^{\text{att}}[\rho_f(\mathbf{r})]$ are the excess Helmholtz free energy of a hard-sphere term and attraction term, respectively.

For the hard-sphere term $F_{\text{ex}}^{\text{rep}}[\rho_f(\mathbf{r})]$, the fundamental measure theory^{241,243–245} (FMT) is one of the most popular methods, while the modified FMT^{246,247} (MFMT), smoothed density approximation^{238–241} (SDA), and weighted density approximation^{169,248,249} (WDA) are also widely used. In Table 2, we present the detailed information on $F_{\text{ex}}^{\text{rep}}[\rho_f(\mathbf{r})]$ used in the literatures. Ravikovitch and Neimark^{238,250} used SDA in the $F_{\text{ex}}^{\text{rep}}[\rho_f(\mathbf{r})]$ term to calculate PSD in siliceous mesoporous materials

$$F_{\text{ex}}^{\text{rep}}[\rho_f(\mathbf{r})] = \int d\mathbf{r} \frac{\rho_f(\mathbf{r})}{\bar{\rho}_f(\mathbf{r})} f_{\text{ex}}^{\text{rep}}(\bar{\rho}_f(\mathbf{r})) \quad (13)$$

where $f_{\text{ex}}^{\text{rep}}(\bar{\rho}_f(\mathbf{r}))$ is the excess free energy density, and $\bar{\rho}_f(\mathbf{r}) = \int d\mathbf{r}' \rho_f(\mathbf{r}') \omega(|\mathbf{r} - \mathbf{r}'|; \rho_f(\mathbf{r}'))$, with $\omega(|\mathbf{r} - \mathbf{r}'|; \rho_f(\mathbf{r}'))$ the weighted function.

FMT is also a popular choice to describe the $F_{\text{ex}}^{\text{rep}}[\rho_f(\mathbf{r})]$ term in NLDFT,²⁴² which is given as

Table 2. Various Versions of NLDFT and QSDFT^a

| No. | Authors | Methods | Samples | Surfaces | Geometries | T (K) | P (bar) | F _{ex} ^{rep} | F _{ex} ^{att} | U _{ex} ^{att} (NLDFT) or U _{ex} ^{att} (QSDFT) |
|-----|----------------------------------|-------------------------|----------------------------------|----------|---|--|--|--------------------------------|--------------------------------|--|
| 1 | Ravikovich et al. ²⁴² | NLDFT | N ₂ , CH ₄ | Carbon | Slit | 77.4 (N ₂), 111 (CH ₄) | 0–1.01 (N ₂), N/A (CH ₄) | SDA, FMT | WCA | Steele 10-4-3 |
| 2 | Ravikovich et al. ²⁴² | NLDFT | N ₂ , CO ₂ | Silica | Cylindrical | 77.4 (N ₂), 273.2 (CO ₂) | 0–1.01 (N ₂), 0–133.3 (CO ₂) | SDA, FMT | WCA | Lj 10-4 |
| 3 | Ravikovich et al. ²³⁹ | NLDFT | N ₂ | Carbon | Slit | 77 | 0–0.97 | SDA | WCA | Lj 10-4 |
| 4 | Ravikovich et al. ²⁴⁰ | NLDFT | N ₂ , CO ₂ | Carbon | Slit | 77.4 (N ₂), 273 (CO ₂) | 0–1.01 (N ₂), 0–1.07 (CO ₂) | SDA | WCA | Steele 10-4-3 |
| 5 | Ravikovich et al. ²³⁸ | NLDFT | N ₂ | Graphite | Cylindrical | 77.4 (N ₂) | 0–1.01 (N ₂) | SDA | WCA | Lj 10-4 |
| 6 | Cimino et al. ²⁴¹ | NLDFT | N ₂ | Graphite | Cylindrical | 77.4 (N ₂) | 0–1.01 (N ₂) | SDA | WCA | Lj 10-4 |
| 7 | Cimino et al. ²⁴¹ | QSDFT | N ₂ | Silica | Cylindrical | 77 (N ₂) | 0–0.97 (N ₂) | FMT | WCA | WCA |
| 8 | Ravikovich et al. ²⁴⁴ | QSDFT | N ₂ | Silica | Cylindrical | 77 (N ₂) | 0–0.97 (N ₂) | FMT | WCA | WCA |
| 9 | Neimarka et al. ²⁴⁵ | QSDFT | N ₂ | Carbon | Slit | 77.4 (N ₂) | 0–1.01 (N ₂) | FMT | WCA | WCA |
| 10 | Gor et al. ²⁵⁸ | QSDFT | N ₂ | Carbon | Cage-like, channel-like, cylindrical, spherical | 77.4 | 0–1.01 | FMT | WCA | N/A |
| 11 | Firouzi et al. ²⁵⁵ | QSDFT | N ₂ | Silica | Slit | 77 | 0–0.97 | FMT | WCA | WCA |
| 12 | Li et al. ¹⁶⁹²⁴⁹ | NLDFT (Engineering DFT) | N ₂ , hydrocarbons | Graphite | Slit | 77.3 (N ₂), 273.15–363.15 (hydrocarbons) | 0–1 (N ₂), 0–300 (hydrocarbons) | WDA | QDE | Steele 10-4-3 |
| 13 | Liu et al. ^{117,260} | NLDFT (PCSAFT DFT) | CO ₂ , hydrocarbons | Kerogen | Slit | 308–460 | 0–600 | FMT | CK, WDA, TPT1 | Steele 10-4-3 |
| 14 | Sauer and Gross ²⁴⁷ | NLDFT (PCSAFT DFT) | Ar, Kr, hydrocarbons | Graphite | Slit | 100–600 | 0–11.6 | MEMT | WDA, TPT1 | Lj 9-3, Steele 10-4-3 |

^aNos. 1–10 are literatures about using DFT calculate PSD. Nos. 11–13 are examples in the literature that apply NLDFT into confinement conditions. Considering that N₂ and CO₂ are mainly discussed fluids for PSD in this work, Ar used in refs 238, 240, 241, 244, and 245 is not shown in the above table. QDE denotes quadratic density expansion. CK denotes the Chen and Kreglewski model.²⁶¹ WDA denotes weighed density approximation. TPT1 denotes the Wertheim's first-order thermodynamic perturbation theory.²⁶² MEMT denotes the modified FMT.²⁶³

Table 3. Lennard-Jones Parameters for N₂ and CO₂ in NLDFT, QSDFT, and MC Simulations^a

| No. | Authors | Samples | Applied methods | $F_{\text{ex}}^{\text{att}}$ | Models | σ_{ff} (nm) | $\varepsilon_{\text{ff}}/k_{\text{B}}$ (K) |
|-----|------------------------------------|-----------------|-----------------|------------------------------|---------------------|---------------------------|--|
| 1 | Ravikovitch et al. ²⁴² | N ₂ | NLDFT | WCA | Single-site LJ 12-6 | 0.3575 | 94.45 |
| 2 | Gor et al. ²⁵⁸ | N ₂ | QSDFT | WCA | Single-site LJ 12-6 | 0.3549 | 95.77 |
| 3 | Ravikovitch et al. ²⁴⁰ | N ₂ | MC | N/A | Single-site LJ 12-6 | 0.3615 | 101.5 |
| 4 | Tian and Wu ²¹² | N ₂ | MC | N/A | Single-site LJ | 0.3572 | 93.98 |
| 5 | Maddox et al. ²⁶⁴ | N ₂ | MC | N/A | Single-site LJ 12-6 | 0.375 | 95.2 |
| 6 | Sweatman and Quirke ²⁶⁵ | N ₂ | MC | N/A | Multisite LJ | 0.333 | 34.4 |
| 7 | Do and Do ²⁶⁶ | N ₂ | MC | N/A | Multisite LJ 12-6 | 0.332 | 36.4 |
| 8 | Potoff and Siepmann ²⁶⁷ | N ₂ | MC | N/A | Multisite LJ 12-6 | 0.331 | 36 |
| 9 | Ravikovitch et al. ²⁴² | CO ₂ | NLDFT | WCA | Single-site LJ 12-6 | 0.3454 | 235.9 |
| 10 | Sweatman and Quirke ²⁶⁵ | CO ₂ | MC | N/A | Multisite LJ | C: 0.275 O: 0.3015 | C: 28.3 O: 81.0 |

^aNote that the literatures not specifying LJ interaction potential types did not disclose the details.

$$F_{\text{ex}}^{\text{rep}}[\rho_{\text{f}}(\mathbf{r})] = k_{\text{B}}T \int d\mathbf{r}' \Phi[n_{\alpha}(\mathbf{r})] \quad (14)$$

where $\Phi[n_{\alpha}(\mathbf{r})]$ is the excess hard-sphere free energy density, which is a functional of weighted densities $n_{\alpha}(\mathbf{r})$, given as

$$\begin{aligned} \Phi[n_{\alpha}(\mathbf{r})] = & n_0 \ln(1 - n_3) + \frac{n_1 n_2 - \mathbf{n}_{V1} \cdot \mathbf{n}_{V2}}{1 - n_3} \\ & + \frac{\frac{1}{3} n_2^3 - n_2 (\mathbf{n}_{V2} \cdot \mathbf{n}_{V2})}{8\pi(1 - n_3)^2} \end{aligned} \quad (15)$$

where n_0 , n_1 , n_2 , n_3 , \mathbf{n}_{V1} , and \mathbf{n}_{V2} are weighted densities (details can be found in Ravikovitch et al.²⁴²).

For the attractive term $F_{\text{ex}}^{\text{att}}[\rho_{\text{f}}(\mathbf{r})]$, the mean-field approximation (MFA) has been widely used in PSD characterization

$$F_{\text{ex}}^{\text{att}}[\rho_{\text{f}}(\mathbf{r})] = \frac{1}{2} \iint d\mathbf{r} d\mathbf{r}' \rho_{\text{f}}(\mathbf{r}) \rho_{\text{f}}(\mathbf{r}') u_{\text{att}}^{\text{ff}}(|\mathbf{r} - \mathbf{r}'|) \quad (16)$$

where $u_{\text{att}}^{\text{ff}}$ is the fluid–fluid interaction potential, which is given as the Weeks–Chandler–Andersen (WCA) scheme²⁵¹ of the LJ potential

$$u_{\text{att}}^{\text{ff}} = \begin{cases} -\varepsilon_{\text{ff}}, & |\mathbf{r} - \mathbf{r}'| < 2^{1/6} \sigma_{\text{ff}} \\ u^{\text{ff}}(|\mathbf{r} - \mathbf{r}'|), & |\mathbf{r} - \mathbf{r}'| \geq 2^{1/6} \sigma_{\text{ff}} \end{cases} \quad (17)$$

where ε_{ff} and σ_{ff} are the LJ energy and size parameters, respectively. For PSD characterization, the LJ 12-6 interaction potential is usually applied for $u^{\text{ff}}(|\mathbf{r} - \mathbf{r}'|)$ as in eq 17. It is worth noting that various LJ parameters are available for N₂ and CO₂ as shown in Table 3. Therefore, specifying the LJ parameters used in the MFA is essential for accurate PSD characterization by using NLDFT.

The external fluid–solid potential $U_{\text{ext}}(\mathbf{r})$ is another key parameter for PSD characterization. Various models are available depending on the surface type and geometry. As shown in Figure 11, slit pores consisting of three-layer graphene sheets have been widely used to represent carbonaceous

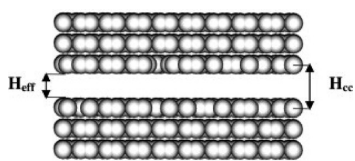


Figure 11. Schematic representation of carbon-slit pore. Reproduced from Lucena et al.²⁵² with permission. Copyright (2010) Elsevier.

materials, such as activated carbon. In Ravikovitch et al.,²⁴² the Steel 10-4-3 potential is used to model the fluid–surface potential in carbon slit pores, in which the potential only varies in the z -direction perpendicular to the pore surface

$$U_{\text{fs}}(z) = 2\pi\rho_s\varepsilon_{\text{fs}}\sigma_{\text{fs}}\Delta \left[\left(\frac{\sigma_{\text{fs}}}{z} \right)^{10} - \left(\frac{\sigma_{\text{fs}}}{z} \right)^4 - \frac{\sigma_{\text{fs}}^4}{3\Delta(0.61\Delta + z)^3} \right] \quad (18)$$

where $\rho_s = 0.114 \text{ \AA}^{-3}$ is the carbon number density of in graphene, $\Delta = 3.35 \text{ \AA}$ is the interlayer spacing, and $\varepsilon_{\text{fs}} = \sqrt{\varepsilon_f \varepsilon_s}$ and $\sigma_{\text{fs}} = (\sigma_f + \sigma_s)/2$ are the energy and size parameters of the fluid–surface interaction, respectively. The energy and size parameters of graphite surface are given as $\sigma_s = 0.3345 \text{ nm}$ and $\varepsilon_s/k_{\text{B}} = 28 \text{ K}$, respectively. Then, the external potential $U_{\text{ext}}(z)$ is given as

$$U_{\text{ext}}(z) = U_{\text{fs}}(z) + U_{\text{fs}}(H - z) \quad (19)$$

where H is the slit pore width.

However, in silica-based porous media (such as MCM-41) with a cylindrical pore geometry, the external potential is described by the LJ 10-4 potential²⁴²

$$\begin{aligned} U_{\text{ext}}(r, R) = & \pi^2 \rho_s^2 \varepsilon_{\text{fs}} \sigma_{\text{fs}}^2 \left\{ \frac{63}{32} \left[\frac{R-r}{\sigma_{\text{fs}}} \left(1 + \frac{r}{R} \right) \right]^{-10} \right. \\ & \times F \left[-\frac{9}{2}, -\frac{9}{2}; 1; \left(\frac{r}{R} \right)^2 \right] - 3 \left[\frac{R-r}{\sigma_{\text{fs}}} \left(1 + \frac{r}{R} \right) \right]^{-4} \\ & \left. \times F \left[-\frac{3}{2}, -\frac{3}{2}; 1; \left(\frac{r}{R} \right)^2 \right] \right\} \end{aligned} \quad (20)$$

where r is the radial coordinate of fluid from the pore center, R the radial coordinate of the pore center, and $F[\alpha, \beta; \gamma; \delta]$ the hypergeometric series. The surface density ρ_s is given as 0.153 \AA^{-2} for silica surface. The energy and size parameters of the fluid–surface interaction in eq 20 are $\varepsilon_{\text{fs}} = \sqrt{\varepsilon_f \varepsilon_s}$ and $\sigma_{\text{fs}} = (\sigma_f + \sigma_s)/2$ with $\sigma_s = 0.2765 \text{ nm}$ and $\varepsilon_s/k_{\text{B}} = 229.722 \text{ K}$ for silica.

Generally, PSD can be automatically fitted from experimentally measured adsorption/desorption isotherms by using commercial software such as Autosorb-1²⁵³ and Micromeritics ASAP-2460.²⁰⁶ However, as discussed above, the accurate excess Helmholtz free energy (arising from fluid–fluid interaction) and external potential (arising from fluid–surface interaction) terms are essential. There are several different approximations available for each excess Helmholtz free energy term, and the expression for the external potential is also

dependent on the geometry and rock type. Ravikovitch and Neimark²⁵⁰ used NLDFT to calculate PSD in siliceous mesoporous material SBA-15, which consists of a series of cylindrical pores. The calculated PSD is found to be in a good agreement with geometrical considerations and XRD data. However, unlike SBA-15 with a well-defined pore geometry consisting of a uniform material, the rock heterogeneity and different pore geometries in shale media are evident as we discussed in Section 2. The kernel of NLDFT is built upon the types of adsorbate, adsorbent, and pore shape as well as various approximations and assumptions, while the pore surface is generally assumed as a smooth one consisting of a single-type material with a predetermined shape. Wang and Ju⁵⁸ tested the PSD of shale samples obtained from NLDFT in which both carbon and silica are considered as adsorbents. They also considered various pore shapes including slit, cylinder, and sphere. They found drastically different PSDs by using various kernels.

In addition, the quenched solid density functional theory (QSDFT) is another popular choice for PSD analysis, in which the pore surface is integrated as one of the components. In QSDFT, the grand potential of both fluid and solid $\Omega_{fs}[\rho_f(\mathbf{r}), \rho_s(\mathbf{r})]$ are considered^{238,241}

$$\begin{aligned} \Omega_{fs}[\rho_f(\mathbf{r}), \rho_s(\mathbf{r})] = & F_{id}[\rho_f(\mathbf{r})] + F_{id}[\rho_s(\mathbf{r})] + F_{ex}[\rho_f(\mathbf{r}), \rho_s(\mathbf{r})] \\ & + \frac{1}{2} \iint d\mathbf{r}d\mathbf{r}' \rho_f(\mathbf{r})\rho_f(\mathbf{r}')u_{att}^{ff}(|\mathbf{r} - \mathbf{r}'|) \\ & + \frac{1}{2} \iint d\mathbf{r}d\mathbf{r}' \rho_s(\mathbf{r})\rho_s(\mathbf{r}')u_{att}^{ss}(|\mathbf{r} - \mathbf{r}'|) \\ & + \frac{1}{2} \iint d\mathbf{r}d\mathbf{r}' \rho_f(\mathbf{r})\rho_s(\mathbf{r}')u_{att}^{fs}(|\mathbf{r} - \mathbf{r}'|) - \mu_f \int d\mathbf{r}\rho_f(\mathbf{r}) \\ & - \mu_s \int d\mathbf{r}\rho_s(\mathbf{r}) \end{aligned} \quad (21)$$

where $\rho_s(\mathbf{r})$ is the density profile of solid components, $F_{id}[\rho_s(\mathbf{r})]$ the ideal term of hard-sphere free energy of solid components, $F_{ex}[\rho_f(\mathbf{r}), \rho_s(\mathbf{r})]$ the excess hard-sphere repulsive term for both fluid and solid components, $u_{att}^{ss}(|\mathbf{r} - \mathbf{r}'|)$ and $u_{att}^{fs}(|\mathbf{r} - \mathbf{r}'|)$ the attractive parts of solid–solid and solid–fluid potentials, respectively, and μ_s the solid chemical potential.

At equilibrium, the grand potential of both fluid and solid, $\Omega_{fs}[\rho_f(\mathbf{r}), \rho_s(\mathbf{r})]$, reaches minimum. Usually, it is assumed that solid component only affects $F_{ex}[\rho_f(\mathbf{r}), \rho_s(\mathbf{r})]$ during grand potential minimization. Then, the fluid distribution is given as

$$\begin{aligned} \rho_f(\mathbf{r}) = & \Lambda_f^{-3} \exp\left(-\frac{\beta\delta F_{ex}[\rho_f(\mathbf{r}), \rho_s(\mathbf{r})]}{\delta\rho_f(\mathbf{r})}\right. \\ & \left.- \beta \int d\mathbf{r}' \rho_f(\mathbf{r}')u_{att}^{ff}(|\mathbf{r} - \mathbf{r}'|) + \beta\mu_f\right. \\ & \left.- \beta \int d\mathbf{r}' \rho_s(\mathbf{r}')u_{att}^{fs}(|\mathbf{r} - \mathbf{r}'|)\right) \end{aligned} \quad (22)$$

QSDFT is a powerful tool to consider the geometrical heterogeneity of pore walls, and roughness parameter is implemented to describe surface corrugation.²⁵⁴ The applications of QSDFT in shale rock characterizations have also been reported in previous works,^{58,254–256} but a systematic calibration is limited.

Collectively, while NLDFT and QSDFT have been considered as the golden standard for PSD characterization as they can explicitly consider fluid–fluid and fluid–surface interactions and have shown excellent agreement with

experimental measurements in terms of carbonaceous and siliceous materials, attention and care should be paid when applying them to characterize PSD in shale. Using different pore geometries and types would provide largely different PSD characterizations. The fluid–surface interaction parameters for some minerals such as clay and carbonates have not been developed yet, while their interactions with N_2 and CO_2 might be different from those from siliceous materials. In addition, as CO_2 carries a quadruple moment, its interaction with some pore surfaces such as clay with heteroatoms²⁵⁷ may not be simply described by LJ-type interactions. Various pore geometries and inherent rock heterogeneity in shale media also make using a uniform pore geometry and a uniform pore type in NLDFT unjustifiable for shale PSD characterization, which has been the common practice. Even from the perspective of using NLDFT and QSDFT to provide qualitative PSD quantifications in shale, we would strongly urge the researchers to provide the details about the used parameters and approximations, as they are generally not provided. There are different versions of parameters and approximations available for NLDFT and QSDFT for PSD characterizations, while some variations in these factors might result in drastically different PSDs.

4. METHANE STORAGE MECHANISMS IN SHALE NANOPOROUS MEDIA

Methane storage (sorption) mechanisms in shale nanoporous media can be separated into three different forms: free gas, adsorbed gas, and absorbed gas.³⁰ The free gas is a bulk-like gas stored in fractures and macropores as well as in the middle of some mesopores. Adsorbed gas refers to the gas molecules physically adsorbed on the pore surface of organic and inorganic matters. Thanks to the extensive amount of nanoscale pores in shale media, the adsorbed gas which generally has a higher density than the free gas⁹⁹ can contribute up to 85% of total GIP in shale. Therefore, the knowledge about methane adsorption capacity in shale is imperative to both GIP estimation and well productivity.¹²² The absorbed gas depicts the dissolved gas within the kerogen matrix. While shale gas can contain other heavier hydrocarbons such as ethane and propane,²⁴ in this section, we mainly focus on methane adsorption capacity as it is the predominant constituent of shale gas.

There have been extensive experimental measurements on the methane adsorption capacity in shale, and the effects of pressure,^{87,268} temperature,^{269,270} moisture content,^{172,271} rock compositions^{114,164} (e.g., organic and inorganic matters, kerogen type, and maturity), and pore structures^{71,146} have been explored. A more detailed review about methane adsorption in shale and controlling factors can be referred to Memon et al.,¹¹⁰ Rani et al.,²⁷² and Wang et al.¹²³ Methane absorption in a kerogen matrix has gradually attracted attention from scientists and engineers in recent years.^{156,164} It has been reported that the absorbed gas in kerogen can contribute up to 22% to total GIP in Barnett shale samples.²⁷³ The sorption-induced kerogen swelling behavior has also been reported.¹¹³ Chen et al.²⁷⁴ measured methane sorption-induced swelling on shale samples from the Lower Cambrian Niutitang Formation and found that the volumetric strain can be up to 0.1% at 10 MPa and 298 K. Huang et al.²⁷⁵ measured the swelling behavior of Kimmeridge kerogen in various hydrocarbons including normal-alkanes, naphthenes and aromatics. They found that kerogens in the normal-alkanes and aromatics have a higher swelling ratio than those in naphthenes due to the flexible structure of carbon chains and π - π interactions with kerogen, respectively.

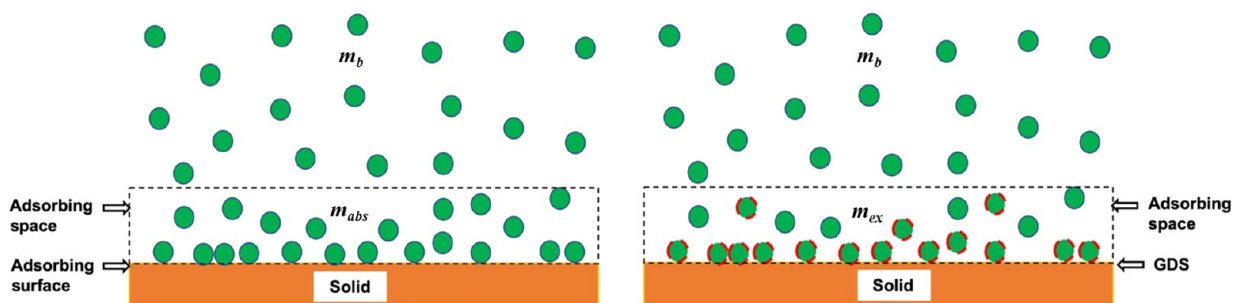


Figure 12. Schematic representation of excess and absolute adsorption. GDS is Gibbs dividing surface; m_b , m_{ex} and m_{abs} are free gas amount, excess adsorption, and absolute adsorption, respectively. The green circles represent the adsorbate molecules, and the red dashed outlines represent m_{ex} . Reproduced from Xiong et al.¹⁰⁸ with permission. Copyright (2020) Elsevier.

Molecular simulations such as MD and GCMC have been applied to study kerogen swelling behavior due to methane sorption.^{121,224,276,277} Huang et al.^{121,278} performed MD and GCMC simulations on kerogen deformation induced by gas sorption considering moisture content, kerogen type, maturity, and competitive adsorption. They found that the volumetric strain is influenced by both the pore shrinkage effect due to mechanical compression and the sorption-induced swelling effect¹²¹ as well as the coupling effect of moisture, resulting in kerogen swelling magnitude in the order of Type IA > Type IIA > Type IIIA.²⁷⁸ Ho et al.²⁷⁶ studied the CH₄ and CO₂ sorptions in a flexible Type II-D kerogen matrix at 300 K and pressure up to 192 atm by using a hybrid MC/MD simulation. The simulation is performed under a zero effective stress condition. They found that the kerogen volume expands up to 5.4% and 11% due to CH₄ and CO₂ sorption, respectively. Tesson and Firoozabadi²²⁴ studied methane sorption in flexible and rigid kerogen (Type II-A) slit pores using a hybrid MD-MC simulation at 333.15 K and pressure up to 400 atm. They found that the dynamic system is affected by both gas adsorption and matrix deformation. The methane-accessible surface area in flexible kerogen increases with pressure, while it is higher than that in a rigid system. Moreover, the sorption capacity in a flexible system is 57% higher than that in a rigid system.

Currently, the vast majority of experimental measurements are conducted to quantify methane adsorption capacity in shale media, as adsorption is the predominant storage mechanism,²⁷⁹ while it is difficult to distinguish methane adsorption and absorption via experimental measurements.²⁷³ However, the directly measured adsorption capacity usually corresponds to excess adsorption, while the absolute adsorption which represents the adsorbed gas capacity^{108,279} needs to be converted from the excess adsorption. Different methods such as Langmuir,^{125,280} supercritical Dubinin–Radushkevich (SDR),^{98,99} supercritical BET,^{102,103} simplified local-density (SLD)^{104,105}, and molecular simulations such as GCMC^{115,116,281} and MD^{282,283} have been applied to describe the absolute adsorption. In Section 5, we explicitly discuss the current state-of-the-art methane adsorption measurements in shale from a *macroscopic* perspective and the understanding from molecular simulations from a *microscopic* perspective as well as various excess-adsorption-to-absolute-adsorption conversion methods.

5. METHANE EXCESS ADSORPTION AND ABSOLUTE ADSORPTION: MEASUREMENT, SIMULATION, AND CONVERSION

In this section, we first discuss experimental measurements on methane adsorption in shale nanoporous media which is the excess adsorption from a *macroscopic* perspective. Then, we illustrate methane adsorption behaviors in shale nanoporous media from a *microscopic* perspective according to molecular simulations which can explicitly consider fluid–fluid and fluid–surface interactions. We note that our brief review about experimental measurements and molecular simulations intends to provide basic backgrounds about the conversion of experimentally measured excess adsorption to the absolute adsorption. More details about these two parts can be referred to other review works.^{284–286} Thereafter, we discuss various excess-adsorption-to-absolute-adsorption conversion methods. We conclude this section by briefly summarizing some key issues in these conversion methods and remaining challenges.

5.1. Experimental Measurements on Methane (Excess) Adsorption in Shale. Before moving onto the adsorption measurements, it is necessary to discuss the concepts of two different adsorption quantities: excess adsorption and absolute adsorption. As shown in Figure 12, the excess adsorption (m_{ex}) represents the difference between the total number of gas molecules in the system (m_{tot}) and the number of molecules that would occupy the accessible pore space under a free gas condition at the given temperature and pressure.²⁸⁶ The absolute adsorption (m_{abs}) which includes all the adsorbate molecules in the characterized adsorbed phase represents the adsorbed gas capacity. Assuming the generally used methane monolayer adsorption model²⁷⁹ as shown in Figure 13, m_{ex} is related to m_{abs} by

$$m_{ex} = m_{tot} - V_{void}\rho_b = m_{abs} - V_a\rho_b \quad (23)$$

or

$$m_{ex} = m_{abs} \left(1 - \frac{\rho_b}{\rho_a} \right) \quad (24)$$

where V_{void} , V_a , ρ_a , and ρ_b represent the void (pore) volume, adsorbed phase volume, adsorbed phase density, and adsorbate bulk density, respectively. In general, ρ_a is higher than ρ_b .²⁷⁹ At low pressures, the difference between m_{ex} and m_{abs} is negligible due to the small ρ_b .^{125,286} However, under the *in situ* conditions (high pressure and high temperature), the differences between m_{ex} and m_{abs} become significant as ρ_b becomes no longer negligible (as shown in eq 23) and comparable to ρ_a (as shown in eq 24).^{87,280} While m_{ex} and ρ_b can be obtained from

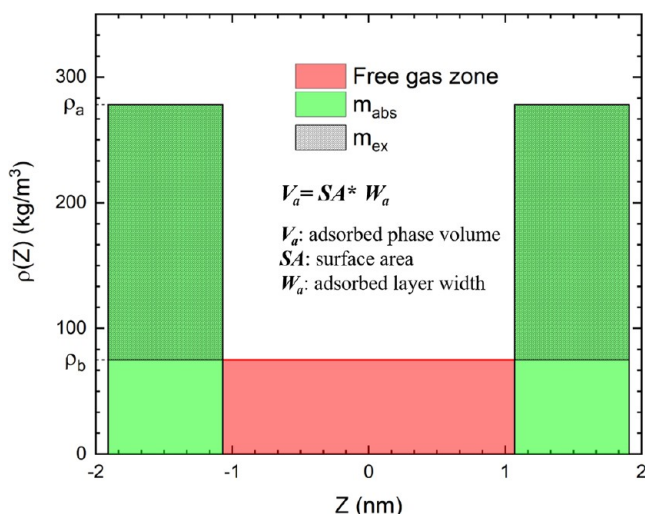


Figure 13. Schematic representation of methane monolayer adsorption model in a 4 nm slit pore, where V_a is the adsorbed phase volume, SA is the surface area and W_a is the adsorption layer width. Reproduced from Pang and Jin²⁷⁹ with permission. Copyright (2019) Elsevier.

experimental measurements and EOS modeling, respectively, neither ρ_a or V_a is directly available.

Two popular experimental measurements have been widely conducted to quantify m_{ex} in shale samples: volumetric^{164,269,287} and gravimetric^{78,112,288} methods. The gravimetric method is used to measure the adsorption amount according to the difference between buoyancy and gravity of the sample mass by microbalance.⁹⁹ The gravimetric method has the advantage of being highly accurate, while the sample size should be small.¹⁶⁴ In addition, it is generally conducted at moderate pressures.²⁸⁶ The volumetric method is more accurate at low pressure conditions.²⁸⁶ Moreover, the volumetric method is favorable in the oil/gas industry because large samples can be used in the measurements which can take into account the reservoir rock heterogeneity.⁹⁹

A schematic representation of the gravimetric measurement setup¹¹³ is shown in Figure 14, while the details can be referred

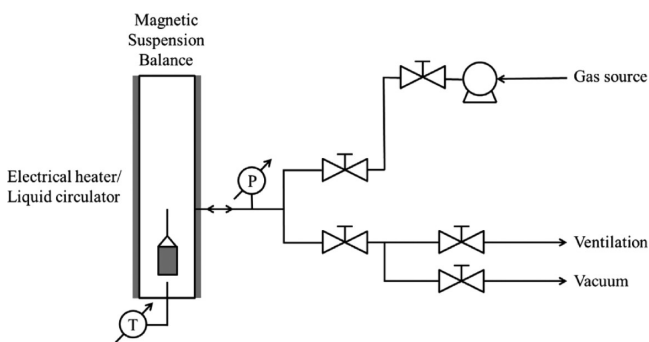


Figure 14. Schematic representation of gravimetric method. Reproduced from Zhao et al.¹¹³ with permission. Copyright (2018) Elsevier.

to Zhao et al.¹¹³ The gravity force (F_A) and buoyancy force (F_B) can be given as

$$\begin{cases} F_A = (m^{SC} + m^S + m^A)g \\ F_B = (V^{SCC} + V^S + V^A)\rho_b g \end{cases} \quad (25)$$

where m^{SC} , m^S , and m^A are the weight of the empty sample container, weight of the loaded sample, and weight of the absolute adsorption, respectively; V^{SC} , V^S , and V^A are the volume of the empty sample container, volume of the sample, and volume of the adsorbed phase, respectively; ρ_b and g are bulk adsorbate density and gravity acceleration, respectively. The m^S and V^S can be determined by helium gas at 333 K and elevated pressures up to 100 bar.^{87,113} Therefore, the balance reading (Δm) is given as

$$\begin{aligned} \Delta m &= (F_A - F_B)/g \\ &= m^{SC} + m^S + m^A - (V^{SC} + V^S + V^A)\rho_b \end{aligned} \quad (26)$$

and the mass of absolute adsorption can be calculated as

$$m^A = \Delta m - m^{SC} - m^S + (V^{SC} + V^S + V^A)\rho_b \quad (27)$$

Since V^A cannot be directly measured from experiments,⁸⁰ by applying the correlation based on eq 23, m_{ex} is given as

$$m_{ex} = m^A - V^A\rho_b = \Delta m - m^{SC} - m^S + (V^{SCC} + V^S)\rho_b \quad (28)$$

On the other hand, the volumetric method is based on Boyle's volumetric gas expansion law. The system consists of the reference cell and sample cell connected by a valve, and a temperature bath is used to control the temperature of system, as shown in Figure 15.¹⁶⁴ The reference cell has a known volume of

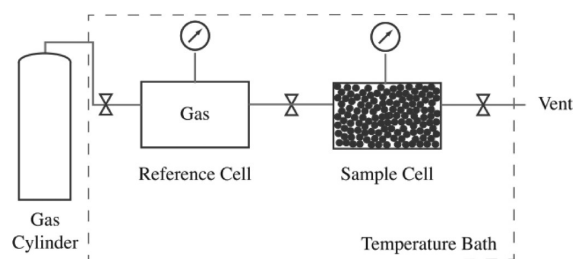


Figure 15. Schematic representation of volumetric method. Reproduced from Heller and Zoback¹⁶⁴ with permission. Copyright (2014) Elsevier.

V_R and stores adsorbate, which is pressurized and heated to the target condition. The sample cell with known volume of V_S contains the adsorbent. During the volumetric experiment process, the connected valve is opened once the sample cell is pressurized, and the gas is expanded to the sample cell. Once the pressure becomes equilibrated, the isothermal adsorption reaches equilibrium, and then, the adsorption amount can be obtained.

During the volumetric measurement, a given amount of adsorbate is loaded into the reference cell of known volume (V_R) at given pressure P . The total amount of fluid in the reference cell m_R is given as

$$m_R = \frac{PV_R}{ZRT} \quad (29)$$

where Z , R , and T are the compressibility factor, universal gas constant, and temperature, respectively. The void volume in the sample cell is measured by the helium expansion method, based on the assumption that helium is a nonadsorbing gas.²⁸⁹ Therefore, the void volume in sample cell V_{S_void} can be obtained by

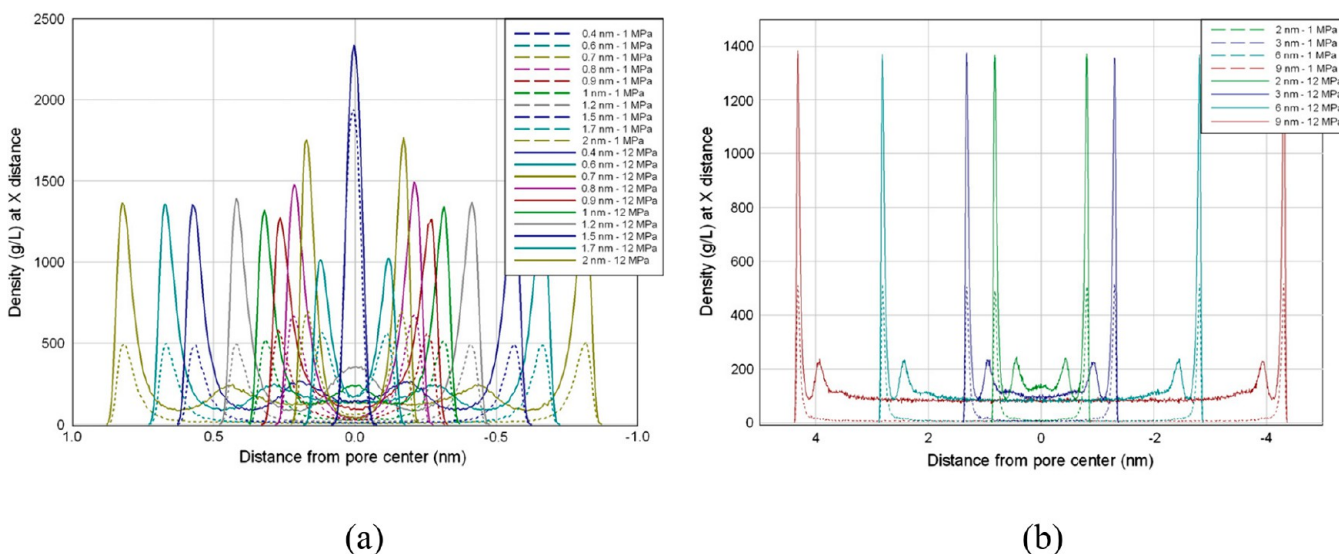


Figure 16. Methane density distributions in carbon slit pores of pore widths (a) from 0.4 to 2 nm and (b) from 2 to 9 nm at 10 and 12 bar as well as 298 K. Reproduced from Mosher et al.¹¹⁶ with permission. Copyright (2013) Elsevier.

$$V_{S_void} = \frac{m_R Z' RT'}{P'} - V_R \quad (30)$$

where Z' , P' , and T' are the compressibility factor, pressure, and temperature after opening the valve via the subsequent pressure drop process, respectively.¹⁶⁴ The compressibility factors of the pure gases can be obtained from the equations of state.^{290,291} When the system reaches equilibrium, m_{ex} can be obtained from m_R and the amount of free gas that can occupy in the reference cell and void volume of sample cell

$$m_{ex} = m_R - \frac{P_2(V_R + V_{S_void})}{RT_2 Z_2} \quad (31)$$

Do et al.²⁹² emphasized the importance of determining V_{S_void} accurately and stated that the helium adsorption-based V_{S_void} generally overestimates the true pore volume as helium adsorption likely occurs in ultrafine pores. At high pressures, the overestimation of V_{S_void} can lead to an even negative m_{ex} value.²⁹³ Ross and Bustin²⁹⁴ reported the phenomenon of negative methane m_{ex} in Jurassic and Devonian shales. They argued that it is because while the smaller-sized helium molecules can penetrate into small pores, methane molecules are not accessible to these pores. In addition, the accuracy of measured results needs to be further analyzed by considering the uncertainties arising from experimental design and setup. The errors in pressure determination can arise from either the pressure measurements, which influence the mass balance calculation, or from the gas leakage.²⁸⁵ Belmabkhout et al.²⁸⁵ found that an absolute error of 8 kPa can lead to a relative error between 8.4% and 42.7% in adsorption capacity in activated carbons at 303 K. Thus, they recommended to adopt a pressure transducer to minimize the relative error. For gas leakage, a safe leakage rate under 4.5×10^{-4} mol/h is suggested for the low adsorbate system (mass uptake under 0.1 g/g) to reduce the relative error. A detailed review about experimental uncertainties can be referred to Mohanmmad et al.²⁹⁵ and Sircar et al.²⁹⁶

In summary, both gravimetric and volumetric methods measure gas adsorption in shale nanoporous media from a *macroscopic* perspective, providing m_{ex} . However, as discussed above, the working mechanisms for these two approaches are

different. In addition, whole shale samples containing both organic and inorganic matters have been widely used to measure adsorption capacity.^{172,181,297,298} While there have been experimental works separating various constituents in shale samples to measure gas adsorption in each of them,^{150,259} a precise control of PSD cannot be achieved. As methane adsorption in shale nanoporous media strongly depends on rock type²⁴ and PSD,¹¹⁶ it is imperative to combine the *macroscopic* experimental measurements with the *microscopic* molecular modeling and simulation approaches which can explicitly consider fluid–fluid and fluid–surface interactions.

5.2. Molecular Simulations on Methane Adsorption Behaviors in Shale. Molecular modeling and simulations have gained much attention in the past decade in the studies of methane adsorption in shale nanoporous media, as they can explore the length scale which is not accessible to experimental measurements. In micropores and mesopores, as methane molecular size is comparable to the pore size, fluid–surface interactions play an important role, and fluid distributions are inhomogeneous.¹¹⁶ Molecular simulations can explicitly consider intermolecular interactions to account for the rock type²⁴ and pore size,¹¹⁶ making it a powerful tool in this endeavor.

GCMC and MD simulations have been widely applied to study fluid adsorption^{120,299,300} and flow^{301–303} in shale nanoporous media. The pore size effect on methane adsorption has been studied by a number of works.^{114,116,304,305} Mosher et al.¹¹⁶ carried out GCMC simulations on methane adsorption in carbon slit pores at various temperatures and pressures up to 200 bar. As shown in Figure 16, methane density distributions in micropores and mesopores are inhomogeneous and render drastically different adsorption behaviors. In micropores, methane has prominent layering structures due to the overlap of fluid–surface interactions; in mesopores, it has a strong first adsorption layer and a weak second adsorption layer, while its density in the middle of the pores regresses to the bulk density. Tian et al.⁹⁹ argued that the second adsorption layer should be treated as the transition zone which has a higher density than the free gas density for the conversion of m_{ex} to m_{abs} , as shown in Figure 17. As methane adsorption behaviors are strongly dependent on pore size, Pang et al.^{88,100,122} claimed that it is

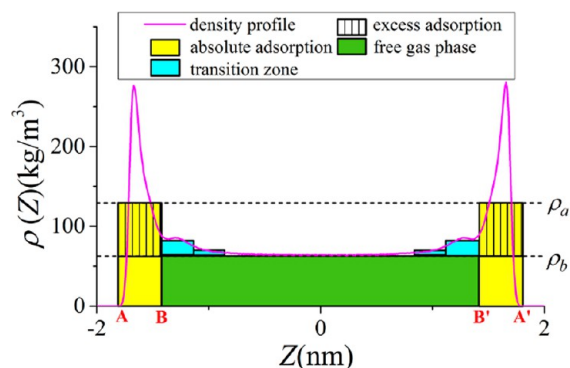


Figure 17. Schematic representation of transition zone in 4 nm illite slit pore from methane density profile at 333.15 K and 10 MPa. The heights of characterized phases are calculated from the integration of density profiles. Reproduced from Tian et al.⁹⁹ with permission. Copyright (2017) Nature.

imperative to consider PSD for methane m_{abs} characterization in kerogen nanoporous media. On the other hand, it has been reported that while m_{ex} per unit surface area is dependent on the pore width in micropores, it becomes insensitive to pore width in mesopores.^{100,304}

Rock compositions,¹¹⁴ moisture,^{28,306} and surface roughness and chemistry^{50,305} can also play important roles in methane adsorption in nanoporous media. Xiong et al.¹¹⁴ performed GCMC simulations to study methane adsorption in carbon, clay (e.g., illite and montmorillonite), and quartz slit pores. The adsorption capacity decreases in the order of organic > clay > quartz. In general, methane adsorption capacity in shale is positively correlated with TOC,²³ while it has been shown that clay content contributes to the total adsorption in organic-rich as well as clay-rich shales.^{23,29} In addition, a number of works have been reported on the effect of rock composition on pore structures.^{160,178} On one hand, as shown in Figure 18(a) and (b), micropore volume and SSA have positive correlations with

TOC in organic-rich shale, indicating that microporosity is mainly developed in organic matter, while the clay minerals contribute to mesopore volume.¹⁶⁰ However, in some translational shale samples, as shown in Figure 19, the micropores are

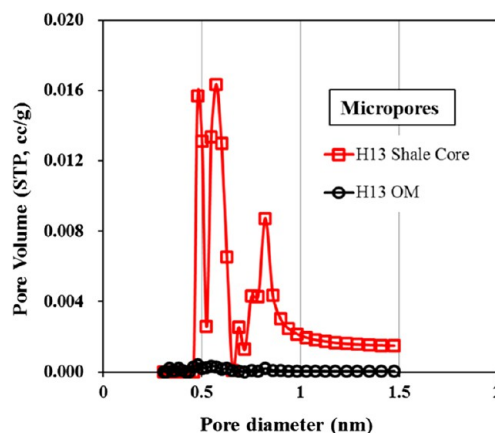


Figure 19. PSD in micropore range in translational shale and isolated kerogen samples from Ordos Basin. Reproduced from Xiong et al.¹⁵⁰ with permission. Copyright (2017) Elsevier.

mainly developed in inorganic matter, especially in clay minerals.¹⁵⁰ In addition, as depicted in Figure 20, the presence of clay minerals can contribute to micropore and mesopore SSA in various shale samples. The predicted maximum adsorption capacities from the Langmuir model in shale samples are related to TOC and clay contents as shown in Figure 21(a). In addition, the relationship of the mesopore surface area from N_2 adsorption and micropore volume from CO_2 adsorption show a positive relationship with predicted capacity as shown in Figure 21(b). We note that while the maximum adsorption capacities obtained from the Langmuir model may not provide the actual maximum loadings, they can qualitatively show the potential of gas adsorption in porous media. On the other hand,

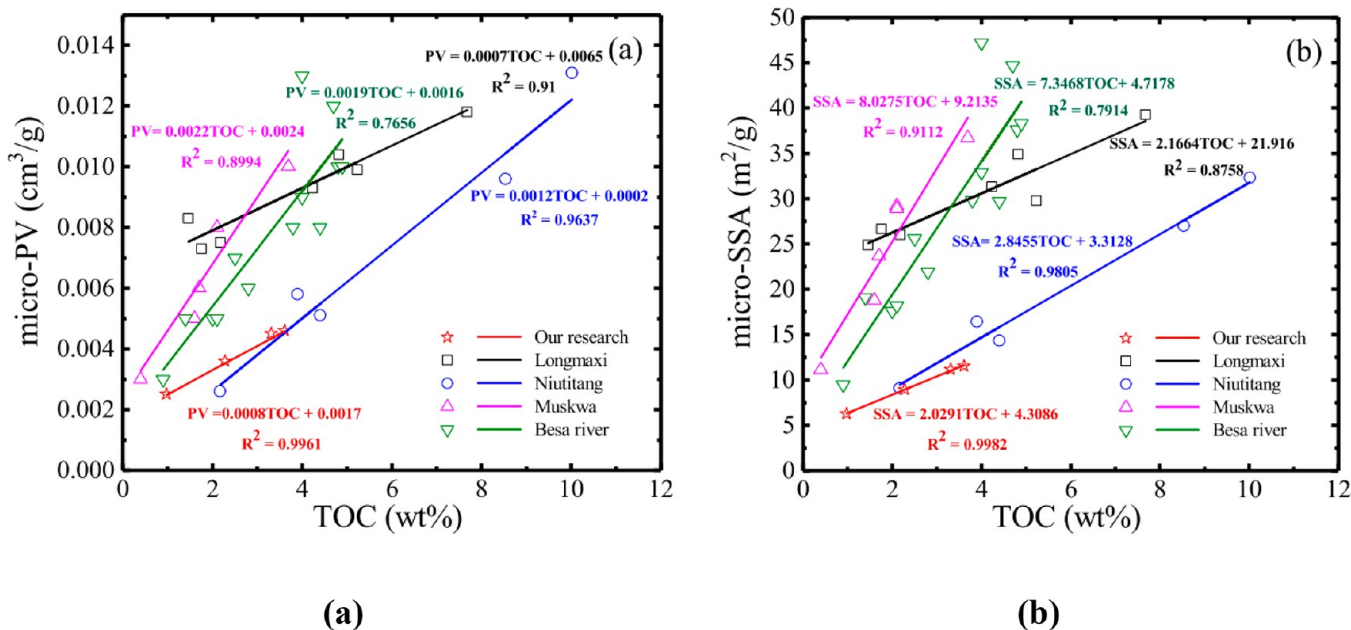


Figure 18. Relationship of micropore and mesopore structure with TOC for various formations. (a) Relationship of micropore pore volume with TOC. (b) Relationship of micropore SSA with TOC. Reproduced from Wu et al.⁷¹ with permission. Copyright (2020) American Chemical Society.

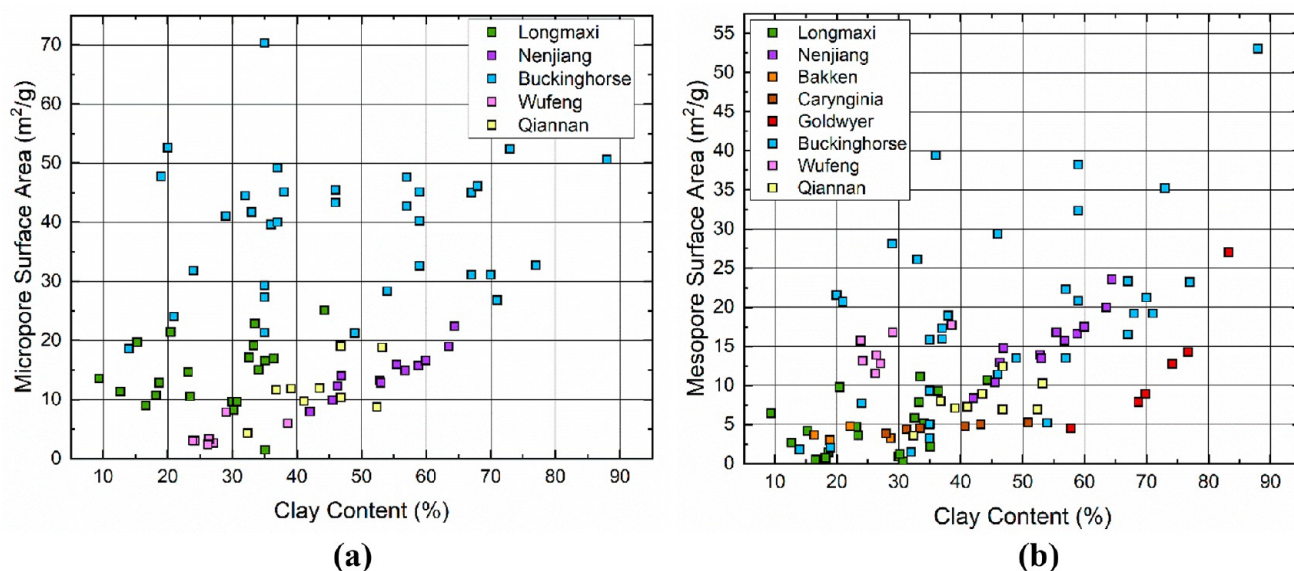


Figure 20. Relationship of clay content with (a) micropore SSA and (b) mesopore SSA in various shale samples: Longmaxi (data from Zhu et al.³⁰⁸), Nenjiang (data from Zhang et al.³⁰⁹), Buckingham (data from Chalmers and Bustin¹⁷⁵), Wufeng (data from Xiong et al.³²), Qiannan (data from Tian et al.³¹⁰), Bakken (data from Yuan et al.¹⁶⁰), Carynginia (data from Yuan et al.¹⁶⁰), and Goldwyer (data from Yuan et al.¹⁶⁰).

methane adsorption capacities in organic and inorganic matters vary as reported in a number of experimental works. In Table 4, we summarize the measured methane excess adsorption amounts in isolated kerogen and pure clay minerals (including organic-matter-free clay-mineral-dominated rocks). It is shown that the gas adsorption capacity in organic matter is generally larger than that in inorganic matter.^{29,70,307} In addition, molecular simulations show that the methane maximum excess adsorptions in carbon micropores and mesopores at 333.15 K are within the range of 0.0036–0.006 mmol/m²,¹⁰⁰ while those in illite are within the range of 0.0017–0.0024 mmol/m².⁹⁹ Similar observations have been reported as listed in Table 5. Collectively, both rock type and pore size play important roles in estimating methane adsorption capacity in shale.

In addition, Jin and Firoozabadi reported that the presence of water in clay nanopores can greatly reduce methane adsorption by occupying the adsorption sites.³⁰⁶ Other simulation works reported that the decrease in gas adsorption capacity is mainly due to the preferential adsorption of water on oxygen-containing groups in kerogen.^{119,320–322} The reduction in gas adsorption capacity increases as water content increases.³²² In addition, such reduction is significant in low-maturity kerogens, which contain more hydrophilic functional groups promoting the formation of water clusters to block the small pores.^{119,323} There have been a number of GCMC simulation studies on methane adsorption in kerogen nanopores with rough surfaces.^{28,120,121,224,278,324,325} Tesson and Firoozabadi reported that the strong methane first adsorption layer might disappear on kerogen surface with a high degree of roughness.²²⁴ Water can form hydrogen bonding with kerogen surface functional groups to reduce methane adsorption sites,²⁸ while kerogen deformation due to methane adsorption has also been taken into account by molecular simulations.¹²¹ Other factors which can affect methane adsorption in shale nanoporous media including pore shape and structure^{118,326,327} as well as kerogen type and maturity^{321,324,328} have been investigated, while the detailed discussions about the applications of molecular simulations in shale gas studies can also be referred to other review papers.^{123,329}

While molecular simulations can provide important insights into methane adsorption in shale nanoporous media from atomistic and molecular scales, their accuracy is highly dependent on the molecular models and force fields applied to represent fluid–fluid and fluid–surface interactions. Thanks to the development of highly accurate force fields for methane,³³⁰ structural and thermodynamic properties of methane can be well predicted by molecular simulations. However, the current state-of-the-art models and force fields for rock surfaces (such as kerogen, clay, quartz, and carbonates) are either based on simplified surface models (e.g., graphite surface to represent kerogen²⁷⁹) or have not been directly tested against experimental measurements in terms of methane adsorption on a consistent basis. Unlike nanoporous media with well-characterized pore structures and dimensions such as SBA-15³³¹ and MCM-41,²⁶⁴ shale is subject to rock heterogeneity and pore size heterogeneity. It is difficult to conduct experimental measurements on methane adsorption in precisely controlled (PSD and rock type) shale nanoporous media to provide benchmark data for molecular simulations to tune the force fields. Therefore, in the future, it is imperative to have more synergy between experimental measurements and molecular simulations to further advance our understanding toward methane adsorption in shale nanoporous media.

5.3. Excess-Adsorption-to-Absolute-Adsorption Conversion Methods. As both gravimetric and volumetric methods can only measure m_{ex} , one needs to convert the measured m_{ex} to m_{abs} . The excess adsorption amounts vary in different shale samples due to different pore structures and properties, but in general, m_{ex} first increases with pressure then decreases,⁸⁷ as shown in Figure 22. As pressure increases, bulk gas density increases, while the increment in adsorbed gas density is less significant than that in the bulk phase at high pressures.²⁷⁹ On the other hand, m_{abs} monotonically increases with pressures.⁸⁸

It should be noted that in eqs 23 and 24, neither V_a nor ρ_a can be directly measured from experiments.^{125,164,279} One needs to make certain assumptions to convert the experimentally measured m_{ex} to m_{abs} . In terms of the conversion methods

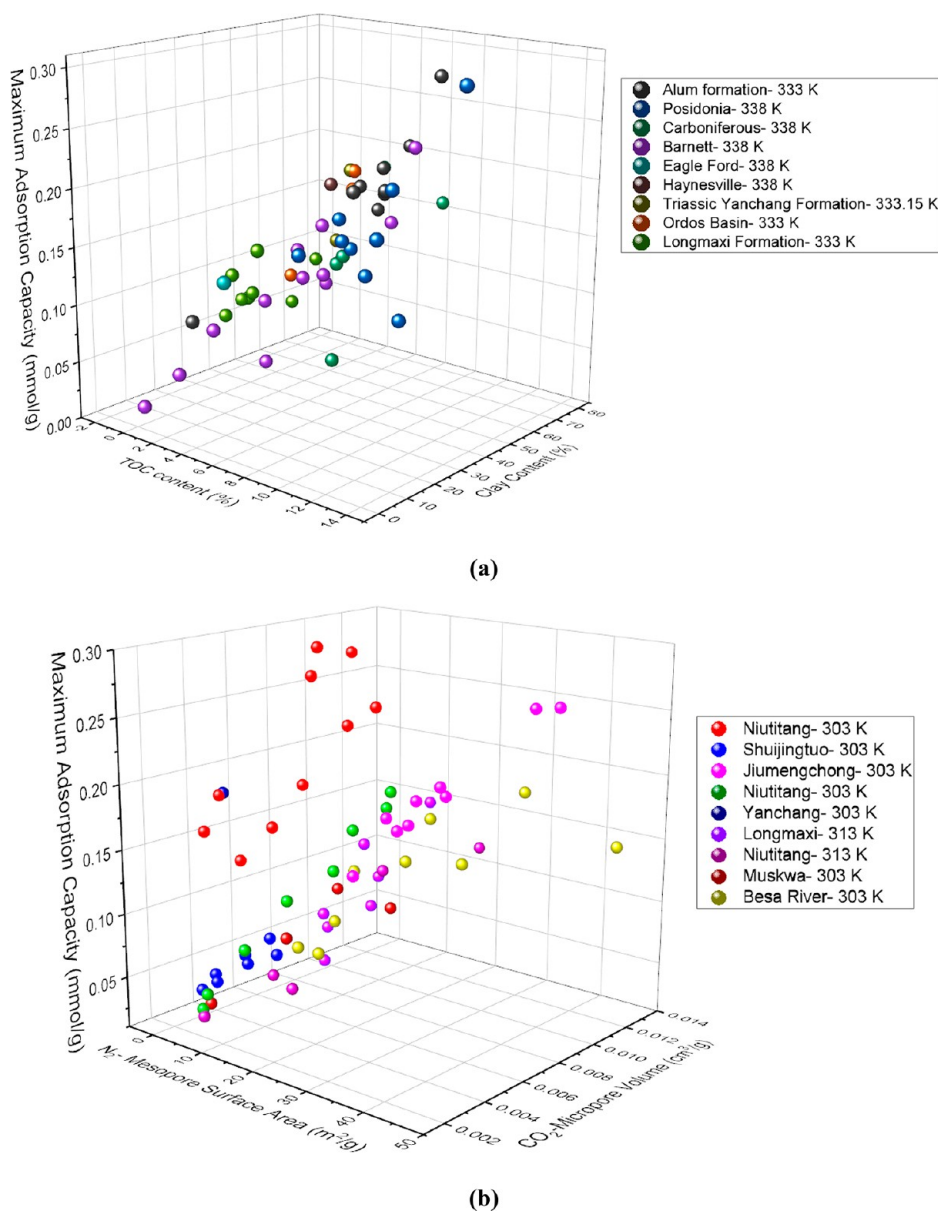


Figure 21. (a) Relationship of predicted maximum adsorption capacities obtained from the Langmuir model with TOC and clay contents in various shale samples: Alum (data from Gasparik et al.⁷²), Posidonia shale (data from Gasparik et al.⁷²), Carboniferous shale (data from Gasparik et al.⁷²), Barnett shale (data from Gasparik et al.⁷²), Eagle Ford (data from Gasparik et al.⁷²), Haynesville (data from Gasparik et al.⁷²), Triassic Yanchang Formation (data from Huang et al.³¹¹), Ordos Basin (data from Ji et al.³¹²), and Longmaxi Formation (data from Ji et al.³¹³). (b) Relationship of predicted maximum adsorption capacities obtained from the Langmuir model with mesopore surface area and micropore volume from N₂ and CO₂ adsorption, respectively, in various shale samples: Niutitang (data from Feng et al.³¹⁴), Shuijingtuo, Jiumengchong, and Niutitang (data from Gai et al.³¹⁵), Yanchang (data from Cao et al.³¹⁶), Longmaxi and Niutitang (data from Wang et al.¹⁸¹), and Muskwa and Besa River (data from Ross and Bustin²³).

using V_a and eq 23, Rexer et al.⁹⁶ used the CO₂ adsorption volume which is measured at 195 K and 1 bar as V_a . Zhang et al.⁹³ calculated V_a from the derivative of m_{ex} with respect to ρ_b , assuming that the adsorbed phase saturates and m_{abs} becomes constant at high pressures. However, molecular simulations have shown that m_{abs} monotonically increases with pressure.^{99,279} Another method to account for V_a is to relate the surface area and the width of adsorption layer.^{88,99,108} In such a method, the adsorbed layer width is fixed as 0.38 nm, which is the LJ diameter of methane molecule.³³² Tian et al.⁹⁹ compared such a direct conversion method with molecular simulation and found that the application of using V_a with eq 23 performs better than that using ρ_a with eq 24. As for the conversion method using eq 24,

several methods are applied to approximate ρ_a : (a) the constant density (424 kg/m³) of liquid methane at its boiling point (112 K and 1 bar),^{87,94} (b) the constant density (373 kg/m³) from the van der Waals constant b of saturated methane at its critical point (190.56 K and 45.8 bar),^{95,164} (c) the slope method which uses a linear regression of m_{ex} with respect to ρ_b , with the intercept of x -axis representing the maximum ρ_a ,^{87,333–335} and (d) the pressure-dependent adsorbed phase density from molecular simulation results.^{102,112,113} Do and Do³³⁶ stated that the density of supercritical fluid in the adsorbed phase can be close to, but would not exceed, its liquid density at higher pressures by studying adsorbates such as krypton, argon, nitrogen, and methane on carbonaceous solids. Wu et al.¹¹² applied the liquid

Table 4. Measured Excess Adsorption Amount in Isolated Kerogen and Pure Minerals (Including Organic-Matter-Free Clay-Mineral-Dominated Rocks)

| Sample | Temperature (K) | Pressure range (bar) | Maximum excess adsorption amount ^a (mmol/g) | Corresponding pressure at maxima (bar) | Specific surface area ^b (m ² /g) | Maximum excess adsorption amount ^c (mmol/m ²) | Source |
|---|-----------------|----------------------|--|--|--|--|-----------------------------|
| Lower Toarcian Posidonia isolated kerogen (Type II) | 338.15 | 1.8–41.9 | 0.76 | 141.9 | 68.1 | 0.01116 | Rexer et al. ⁹⁶ |
| Lower Silurian Longmaxi Formation isolated kerogen | 333 | 10–200 | 1.83 | 80 | 284.6 | 0.00643 | Xiong et al. ¹⁷⁴ |
| Vaca Muerta Formation isolated kerogen | 333 | 0–150 | 0.51 | 100 | 29.7 | 0.01717 | Wu et al. ¹¹² |
| Barnett shale isolated kerogen (Type II) | 338 | 1–130.9 | 1 | 130.9 | – | – | Hu ¹⁵⁷ |
| Upper Ordovician isolated kerogen (Type I) | 333 | 0–600 | 0.492 | 120 | – | – | Li et al. ³¹⁷ |
| Kimmeridge kerogen | 338.15 | 0–35 | 0.25 | 35 | 6.6 | 0.03788 | Zhao et al. ²⁸⁸ |
| Green River Formation shale isolated kerogen (Type I) | 338.55 | 6.1–142.6 | 0.489 | 142.6 | – | – | Zhang et al. ⁷⁰ |
| Woodford shale isolated kerogen (Type II) | 338.55 | 7.9–140.6 | 0.667 | 140.6 | – | – | Zhang et al. ⁷⁰ |
| Illite | 338.55 | 5.2–125.9 | 0.045 | 96.9 | 7.1 | 0.00634 | Ji et al. ²⁹ |
| Kaolinite | 338.55 | 6.4–112 | 0.063 | 112 | 15.3 | 0.00412 | Ji et al. ²⁹ |
| Chlorite | 338.55 | 6–115.1 | 0.056 | 115.1 | 11.7 | 0.00479 | Ji et al. ²⁹ |
| Illite–semectite | 338.55 | 2.2–98.8 | 0.111 | 98.8 | 30.8 | 0.00360 | Ji et al. ²⁹ |
| Montmorillonite | 338.55 | 5.8–108.3 | 0.263 | 108.3 | 76.4 | 0.00344 | Ji et al. ²⁹ |
| Illite | 333 | 0–200 | 0.128 | 200 | – | – | Fan et al. ³¹⁸ |
| Illite–semectite | 333 | 0–200 | 0.11 | 150 | – | – | Fan et al. ³¹⁸ |
| Montmorillonite | 333 | 0–200 | 0.138 | 150 | – | – | Fan et al. ³¹⁸ |
| Chlorite | 333 | 0–200 | 0.034 | 150 | – | – | Fan et al. ³¹⁸ |
| Kaolinite | 333 | 0–200 | 0.11 | 150 | – | – | Fan et al. ³¹⁸ |
| Illite | 333 | 3.5–180 | 0.084 | 180 | 11.2 | 0.00750 | Liu et al. ³¹⁹ |
| Kaolinite | 333 | 0–180 | 0.137 | 180 | 15.7 | 0.00873 | Liu et al. ³¹⁹ |
| Montmorillonite | 333 | 10–180 | 0.21 | 180 | 56.5 | 0.00372 | Liu et al. ³¹⁹ |

^aCollected maximum excess adsorption data from experimental measurements. ^bSSA is measured based on N₂ BET data. ^cAdsorption amount per surface area (mmol/m²) = adsorption amount per unit weight (mmol/g)/SSA (m²/g).

Table 5. Simulated Excess and Absolute Adsorption Amount in Different Types of Pores from Molecular Simulations

| Adsorbent | Temperature (K) | Adsorption type | Pressure range (bar) | Range of maximum adsorption amount (mmol/m ²) | Pressure range of maximum adsorption amount (bar) | Source |
|----------------------------------|-----------------|---------------------|----------------------|---|---|------------------------------|
| Carbon slit pore (0.7–10 nm) | 333.15 | Excess adsorption | 50–500 | 0.0036–0.006 | 50–150 | Pang and Jin ¹⁰⁰ |
| | | Absolute adsorption | 50–500 | 0.0044–0.0082 | 500 | |
| Illite slit pore (1–8 nm) | 333.15 | Excess adsorption | 0–500 | 0.0019–0.0023 | 100–150 | Tian et al. ⁹⁹ |
| Illite slit pore 4 nm | 333.15 | Absolute adsorption | 0–500 | 0.0064 | 500 | |
| Kerogen slit pore (2 and 4 nm) | 338.15 | Excess adsorption | 100–600 | 0.0052–0.0058 | 100 | Zhou et al. ²⁸ |
| Montmorillonite slit pore (2 nm) | 333 | Excess adsorption | 25–400 | 0.0037 | 180 | Xiong et al. ¹⁷⁴ |
| | | Absolute adsorption | 25–400 | 0.00704 | 400 | |
| Carbon slit pore (0.4–9 nm) | 298 | Excess adsorption | 0–180 | 0.00767–0.01536 | 29–132.7 | Mosher et al. ¹¹⁶ |

density to directly convert experimental measured m_{ex} to m_{abs} and observed an obvious declining trend of m_{abs} versus pressure

at high pressures for methane adsorption in shale samples from the Vaca Muerta Formation, while the absolute adsorption

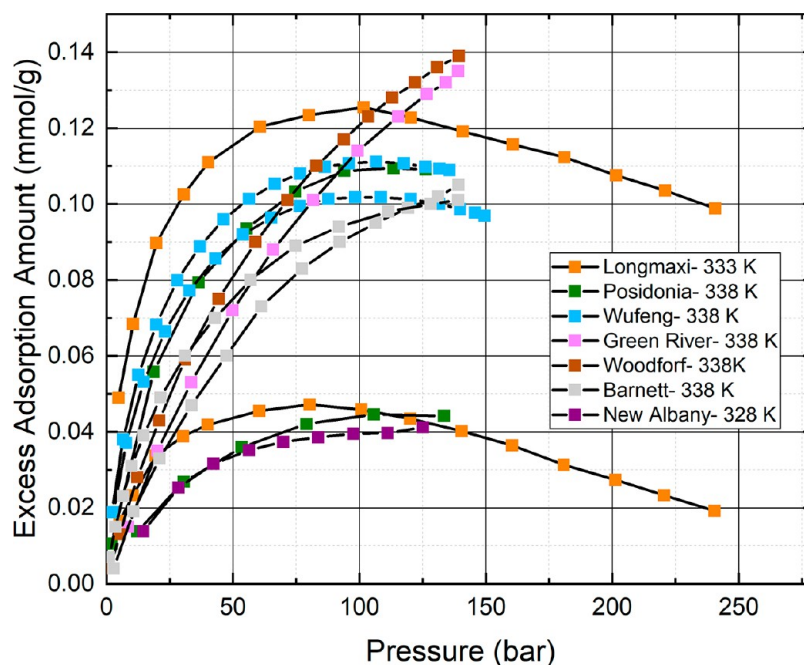


Figure 22. Methane excess adsorption isotherms in different shale samples: Longmaxi (data from Zhou et al.⁸⁷), Posidonia (data from Rexer et al.⁹⁶), Wufeng (data from Tian et al.⁹⁵), Green River (data from Zhang et al.⁷⁰), Woodford (data from Zhang et al.⁷⁰), Barnett (data from Zhang et al.⁷⁰), and New Albany (data from Chareonsuppanimit et al.²⁸⁹).

converted by applying the GCMC adsorbed phase density is larger than that obtained by using liquid density. Yu et al.¹⁰¹ used pressure-dependent density from correlations proposed by Riewchotisakul and Akkutlu³³⁷ according to molecular dynamics simulation at 353 K in 5 nm carbon nanotube. Pang et al.⁸⁸ assessed the performance of using constant ρ_a for conversion and found a similar behavior by using GCMC simulations to study methane adsorption in kerogen nanoporous media. Moreover, Zhou et al.⁸⁷ reported that the regressed ρ_a from the slope method ranges from 219 to 527 kg/m³, while they attributed this behavior to the different pore structures of shale rock samples. Clarkson and Haghshenas³³³ found that the regressed ρ_a can be as high as 1050 kg/m³ for methane adsorption in shale samples from the Rio Bonito Formation.

In addition, a large number of works used thermodynamic models such as Langmuir, supercritical Dubinin–Radushkevich (SDR), and supercritical-BET (SBET) to regress the experimentally measured m_{ex} to predict m_{abs} . In the following subsections, we discuss these popular models.

5.3.1. Langmuir Model. The Langmuir model is one of the most widely applied adsorption models in the shale industry to describe methane adsorption behavior thanks to its simplicity.^{101,108,294,338} The Langmuir model describes the kinetic balance of gas adsorption and desorption on a flat energetically homogeneous surface³³⁹ as shown in Figure 23.³⁴⁰

The assumptions used in the Langmuir model include: (a) Monolayer adsorption forms on a flat energetically homogeneous surface. (b) The surface contains the adsorption sites with equal adsorption energy. (c) Fluid–fluid interactions are not considered between adjacent gas molecules^{341–343} (thus, an ideal gas assumption). Here, we show the derivation of the Langmuir model from the kinetic approach³⁴³ for simplicity, while other approaches such as classical thermodynamic^{213,344} and statistical mechanics^{343,345} can be found elsewhere. In the Langmuir model, the reversible process of adsorption and desorption can be described as

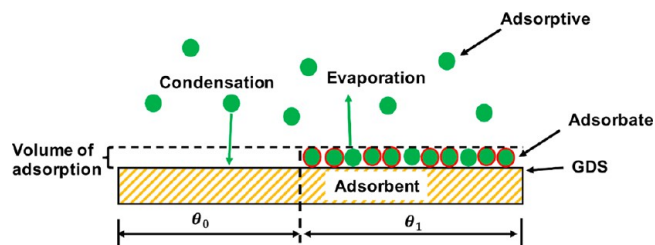


Figure 23. Schematic representation of Langmuir monolayer adsorption model. The green circles represent gas molecules. GDS is the Gibbs dividing surface. θ_0 and θ_1 represent the coverage of the surface site that is empty and occupied by adsorbate, respectively. The interpretation of excess and absolute adsorptions can be referred to Figure 12. Reproduced from Xiong et al.³⁴⁰ with permission. Copyright (2020) Elsevier.



where A_g , S , and A_a are free gas molecule, empty adsorption site, and site occupied by the adsorbed molecule, respectively; k_a and k_d represent rate constants in adsorption and desorption process, respectively. The rate of adsorption (r_a) and desorption (r_d) can be given as

$$\begin{cases} r_a = Pk_a\theta_1 \\ r_d = k_d\theta_1 \end{cases} \quad (33)$$

where P and θ_1 are pressure and coverage of adsorbate on the solid surface, respectively. Within the framework of the Langmuir model, the fraction of the surface covered by adsorbed gas is calculated according to the adsorbed amount (m_{abs}^{LA}) and maximum adsorption capacity (m_{max}^{LA}): $\theta_1 = m_{abs}^{LA}/m_{max}^{LA}$. When the system is at equilibrium, the rate of adsorption equals to that in desorption ($r_a = r_d$). By defining the Langmuir equilibrium

constant $K_L = k_a/k_d$ and substituting θ_1 into eq 33, the general expression of the Langmuir model is given as

$$m_{\text{abs}}^{\text{LA}} = m_{\text{max}}^{\text{LA}} \frac{K_L P}{1 + K_L P} \quad (34)$$

It should be noted that the Langmuir model describes the true adsorption amount (absolute adsorption), while the excess adsorption amount is given as

$$m_{\text{ex}}^{\text{LA}} = m_{\text{max}}^{\text{LA}} \frac{K_L P}{1 + K_L P} \left(1 - \frac{\rho_b}{\rho_a}\right) \quad (35)$$

or

$$m_{\text{ex}}^{\text{LA}} = m_{\text{max}}^{\text{LA}} \frac{K_L P}{1 + K_L P} - V_a \rho_b \quad (36)$$

where ρ_a and V_a are adsorbed phase density and adsorbed phase volume applied in Langmuir model, respectively. Unlike the above-mentioned direct conversion methods, the Langmuir model is used to regress the experimentally measured m_{ex} to obtain m_{abs} . There are generally two types of applications with different assumptions used in current works:^{80,125} (a) constant ρ_a (as in eq 35); (b) constant V_a (as in eq 36).

In terms of the applications with constant ρ_a and eq 35, V_a increases with pressure, while ρ_a can be assumed as a predetermined (fixed) value of 373 or 424 kg/m³^{395,164} or one of the regression parameters.^{87,94,108} Tian et al.⁹⁵ applied a constant density of 373 and 424 kg/m³ and freely fitted ρ_a in the Langmuir model to interpret the experimentally measured methane m_{ex} in Lower Silurian–Upper Ordovician shale samples. These approaches show a similar regression quality in terms of m_{ex} . They also found that the freely fitted ρ_a is temperature dependent, while it can be higher than the liquid methane density. Similarly, Gasparik et al.⁹⁴ observed similar regression performances for predetermined and freely fitted ρ_a in almost all the studied samples. They stated that the high value of freely fitted ρ_a (over 600 kg/m³) in Posidonia samples may be due to the artifacts during regression. The ρ_a increases with pressure from molecular simulations,^{99,112,279} indicating that using a constant ρ_a may not be justifiable. Zhang et al.⁹³ applied a pressure-dependent ρ_a associated with the Langmuir model. The maximum density in their expression is obtained from the intercept of the x -axis of excess adsorption with respect to bulk density. On the other hand, the regressed maximum adsorption capacity has been used to evaluate the effect of shale rock properties such as composition (e.g., TOC, moisture)^{70,346,347} and pore structures.^{23,348,349} In terms of the approaches using constant V_a , Xiong et al.¹⁰⁸ used V_a obtained by multiplying SSA by 0.38 nm (as the width of methane single-adsorption layer) to regress experimentally measured m_{ex} . Pang et al.⁸⁸ showed that the Langmuir model with 0.38 nm as the constant adsorption layer width can have a reasonable agreement with GCMC simulations. In addition to the traditional Langmuir model, the Toth model with the consideration of heterogeneity^{125,350} has been applied

$$\begin{cases} m_{\text{abs}}^{\text{Toth}} = m_{\text{m}}^{\text{Toth}} \frac{K_T P}{(1 + (K_T P)^n)^{1/n}} \\ m_{\text{ex}}^{\text{Toth}} = m_{\text{m}}^{\text{Toth}} \frac{K_T P}{(1 + (K_T P)^n)^{1/n}} - V_a \rho_b \text{ or} \\ m_{\text{m}}^{\text{Toth}} \frac{K_T P}{(1 + (K_T P)^n)^{1/n}} (1 - \rho_b / \rho_a) \end{cases} \quad (37)$$

where K_T is a constant, and n reflects the heterogeneity of adsorbent. If n is close to 1, the Toth model regresses to the Langmuir model.

Due to the rock heterogeneity, the energetically homogeneous assumption used in the Langmuir model may not be applicable to shale nanoporous media. To take into account the different rocks in shale, Tang et al.^{280,351} used a dual-site Langmuir (DSL) model by assuming two types of adsorption sites with different temperature-dependent equilibrium constants. A fraction coefficient is used to account for the ratio of these sites. The added parameters lead to an increase in degrees of freedom for fitting, while the fraction coefficient obtained from regression only represent the results of the best numerical fit, not based on the physical meaning of shale rock heterogeneity. Li et al.⁸⁰ proposed a modified Langmuir model to account for the energetic heterogeneity by considering PSD. The adsorption energy is expressed by using the Steele 10-4 potential model³⁵² so that adsorption energy distributions are related to the actual shale PSD. In their approach, the averaged interaction coefficient which is dependent on the density of adsorbent atoms and adsorbate–adsorbent interaction is applied, while in shale nanoporous media the rock heterogeneity may result in different PSDs and interaction energies.

We note that the original Langmuir model is developed for adsorption on a single surface, not in a porous media. As we have discussed, shale has a wide range of PSD with an extensive number of micropores and mesopores. The methane adsorption behaviors in micropores and some small mesopores are drastically different from the adsorption on a single surface making using the Langmuir model to convert m_{ex} to obtain m_{abs} a pure curve fitting.³⁰ In addition, there are many works directly using the Langmuir adsorption amount to represent the excess adsorption.^{35,157,353} Although the pressures in their work are generally low, the mixed definitions of excess and absolute adsorptions may lead to larger errors if the isotherm is extrapolated to higher pressure conditions.

5.3.2. Supercritical Dubinin–Radushkevich (SDR) Model. The classical Dubinin–Radushkevich (DR) model describes a micropore-filling phenomenon which is based on Polanyi potential theory.^{354,355} It has been widely used to model subcritical gas adsorption in zeolite and carbonaceous materials.^{356,357} Within the framework of the DR model, the adsorption potential A is temperature dependent, given as

$$A = -RT \ln \left(\frac{P}{P_0} \right) \quad (38)$$

where P and P_0 are pressure and saturation pressure, respectively. The characteristic curve is investigated in terms of the distribution of the adsorption volume and potential, which reflects the given adsorbent–adsorbate system.³⁵⁴ Therefore, the fraction (using Gaussian distribution) of pore volume occupied by the adsorbed phase (W) to the total pore volume (W_0) can be given as

$$\frac{W}{W_0} = \exp[-(A/E)^2] \quad (39)$$

where E is the characteristic energy of the system. By defining $E = \beta E_0$, where β and E_0 are affinity coefficient and characteristic energy of a standard adsorbate–adsorbent system, and applying W/W_0 , the absolute adsorption in the DR model can be expressed as

$$\begin{aligned} m_{\text{abs}}^{\text{DR}} &= m_{\text{max}}^{\text{DR}} \exp\left\{-\left[\frac{RT}{\beta E_0} \ln\left(\frac{P}{P_0}\right)\right]^2\right\} \\ &= m_{\text{max}}^{\text{DR}} \exp\left\{-D \left[\ln\left(\frac{P}{P_0}\right) RT\right]^2\right\} \end{aligned} \quad (40)$$

where D is defined as the constant representing the affinity of adsorbate to the adsorbent, which depends on the structural property of porous media. It should be noted the DR model is originally used for subcritical adsorption. Sakurovs et al.⁹⁸ modified the original DR model to the application of supercritical gas adsorption in coal. The modified version is called supercritical DR (SDR) model which utilizes adsorbed phase density (ρ_a^{SDR}) and bulk density (ρ_b), which is given as

$$m_{\text{abs}}^{\text{SDR}} = m_{\text{max}}^{\text{SDR}} \exp\left\{-D \left[\ln\left(\frac{\rho_a}{\rho_b}\right) RT\right]^2\right\} \quad (41)$$

Then, the excess adsorption in SDR model is given as

$$m_{\text{ex}}^{\text{SDR}} = m_{\text{max}}^{\text{SDR}} \exp\left\{-D \left[\ln\left(\frac{\rho_a}{\rho_b}\right) RT\right]^2\right\} \left(1 - \frac{\rho_b}{\rho_a}\right) \quad (42)$$

or

$$m_{\text{ex}}^{\text{SDR}} = m_{\text{max}}^{\text{SDR}} \exp\left\{-D \left[\ln\left(\frac{\rho_a}{\rho_b}\right) RT\right]^2\right\} - V_a \rho_b \quad \text{with } V_a = \frac{m_{\text{max}}^{\text{SDR}}}{\rho_a} \quad (43)$$

The SDR model has been used to regress methane m_{ex} to obtain m_{abs} in coal and shale samples.^{57,95,317,358} Both constant adsorbed phase density (eq 42) and constant adsorbed phase volume (eq 43) methods have been applied in experimental and simulation works. In terms of the constant adsorbed phase density method, the fitting parameters include $m_{\text{max}}^{\text{SDR}}$ and D , while the adsorbed phase density can be treated as a freely fitted^{95,98,317,340} or predetermined value such as 373 or 424 kg/m³.^{88,347} Li et al.³¹⁷ applied the SDR and Langmuir models using fixed adsorbed phase density to regress the experimentally measured methane m_{ex} in shale and isolated kerogen samples from Sichuan Basin under three temperatures (333, 373, and 413 K) and pressure up to 600 bar. They found that the fitted adsorbed phase density for shale is in the range of 210–546 and 209–489 kg/m³ for the Langmuir and SDR models, respectively. Tian et al.⁹⁵ reported that the freely fitted adsorbed phase densities in the SDR model for shale samples from Sichuan Basin at 308.5, 323.5, and 338.5 K are all lower than 424 kg/m³, while the highest regressed adsorbed phase density value based on the Langmuir model can be even over 1000 kg/m³. On the other hand, Hu et al.³⁴⁷ investigated the methane adsorption in overmature Wufeng–Longmaxi shale and found that the regressed ρ_a can be higher than 424 kg/m³. In addition, they found

that the regressed maximum adsorption capacity in the SDR model is independent of the applied ρ_a approaches (either freely fitted or predetermined ρ_a as 424 or 373 kg/m³), while the maximum adsorption capacity in SDR is comparable to that in the Langmuir model using a freely fitted adsorbed phase density. In contrast, Wang et al.³⁵⁹ compared the maximum adsorption capacity of shale samples from the Wufeng–Longmaxi Formation calculated with a fixed adsorbed phase density as 424 or 373 kg/m³ and a freely fitted adsorbed phase density. They found a smaller regressed maximum adsorption capacity when using a higher fixed adsorbed phase density. Rexer et al.⁵⁷ applied the SDR model to methane adsorption in an Alum shale sample at temperatures from 300 to 430 K and pressures up to 140 bar and with a predetermined density as 370 kg/m³, which is obtained from molecular simulations by Ambrose et al.³⁶⁰ They found that the use of 370 kg/m³ can have a good regression result only for temperatures between 300 and 338 K, while the freely fitted adsorbed phase density method can have good regression results at all the temperature conditions. On the other hand, in terms of the constant adsorbed phase volume method, different approaches have been used. Pang et al.⁸⁸ used 0.38 nm as the adsorption layer width associated with surface area to account for the constant adsorbed phase volume, and the calculated absolute adsorption is in a good agreement with molecular simulations. Tian et al.⁹⁹ used the constant adsorbed phase volume in the SDR model to fit methane excess adsorption in illite nanopores obtained from GCMC simulations. They found that using a constant adsorbed phase volume in the SDR model has a better performance than that using a constant adsorbed phase density in terms of absolute adsorption prediction by comparing to GCMC simulations.

However, we note that the SDR model is based on the pore filling mechanism, which has been regarded as the adsorption mechanism in micropores, while shale has a wide range PSD covering micropores, mesopores, and macropores. In addition, the current SDR model cannot take into account the rock heterogeneity.

5.3.3. Supercritical Brunauer–Emmett–Teller (SBET) Model. As methane adsorption in shale nanoporous media may not be fully described by the monolayer adsorption model, and multilayer models have been suggested by molecular simulation works,^{99,279} the BET model has also been proposed to convert m_{ex} to m_{abs} . As shown in Section 3.2.1, the conventional BET equation assumes an infinite number of adsorption layers on adsorbent (thus a multilayer adsorption model), while the general equation to describe the BET isotherm in terms of n adsorption layers can be given as

$$m_{\text{abs}}^{\text{BET}} = \frac{m_{\text{max}}^{\text{BET}} k_0 P/P_0 \left[1 - (n+1)(P/P_0)^n + n(P/P_0)^{n+1}\right]}{1 - P/P_0 \left[1 + (k_0 - 1)P/P_0 - k_0(P/P_0)^{n+1}\right]} \quad (44)$$

where $m_{\text{abs}}^{\text{BET}}$ and $m_{\text{max}}^{\text{BET}}$ are adsorbed gas amount and maximum adsorption capacity in BET model, respectively; k_0 reflects the energetic of adsorption in the system which is introduced in Section 3.2.1, and P and P_0 are the bulk pressure and saturation pressure of gas molecules, respectively. The BET model is originally developed to interpret gas adsorption at subcritical conditions, while methane adsorption in shale nanoporous media is generally conducted at supercritical conditions.³⁶¹ Yu et al.¹⁰² used the pseudosaturation pressure (P_s)³⁶² to replace the saturation pressure, which is given by the Antoine equation³⁶³

$$\ln P_g = 7.7437 - \frac{1306.5485}{19.4362 + T} \quad (45)$$

Then, the excess adsorption in supercritical BET model is given as

$$m_{\text{ex}}^{\text{SBET}} = \frac{m_{\text{max}}^{\text{SBET}} k_0 P/P_0 \left[\frac{1 - (n+1)(P/P_0)^n + n(P/P_0)^{n+1}}{1 + (k_0 - 1)P/P_0 - k_0(P/P_0)^{n+1}} \right] \left(1 - \frac{\rho_b}{\rho_a^{\text{SBET}}} \right)}{1 - P/P_0} \quad (46)$$

where ρ_a^{SBET} is assumed to be pressure dependent³⁶⁴ as $\rho_a^{\text{SBET}} = 0.1057 \ln(P) - 0.4629$. Therefore, the fitting parameters in their work include $m_{\text{max}}^{\text{SBET}}$, n , and k_0 . We note that while the BET model can describe multilayer adsorption, the conversion shown in eq 46 is still based on a single-layer adsorption model as depicted in eq 24. On the other hand, Zhou et al.¹⁰³ proposed a SBET model in terms of bulk density and adsorbed phase density, given as

$$m_{\text{abs}}^{\text{SBET}} = \frac{m_{\text{max}}^{\text{SBET}} k_0 \rho_b / \rho_a^{\text{SBET}} \left[\frac{1 - (n+1)(\rho_b / \rho_a^{\text{SBET}})^n + n(\rho_b / \rho_a^{\text{SBET}})^{n+1}}{1 + (k_0 - 1)\rho_b / \rho_a^{\text{SBET}} - k_0(\rho_b / \rho_a^{\text{SBET}})^{n+1}} \right] \left(1 - \frac{\rho_b}{\rho_a^{\text{SBET}}} \right)}{1 - \rho_b / \rho_a^{\text{SBET}}} \quad (47)$$

Then, the excess adsorption is given as

$$m_{\text{ex}}^{\text{SBET}} = \frac{m_{\text{max}}^{\text{SBET}} k_0 \rho_b / \rho_a^{\text{SBET}} \left[\frac{1 - (n+1)(\rho_b / \rho_a^{\text{SBET}})^n + n(\rho_b / \rho_a^{\text{SBET}})^{n+1}}{1 + (k_0 - 1)\rho_b / \rho_a^{\text{SBET}} - k_0(\rho_b / \rho_a^{\text{SBET}})^{n+1}} \right] \left(1 - \frac{\rho_b}{\rho_a^{\text{SBET}}} \right)}{1 - \rho_b / \rho_a^{\text{SBET}}} \quad (48)$$

In their work, the fitting parameters include $m_{\text{max}}^{\text{SBET}}$, n , ρ_a^{SBET} , and k_0 , while the conversion is conducted under single-layer adsorption model. Xiong et al.³⁴⁰ compared the performance of different adsorption models. They found that the absolute adsorption obtained from SBET keeps increasing and is significantly higher than that predicted by the Langmuir model. Moreover, the SBET-based model with a constant adsorbed density is found to present negative adsorption at high pressures.

While the original BET model can describe multilayer adsorption structures, the current SBET models still convert m_{ex} to m_{abs} based on single-layer adsorption model (see eqs 46 and 48). Similar to the Langmuir model, the SBET model is built upon adsorption on a single energetically homogeneous surface which cannot fully capture the rock heterogeneity and pore size heterogeneity in shale.

5.3.4. Ono–Kondo (OK) Lattice Model. While the Langmuir and SDR models cannot describe the multilayer adsorption models and SBET remains as a pseudo-multilayer model, the Ono–Kondo (OK) lattice model³⁶⁵ can explicitly consider fluid–fluid and fluid–surface interactions as well as the layering structures in porous media.^{366–369} The schematic representation of the OK model is shown in Figure 24 in a cubic lattice geometry. In OK lattice theory, the assumptions include the following: (a) Each adsorption site can be occupied by one adsorbate molecule or at vacancy, and each layer is parallel to the pore surface. (b) Fluid–fluid interactions between adsorbate molecules in the same layer and adjacent layers are considered. (c) Fluid–surface interactions are considered only at the first adsorption layer. At equilibrium, the change of Gibbs free energy relates to the exchange of an adsorbate molecule at one site to

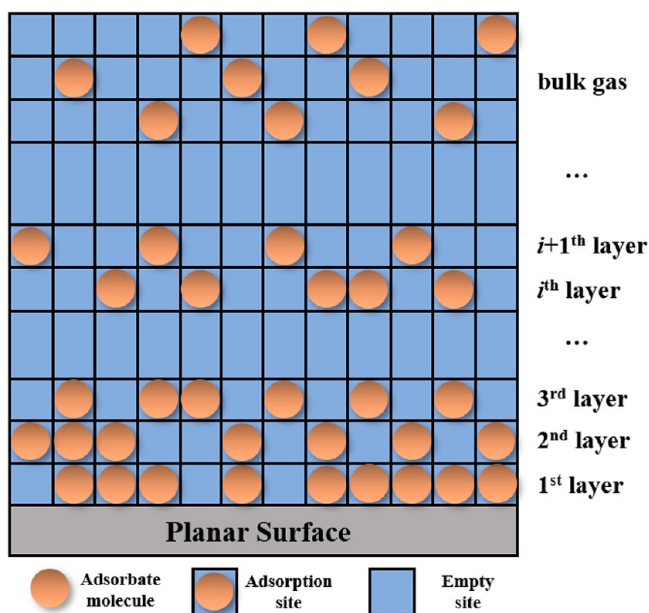


Figure 24. Schematic representation of Ono–Kondo lattice model. i is the index of lattice layers.

the empty site of infinite distance zero; the expressions can be given by the mean-field approximation

$$\begin{cases} \ln \left[\frac{x_i(1-x_b)}{x_b(1-x_i)} \right] + (z_1 x_{i+1} + z_2 x_i + z_1 x_{i-1} - z_0 x_b) \frac{\varepsilon}{k_B T} = 0, & i \geq 2 \\ \ln \left[\frac{x_1(1-x_b)}{x_b(1-x_1)} \right] + (z_1 x_2 + z_2 x_1 - z_0 x_b) \frac{\varepsilon}{k_B T} + \frac{\varepsilon_s}{k_B T} = 0, & i = 1 \end{cases} \quad (49)$$

where i is the index of lattice layer; ε and ε_s are adsorbate–adsorbate interaction energy and adsorbate–adsorbent interaction energy, respectively; z_0 and z_2 are bulk coordination number and coordination number within the same layer, respectively, and z_1 can be expressed as $z_1 = (z_0 - z_2)/2$. For a cubic lattice configuration, $z_0 = 6$, $z_1 = 1$, and $z_2 = 4$,³⁶⁸ while for hexagonal lattice configuration, $z_0 = 8$, $z_1 = 1$, and $z_2 = 6$,³⁷⁰ x_i and x_b represent the fraction of adsorbed phase molecules occupy the layer i and the fraction of molecules in the bulk phase with respect to lattice site, respectively. The expressions of x_i and x_b can be given as

$$\begin{cases} x_i = \frac{\rho_{a,i}^{\text{OK}}}{\rho_{\text{am}}^{\text{OK}}} \\ x_b = \frac{\rho_b}{\rho_{\text{am}}^{\text{OK}}} \end{cases} \quad (50)$$

where $\rho_{a,i}^{\text{OK}}$ and $\rho_{\text{am}}^{\text{OK}}$ are adsorbed phase density in layer i and maximum adsorbate density in each layer, respectively. Therefore, the total excess adsorption and absolute adsorption in OK model can be given as

$$\begin{cases} m_{\text{ex}}^{\text{OK}} = C \sum_{i=1}^{n_k} (x_i - x_b) \\ m_{\text{abs}}^{\text{OK}} = C \sum_{i=1}^{n_k} x_i \end{cases} \quad (51)$$

where C represents the adsorption capacity and reflects both adsorbed phase density and structural properties in each layer.

Sudibandriyo et al.¹⁰⁷ applied monolayer and three-layer adsorption in the OK model for CH_4 , N_2 , and CO_2 adsorption in coal samples. The two-parameter OK model (C and ϵ_s) was proposed in their work, with $\rho_{\text{am}}^{\text{OK}}$ and ϵ obtained from the reciprocal van der Waals co-volume and energy parameter of the LJ 12-6 potential. Mery and Sinayuc¹⁰² adopt Sudibandriyo et al.'s¹⁰⁷ model with monolayer adsorption assumption to predict CO_2 sequestration in shale. However, in the works by Bi et al.^{371,372} and Qin et al.³⁷³ which assumes $\epsilon = 0$ and monolayer adsorption, the OK model regresses to the Langmuir model. They also mistakenly used the expression of excess adsorption for absolute adsorption, which would lead to large errors. Pang and Jin²⁷⁹ assumed a constant adsorbed phase volume which utilizes $C = m_{\text{max}}^{\text{OK}} W_a^{\text{OK}}$ according to the findings from the GCMC simulation to describe methane adsorption in carbon slit pores at 333.15 K, with $m_{\text{max}}^{\text{OK}}$ and W_a^{OK} representing the maximum adsorption capacity per unit surface area and adsorption layer width in the OK model, respectively. W_a^{OK} is fixed as 0.38 nm, which is consistent with the methane LJ diameter.⁹⁹ The regression parameters in their work include $m_{\text{max}}^{\text{OK}}$, $\rho_{\text{am}}^{\text{OK}}$, ϵ , and ϵ_s , while a three-layered structure is assumed from each pore surface. The result of the proposed OK model has shown an excellent agreement with GCMC simulations in terms of both m_{ex} and converted m_{abs} . In addition, the contribution of the second adsorption layer can be explicitly characterized. Xiong et al.¹⁰⁸ used a constant adsorption layer width associated with SSA obtained from experiments to regress experimentally measured methane excess adsorption in shale samples from the Lower Permian Shanxi Formation and a Lower Jurassic sample from the Posidonia shale. They found that the regressed OK model shows monolayer adsorption behaviors, while the regressed maximum adsorbed density should be less than the theoretical limit of methane density (560 kg/m^3) by assuming a hexagonal closed packing (HCP). Moreover, Pang et al.¹⁰⁰ built a model kerogen nanoporous media with a realistic continuous PSD. The methane adsorption is characterized into six distinct types based on the density profiles obtained from the GCMC simulation. In order to consider different adsorption behaviors in micropores and mesopores, pores with specific pore size ranges are characterized and lumped into adsorption type. The performance of the OK model with PSD lumping (OK-PSD-L) is validated by randomly generating 1250 samples with continuous PSD from 0.7 to 50 nm and micropore volume ratios from 5% to 35%. The OK-PSD-L model has a more superior performance to predict the first layer absolute adsorption than Langmuir, SDR, and SBET methods. However, only pore size heterogeneity is considered in current works,^{88,100,122} while the rock heterogeneity arising from different adsorption capacities in organic and inorganic matters has not been fully taken into account.

5.3.5. Simplified Local Density (SLD) Model. The simplified local density (SLD) model is based on the local density approximation (LCA) to calculate the configurational energy of adsorbates according to fluid–surface interaction and EOS.³⁷⁴ The SLD model which considers both fluid–fluid interactions and fluid–surface interactions has been widely used in interpreting hydrocarbon adsorption in shale and coal.^{289,375–379} The currently used SLD model often describes adsorbates in slit pores as shown in Figure 25.

Three basic assumptions are made in the SLD model:^{104,225,375} (a) The adsorbate in the pore has the same chemical potential as its bulk value. (b) At equilibrium, the

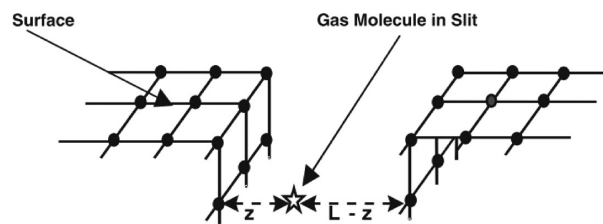


Figure 25. Schematic representation of simplified local density (SLD) model. Reproduced from Chareonsuppanimit et al.²⁸⁹ with permission. Copyright (2012) Elsevier.

chemical potential of the adsorbate in the pore is the summation of fluid–fluid and fluid–surface potentials. (c) The chemical potential is calculated according to the local density value (thus, a LCA). The chemical potential at position z along the pore space is given as

$$\mu(z) = \mu_{\text{ff}}(z) + \mu_{\text{fs}}(z) = \mu_{\text{bulk}} \quad (52)$$

where $\mu_{\text{ff}}(z)$, $\mu_{\text{fs}}(z)$, and $\mu_{\text{bulk}}(z)$ are chemical potential from fluid–fluid interactions, fluid–surface interactions, and bulk phase, respectively. The $\mu_{\text{ff}}(z)$ and $\mu_{\text{bulk}}(z)$ are given as

$$\begin{cases} \mu_{\text{bulk}} = \mu_0(T) + RT \ln \left(\frac{f_{\text{bulk}}}{f_0} \right) \\ \mu_{\text{ff}}(z) = \mu_0(T) + RT \ln \left(\frac{f_{\text{ff}}(z)}{f_0} \right) \end{cases} \quad (53)$$

where $\mu_0(T)$ and f_0 are chemical potential and fugacity of a reference state, respectively, R and T the gas constant and temperature, respectively, and f_{bulk} and $f_{\text{ff}}(z)$ the fugacity of bulk phase and at position z . $\mu_{\text{fs}}(z)$ can be expressed based on fluid–surface potential ($\Psi^{\text{fs}}(z)$) between two pore surfaces

$$\mu_{\text{fs}}(z) = N_A [\Psi^{\text{fs}}(z) + \Psi^{\text{fs}}(L - z)] \quad (54)$$

where N_A is the Avogadro constant, and L is the pore width. Integrated 10-4 potential³⁵² is used to account for fluid–surface potential

$$\Psi^{\text{fs}}(z) = 4\pi\rho_{\text{atom}}\epsilon_{\text{fs}}\sigma_{\text{fs}}^2 \left[\frac{\sigma_{\text{fs}}^{10}}{5(z')^{10}} - \frac{1}{2} \sum_{i=1}^4 \frac{\sigma_{\text{fs}}^4}{[z' + (i-1)\sigma_{\text{ss}}]^4} \right] \quad (55)$$

where ρ_{atom} is the density of solid atom, 38.2 atoms/nm^2 , ϵ_{fs} the interaction parameter between fluid and surface, σ_{fs} the fluid–solid atom diameter which can be given as $\sigma_{\text{fs}} = (\sigma_{\text{ff}} + \sigma_{\text{ss}})/2$, and σ_{ff} and σ_{ss} are 0.355 and 0.3758 nm, respectively, and z' the dummy coordinate which can be given as $z' = z + \sigma_{\text{ss}}/2$. Therefore, eq 52 can be given as

$$f_{\text{ff}}(z) = f_{\text{bulk}} \exp \left[- \frac{\Psi^{\text{fs}}(z) + \Psi^{\text{fs}}(L - z)}{k_B T} \right] \quad (56)$$

where k_B is the Boltzmann constant. The Peng–Robinson equation of state (PR-EOS)³⁸⁰ is used for fugacity calculation of bulk fluid and adsorbate in the system

$$\left\{ \begin{aligned} \ln \frac{f_{\text{bulk}}}{P} &= \frac{b\rho_b}{1-b\rho_b} - \frac{a(T)\rho_b}{RT(1+2b\rho_b-b^2\rho_b^2)} - \ln\left(\frac{P}{RT\rho_b} - \frac{Pb}{RT}\right) \\ &\quad - \frac{a(T)}{2\sqrt{2}bRT} \ln\left[\frac{1+(1+\sqrt{2})\rho_b b}{1+(1-\sqrt{2})\rho_b b}\right] \\ \ln \frac{f_{\text{ff}}(z)}{P} &= \frac{b\rho(z)}{1-b\rho(z)} - \frac{a_{\text{ads}}(z)\rho(z)}{RT(1+2b\rho(z)-b^2\rho^2(z))} \\ &\quad - \ln\left(\frac{P}{RT\rho(z)} - \frac{Pb}{RT}\right) - \frac{a_{\text{ads}}(z)}{2\sqrt{2}bRT} \ln\left[\frac{1+(1+\sqrt{2})\rho(z)b}{1+(1-\sqrt{2})\rho(z)b}\right] \end{aligned} \right. \quad (57)$$

where $a(T)$ and b are the parameter in terms of attraction and the van der Waals co-volume,³⁸¹ respectively, ρ_b and $\rho(z)$ the bulk density and density along z , $a_{\text{ads}}(z)$ the function of position which is proposed by Chen et al.,³⁸² and b can be corrected as³⁸³

$$b_{\text{ads}} = b(1 + \Lambda_b) \quad (58)$$

where b_{ads} and Λ_b are modified co-volume and correction parameter, respectively. Therefore, the excess adsorption in SLD model can be expressed as

$$m_{\text{ex}}^{\text{SLD}} = \frac{A}{2} \int (\rho(z) - \rho_b) dz \quad (59)$$

where A is the surface area. Therefore, the absolute adsorption can be calculated based on the characterization of adsorbed phase width (W_a) from density distribution in SLD model

$$m_{\text{abs}}^{\text{SLD}} = \frac{A}{2} \int_{W_a} \rho(z) dz \quad (60)$$

Here, $m_{\text{ex}}^{\text{SLD}}$ is used to regress experimentally measured excess adsorption, while typical regression variables include ε_{fs} and other parameters treated differently in various works. Qi et al.²²⁵ utilized four regression parameters (ε_{fs} , Λ_b , A , and L) for methane adsorption in shale, kerogen, and clay. The regressed specific surface area of montmorillonite is found to be two times that in kerogen and three times that in shale, respectively. In Liu et al.,¹⁰⁴ ε_{fs} and Λ_b are two adjustable parameters, and the adsorbed phase width is characterized as a methane diameter of 0.37 nm. Here, L is chosen as the dominant pore size from the PSD obtained by NLDFT, and A is from BET SSA. Several works^{104,375} used $\sigma_{\text{ff}}/2$ and $L - \sigma_{\text{ff}}/2$ as the upper and lower limits for density integration, respectively, while other works^{106,225,384} stated that the application of $3\sigma_{\text{ff}}/8$ and $L - 3\sigma_{\text{ff}}/8$ can avoid computational issues during regression. Wu et al.³⁸⁵ derived a SLD-cylinder model for CH_4 and H_2 adsorption in multiwalled carbon nanotubes (MWCNTs). Pang et al.¹⁰⁵ compared the SLD-cylinder model with GCMC simulations for CH_4 adsorption in single-walled carbon nanotubes (SWCNTs). The density profile obtained from GCMC simulation is higher than that from SLD model, and they attributed the deviations to the LCA, inaccurate expression of fluid structure, and repulsive fluid–fluid interaction.

Compared to the OK lattice model, the SLD model is built upon the off-lattice assumption as in NLDFT. In principle, the SLD model can be considered as a simplified model of DFT (e.g., the engineering DFT proposed by Firoozabadi and his co-workers^{30,169,249} uses WDA²⁴³ to extend the PR-EOS to the inhomogeneous conditions). However, due to the LCA and PR-EOS for fluid–fluid interactions, the SLD model generally does not display the layering structures as observed in molecular simulations.^{116,122} In addition, rock heterogeneity and pore size heterogeneity in shale nanoporous media have not been fully taken into account by the SLD model in the current stage.

5.4. Summary about Various Conversion Methods and Remaining Challenges.

While the currently applied models have greatly advanced our understanding toward absolute adsorption characterization in shale nanoporous media at various pressures and temperatures, there still remains daunting challenges. The central challenges arise from the rock heterogeneity and pore size heterogeneity as well as different methane adsorption behaviors in micropores and mesopores. As a result, while the macroscopic thermodynamic models such as Langmuir, SDR, and SBET models are very efficient in terms of data processing, their “one-size-fits-all” approach may not be applicable. In addition, the proposed mechanisms can greatly deviate from methane adsorption behaviors in nanoporous media, and the single-layer adsorption model may become ineligible as shown in molecular simulation works.^{99,279} In this regard, the OK lattice model can capture varying methane adsorption behaviors in micropores and mesopores, and by coupling with PSD, it can have a good agreement with molecular simulations in terms of methane absolute adsorption in model kerogen nanoporous media.¹⁰⁰ However, rock heterogeneity has not been fully taken into account in the present study nor has it been treated without correlating with actual rock composition analysis. Furthermore, the effect of pore geometry has not been investigated well, while most conversion methods are based on slit geometry.

Molecular simulations can be a powerful tool to reveal methane adsorption behaviors in various pores with different rock types, which can complement experimental measurements. However, they need carefully selected molecular models and force fields which should be obtained by explicitly comparing to precisely controlled (rock type, pore size, and pore geometry) porous media to provide reliable predictions.

On the other hand, most experimental measurements on methane adsorption in shale nanoporous media are conducted up to moderate pressure conditions,⁸⁷ while its absolute adsorption at high pressures (which are relevant to actual shale reservoir conditions) is obtained from extrapolation. Pang et al.⁸⁸ have shown that such an extrapolation can result in large errors in terms of absolute adsorption prediction. Therefore, it is suggested to conduct experimental measurements up to high pressure conditions. In addition, Wu et al.¹¹² reported that kerogen swelling and deformation may also greatly affect absolute adsorption prediction as methane adsorption and absorption can occur concurrently during adsorption measurement in shale and isolated kerogen samples. It should be noted that surface roughness may also affect the absolute adsorption calculation as the methane adsorption layer disappears on a rough kerogen surface as shown by Tesson and Firoozabadi.²²⁴ Interestingly, paired with SSA (which can be obtained from PSD with predefined pore geometry), Langmuir and SDR models can have a good agreement with GCMC simulations in terms of methane absolute adsorption in model kerogen nanoporous media.⁸⁸ It is probably because while methane renders varying adsorption behaviors in different pores, the first adsorption layer still dominates the adsorbed gas capacity. This phenomenon also double downs on the importance of reliable characterizations of SSA and PSD.

6. CONCLUDING REMARKS: PROMISES AND CHALLENGES

6.1. Interpretation in Shale Characterizations.

Shale gas has become a dominant natural gas supply in the U.S.,⁷ while natural gas is an important bridge fuel to reach net-zero carbon

emissions.^{2,5} However, due to the inherent rock heterogeneity and the abundant nanoscale pores, the characterization of shale rocks and the determination of methane adsorption in shale nanoporous media face enormous challenges. Thanks to the advancement in various imaging methods (such as SEM), one can directly observe pore structures and geometries in shale, while the observations from these methods are often limited to the target areas and pore connectivity can be hardly revealed. As a result, various indirect observation approaches coupled with different interpretation methods have been used to characterize pore structures including SSA and PSD. Some interpretation methods are built upon microscale and macroscale models (such as the Kelvin equation and Young–Laplace equation), while pores in shale can be as small as sub-1 nm, and pore throat size can be even smaller.²² The validity of these large-scale models in the ultrasmall nanoscale range remains as a debate,²²⁷ while they are embedded in various interpretation methods. On the other hand, the rock heterogeneity (organic and inorganic matters) in shale media adds another layer of difficulty, as most interpretation methods are built upon homogeneous rock properties (such as wettability). There have been attempts to separate different rocks in shale^{150,259} to provide a better interpretation of rock properties. In addition, the nonuniform pore geometries in shale media indicate that the experiences from nanoporous media with a uniform pore geometry²²² cannot be directly applied.

6.2. Absolute Adsorption Conversion. On the other hand, the current state-of-the-art experimental measurements generally obtain excess adsorption, while the absolute adsorption needs to be converted from the excess adsorption. Various excess-adsorption-to-absolute-adsorption methods have been proposed, including constant adsorbed phase density, slope methods, and thermodynamic models (such as Langmuir, SDR, SBET, SLD, and OK). The conversion is either conducted by the assumption of constant adsorbed phase density or constant adsorbed phase volume. Molecular simulations^{99,116} have revealed that the adsorbed phase density is dependent on pressure, temperature, pore size, and rock type, indicating that the constant adsorbed phase density methods may become inapplicable. While these conversion methods have greatly advanced our understanding about the absolute adsorption characterization, they generally do not take into account the rock heterogeneity and pore size heterogeneity. In addition, most methods have been applied under the assumption of a single-layer adsorption model, while molecular simulations indicate that the second adsorption layer which is denoted as a transition zone^{99,279} can exist in methane adsorption in organic and inorganic nanopores. Some thermodynamic models (such as Langmuir and SBET) based on the assumption of adsorption on a single energetically homogeneous surface may also become inapplicable to describe adsorption in micropores and small mesopores in which the overlapped fluid–surface interactions are significant and layering structures emerge.¹¹⁶ In recent works,^{88,100,122} we found that the OK model with various adsorption models coupled with PSD can reliably predict methane absolute adsorption based on the excess adsorption by comparing to GCMC simulations in model kerogen nanoporous media. Interestingly, Langmuir and SDR models coupled with SSA and given adsorption layer thickness can also have a good absolute adsorption prediction.⁸⁸ These studies further emphasize the importance of reliable SSA and PSD for absolute adsorption characterization. However, the rock heterogeneity has not been fully taken into account in these works, which

should be addressed in future works. During the high-pressure methane adsorption process, methane absorption in the kerogen matrix can also occur concurrently with its contribution to the total gas content in kerogen over 20%.¹¹¹ Furthermore, the presence of moisture can also affect methane adsorption behaviors, which is largely ignored in absolute adsorption characterization. Recently, machine learning studies^{386–388} have been reported to account for different factors such as temperature, pressure, TOC, and moisture content on methane adsorption in coal and shale. However, the predicted adsorption isotherm refers to the excess adsorption, while the absolute adsorption still needs to be converted.

Collectively, our review highlights the importance of rock heterogeneity and pore size heterogeneity inherent in shale nanoporous media in pore structure characterizations and methane adsorption behaviors. Due to the so-called dual heterogeneity, one needs to reconsider the commonly used characterization and interpretation methods when it comes to gas adsorption in shale nanoporous media. The accurate SSA and PSD are imperative to the characterization of methane adsorption in shale nanoporous media. We also strongly suggest more synergy and collaborative efforts between experimental measurements from a *macroscopic* perspective and molecular simulations from a *microscopic* perspective in shale gas studies as they can support and provide utterly important guidance to each other.

■ AUTHOR INFORMATION

Corresponding Author

Zhehui Jin – School of Mining and Petroleum Engineering, Department of Civil and Environmental Engineering, University of Alberta, Edmonton, AB T6G 1H9, Canada; orcid.org/0000-0001-8305-5637; Email: zhehui2@ualberta.ca

Authors

Wanying Pang – Key Laboratory of Unconventional Oil & Gas Development, Ministry of Education, Qingdao, China 266580; School of Mining and Petroleum Engineering, Department of Civil and Environmental Engineering, University of Alberta, Edmonton, AB T6G 1H9, Canada

Yingnan Wang – School of Mining and Petroleum Engineering, Department of Civil and Environmental Engineering, University of Alberta, Edmonton, AB T6G 1H9, Canada

Complete contact information is available at: <https://pubs.acs.org/10.1021/acs.energyfuels.1c00357>

Notes

The authors declare no competing financial interest.

Biographies

Wanying Pang is a Ph.D. student in the School of Mining and Petroleum Engineering at the University of Alberta under the supervision of Prof. Zhehui Jin. Her doctoral research investigates hydrocarbon sorption characteristics and absolute adsorption estimation in shale nanoporous media by using statistical thermodynamics approaches. She holds a master's degree in petroleum engineering from the University of Alberta and completed her bachelor's degree at the China University of Petroleum, East China.

Yingnan Wang is a Ph.D. student in the School of Mining and Petroleum Engineering, Department of Civil and Environmental Engineering at the University of Alberta. His current research interests include CO₂ sequestration, thermodynamics of fluids in nanoporous

media, and statistical thermodynamic modeling of phase behavior in shale gas/oil reservoirs. He holds a bachelor's degree in petroleum engineering from Yangtze University and a master's degree in petroleum engineering from the University of Alberta.

Zhehui Jin is an assistant professor in the School of Mining and Petroleum Engineering, at the University of Alberta. His research focuses on the application of molecular modeling and simulations to the development of water treatment materials, unconventional oil/gas resources, enhanced oil recovery, CCUS, and energy storage systems through interdisciplinary studies. He holds a bachelor's degree in materials science and engineering from Tsinghua University and a Ph.D. degree in chemical engineering from the University of California, Riverside.

ACKNOWLEDGMENTS

This work is supported partly by the Opening Fund of Key Laboratory of Unconventional Oil & Gas Development (China University of Petroleum, East China), Ministry of Education, and the Fundamental Research Funds for the Central Universities (19CX05005A-1). The authors also greatly acknowledge a Discovery Grant from the Natural Sciences and Engineering Research Council of Canada (NSERC RGPIN-2017-05080). As a part of the University of Alberta's Future Energy Systems research initiative, this research was made possible in part thanks to funding from the Canada First Research Excellence Fund.

REFERENCES

- (1) Zhang, H.; Cao, D. Molecular simulation of displacement of shale gas by carbon dioxide at different geological depths. *Chem. Eng. Sci.* **2016**, *156*, 121–127.
- (2) *Energy Outlook: 2020 edition*; BP, 2020.
- (3) Weijers, L.; Wright, C.; Mayerhofer, M.; Pearson, M.; Griffin, L.; Weddle, P. Trends in the North American Frac Industry: Invention through the Shale Revolution. In *SPE Hydraulic Fracturing Technology Conference and Exhibition, 2019*; Society of Petroleum Engineers, 2019.
- (4) Hughes, J. D. A reality check on the shale revolution. *Nature* **2013**, *494* (7437), 307–308.
- (5) *Economic and National Security Impacts Under a Hydraulic Fracturing Ban*; U.S. Department of Energy, Washington, DC, January 14, 2021.
- (6) World Shale Resource Assessments. *U.S. Energy Information Administration*. <https://www.eia.gov/analysis/studies/worldshalegas/> (accessed Sep 24, 2021).
- (7) Natural Gas Gross Withdrawals and Production. *U.S. Energy Information Administration*. https://www.eia.gov/dnav/ng/ng_prod_sum_dc_nus_mmcf_a.htm (accessed Feb 26, 2021).
- (8) Dai, J.; Qin, S.; Hu, G.; Ni, Y.; Gan, L.; Huang, S.; Hong, F. Major progress in the natural gas exploration and development in the past seven decades in China. *Petroleum Exploration and Development* **2019**, *46* (6), 1100–1110.
- (9) Annual Energy Outlook 2019 with Projections to 2050. *U.S. Energy Information Administration*. https://www.eia.gov/sites/default/files/resources/AnnualEnergyOutlook_0.pdf (accessed April 2021).
- (10) Fa, G.; Yuan, R.; Lan, J.; Zou, Q.; Li, Z. Net Reserves Evaluation and Sensitivity Analysis of Shale Gas Project under Royalty & Tax System in British Columbia, Canada. In *IOP Conference Series: Earth and Environmental Science*, IOP Publishing, 2019; p 042013.
- (11) Heikkilä, T.; Berardo, R.; Weible, C. M.; Yi, H. A comparative view of advocacy coalitions: Exploring shale development politics in the United States, Argentina, and China. *Journal of Comparative Policy Analysis: research and practice* **2019**, *21* (2), 151–166.
- (12) Wang, S. Shale gas exploitation: Status, problems and prospect. *Natural Gas Industry B* **2018**, *5* (1), 60–74.

- (13) *Annual Energy Outlook 2013*; U.S. Energy Information Administration: Washington, DC, 2013; pp 60–62.

- (14) *Technically Recoverable Shale Oil & Gas Resources: An Assessment of 137 Shale Formations in 41 Countries outside the United States*; U.S. Energy Information Administration, June 2013.

- (15) Lis, A.; Stasik, A. K. Hybrid forums, knowledge deficits and the multiple uncertainties of resource extraction: Negotiating the local governance of shale gas in Poland. *Energy Research & Social Science* **2017**, *28*, 29–36.

- (16) Shar, A. M.; Mahesar, A. A.; Memon, K. R. Could shale gas meet energy deficit: its current status and future prospects. *J. Pet. Explor. Prod. Technol.* **2018**, *8* (4), 957–967.

- (17) Alam, F.; Alam, Q.; Reza, S.; Khurshid-ul-Alam, S.; Saleque, K.; Ahsan, S. Liquefied Natural Gas (LNG) Market and Australia. In *AIP Conference Proceedings*; AIP Publishing LLC, 2017; p 020107.

- (18) Andreasson, S. The bubble that got away? Prospects for shale gas development in South Africa. *Extractive Industries and Society* **2018**, *5* (4), 453–460.

- (19) Li, W.; Wang, C.; Shi, Z.; Wei, Y.; Zhou, H.; Deng, K. The description of shale reservoir pore structure based on method of moments estimation. *PLoS One* **2016**, *11* (3), e0151631.

- (20) Ma, L.; Doney, P. J.; Rutter, E.; Taylor, K. G.; Lee, P. D. A novel upscaling procedure for characterising heterogeneous shale porosity from nanometer-to millimetre-scale in 3D. *Energy* **2019**, *181*, 1285–1297.

- (21) Chalmers, G. R.; Ross, D. J.; Bustin, R. M. Geological controls on matrix permeability of Devonian Gas Shales in the Horn River and Liard basins, northeastern British Columbia, Canada. *Int. J. Coal Geol.* **2012**, *103*, 120–131.

- (22) Chalmers, G. R.; Bustin, R. M.; Power, I. M. Characterization of gas shale pore systems by porosimetry, pycnometry, surface area, and field emission scanning electron microscopy/transmission electron microscopy image analyses: Examples from the Barnett, Woodford, Haynesville, Marcellus, and Doig units. *Characterization of Gas Shale Pore Systems*. *AAPG Bull.* **2012**, *96* (6), 1099–1119.

- (23) Ross, D. J.; Bustin, R. M. The importance of shale composition and pore structure upon gas storage potential of shale gas reservoirs. *Mar. Pet. Geol.* **2009**, *26* (6), 916–927.

- (24) Zhang, M.; Zhan, S.; Jin, Z. Recovery mechanisms of hydrocarbon mixtures in organic and inorganic nanopores during pressure drawdown and CO₂ injection from molecular perspectives. *Chem. Eng. J.* **2020**, *382*, 122808.

- (25) Vandembroucke, M.; Largeau, C. Kerogen origin, evolution and structure. *Org. Geochem.* **2007**, *38* (5), 719–833.

- (26) Demaison, G. J.; Moore, G. T. Anoxic environments and oil source bed genesis. *AAPG Bull.* **1980**, *64* (8), 1179–1209.

- (27) Kelemen, S. R.; Walters, C. C.; Ertas, D.; Kwiatek, L. M.; Curry, D. J. Petroleum Expulsion Part 2. Organic Matter Type and Maturity Effects on Kerogen Swelling by Solvents and Thermodynamic Parameters for Kerogen from Regular Solution Theory. *Energy Fuels* **2006**, *20* (1), 301–308.

- (28) Zhou, J.; Jin, Z.; Luo, K. H. Effects of Moisture Contents on Shale Gas Recovery and CO₂ Sequestration. *Langmuir* **2019**, *35* (26), 8716–8725.

- (29) Ji, L.; Zhang, T.; Milliken, K. L.; Qu, J.; Zhang, X. Experimental investigation of main controls to methane adsorption in clay-rich rocks. *Appl. Geochem.* **2012**, *27* (12), 2533–2545.

- (30) Jin, Z.; Firoozabadi, A. Thermodynamic Modeling of Phase Behavior in Shale Media. *SPE J.* **2016**, *21* (1), 190–207.

- (31) Wu, Y.-S.; Li, J.; Ding, D.; Wang, C.; Di, Y. A generalized framework model for the simulation of gas production in unconventional gas reservoirs. *SPE J.* **2014**, *19* (05), 845–857.

- (32) Xiong, J.; Liu, X.; Liang, L. Experimental study on the pore structure characteristics of the Upper Ordovician Wufeng Formation shale in the southwest portion of the Sichuan Basin, China. *J. Nat. Gas Sci. Eng.* **2015**, *22*, 530–539.

- (33) Wang, T.-Y.; Tian, S.-C.; Liu, Q.-L.; Li, G.-S.; Sheng, M.; Ren, W.-X.; Zhang, P.-P. Pore structure characterization and its effect on methane adsorption in shale kerogen. *Pet. Sci.* **2021**, *18*, 565–578.

- (34) Tian, S.; Dong, X.; Wang, T.; Zhang, R.; Zhang, P.; Sheng, M.; Cheng, S.; Zhao, H.; Fei, L.; Street, J.; Chen, Y.; Xu, Q. Surface properties of organic kerogen in continental and marine shale. *Langmuir* **2018**, *34* (46), 13882–13887.
- (35) Yang, R.; He, S.; Yi, J.; Hu, Q. Nano-scale pore structure and fractal dimension of organic-rich Wufeng-Longmaxi shale from Jiaoshiba area, Sichuan Basin: Investigations using FE-SEM, gas adsorption and helium pycnometry. *Mar. Pet. Geol.* **2016**, *70*, 27–45.
- (36) Curtis, M. E.; Sondergeld, C. H.; Ambrose, R. J.; Rai, C. S. Microstructural investigation of gas shales in two and three dimensions using nanometer-scale resolution imaging. *Microstructure of Gas Shales. AAPG Bull.* **2012**, *96* (4), 665–677.
- (37) Kelly, S.; El-Sobky, H.; Torres-Verdín, C.; Balhoff, M. T. Assessing the utility of FIB-SEM images for shale digital rock physics. *Adv. Water Resour.* **2016**, *95*, 302–316.
- (38) Bernard, S.; Horsfield, B.; Schulz, H.-M.; Wirth, R.; Schreiber, A.; Sherwood, N. Geochemical evolution of organic-rich shales with increasing maturity: A STXM and TEM study of the Posidonia Shale (Lower Toarcian, northern Germany). *Mar. Pet. Geol.* **2012**, *31* (1), 70–89.
- (39) Tian, S.; Wang, T.; Li, G.; Sheng, M.; Zhang, P. Nanoscale Surface Properties of Organic Matter and Clay Minerals in Shale. *Langmuir* **2019**, *35* (17), 5711–5718.
- (40) Javadpour, F.; Moravvej Farshi, M.; Amrein, M. Atomic-force microscopy: a new tool for gas-shale characterization. *Journal of Canadian Petroleum Technology* **2012**, *51* (04), 236–243.
- (41) Tiwari, P.; Deo, M.; Lin, C.; Miller, J. Characterization of oil shale pore structure before and after pyrolysis by using X-ray micro CT. *Fuel* **2013**, *107*, 547–554.
- (42) Sun, Y.; Zhao, Y.; Yuan, L. Quantifying nano-pore heterogeneity and anisotropy in gas shale by synchrotron radiation nano-CT. *Microporous Mesoporous Mater.* **2018**, *258*, 8–16.
- (43) Liu, Y.; Yao, Y.; Liu, D.; Zheng, S.; Sun, G.; Chang, Y. Shale pore size classification: An NMR fluid typing method. *Mar. Pet. Geol.* **2018**, *96*, 591–601.
- (44) Tan, M.; Mao, K.; Song, X.; Yang, X.; Xu, J. NMR petrophysical interpretation method of gas shale based on core NMR experiment. *J. Pet. Sci. Eng.* **2015**, *136*, 100–111.
- (45) Lewis, R.; Singer, P.; Jiang, T.; Rylander, E.; Sinclair, S.; McLin, R. H. NMR T2 Distributions in the Eagle Ford shale: Reflections on Pore Size. In *SPE Unconventional Resources Conference-USA*; Society of Petroleum Engineers, 2013.
- (46) Sun, M.; Yu, B.; Hu, Q.; Yang, R.; Zhang, Y.; Li, B.; Melnichenko, Y. B.; Cheng, G. Pore structure characterization of organic-rich Niutitang shale from China: Small angle neutron scattering (SANS) study. *Int. J. Coal Geol.* **2018**, *186*, 115–125.
- (47) Clarkson, C. R.; Solano, N.; Bustin, R. M.; Bustin, A.; Chalmers, G.; He, L.; Melnichenko, Y. B.; Radliński, A.; Blach, T. P. Pore structure characterization of North American shale gas reservoirs using USANS/SANS, gas adsorption, and mercury intrusion. *Fuel* **2013**, *103*, 606–616.
- (48) Ruppert, L. F.; Sakurovs, R.; Blach, T. P.; He, L.; Melnichenko, Y. B.; Mildner, D. F.; Alcantar-Lopez, L. A USANS/SANS study of the accessibility of pores in the Barnett Shale to methane and water. *Energy Fuels* **2013**, *27* (2), 772–779.
- (49) Mastalerz, M.; He, L.; Melnichenko, Y. B.; Rupp, J. A. Porosity of coal and shale: Insights from gas adsorption and SANS/USANS techniques. *Energy Fuels* **2012**, *26* (8), 5109–5120.
- (50) Psarras, P.; Holmes, R.; Vishal, V.; Wilcox, J. Methane and CO₂ Adsorption Capacities of Kerogen in the Eagle Ford Shale from Molecular Simulation. *Acc. Chem. Res.* **2017**, *50*, 1818–1828.
- (51) Ji, W.; Song, Y.; Jiang, Z.; Meng, M.; Liu, Q.; Chen, L.; Wang, P.; Gao, F.; Huang, H. Fractal characteristics of nano-pores in the Lower Silurian Longmaxi shales from the Upper Yangtze Platform, south China. *Mar. Pet. Geol.* **2016**, *78*, 88–98.
- (52) Ji, W.; Song, Y.; Rui, Z.; Meng, M.; Huang, H. Pore characterization of isolated organic matter from high matured gas shale reservoir. *Int. J. Coal Geol.* **2017**, *174*, 31–40.
- (53) Liu, K.; Ostadhassan, M.; Kong, L. Multifractal characteristics of Longmaxi Shale pore structures by N₂ adsorption: A model comparison. *J. Pet. Sci. Eng.* **2018**, *168*, 330–341.
- (54) Feng, D.; Li, X.; Wang, X.; Li, J.; Sun, F.; Sun, Z.; Zhang, T.; Li, P.; Chen, Y.; Zhang, X. Water adsorption and its impact on the pore structure characteristics of shale clay. *Appl. Clay Sci.* **2018**, *155*, 126–138.
- (55) Külaots, I.; Goldfarb, J. L.; Suuberg, E. M. Characterization of Chinese, American and Estonian oil shale semicokes and their sorptive potential. *Fuel* **2010**, *89* (11), 3300–3306.
- (56) Strapoc, D.; Mastalerz, M.; Schimmelmann, A.; Drobnik, A.; Hasenmueller, N. R. Geochemical constraints on the origin and volume of gas in the New Albany Shale (Devonian–Mississippian), eastern Illinois Basin. *AAPG Bull.* **2010**, *94* (11), 1713–1740.
- (57) Rexer, T. F.; Benham, M. J.; Aplin, A. C.; Thomas, K. M. Methane adsorption on shale under simulated geological temperature and pressure conditions. *Energy Fuels* **2013**, *27* (6), 3099–3109.
- (58) Wang, G.; Ju, Y. Organic shale micropore and mesopore structure characterization by ultra-low pressure N₂ physisorption: Experimental procedure and interpretation model. *J. Nat. Gas Sci. Eng.* **2015**, *27*, 452–465.
- (59) Wang, F.; Guan, J.; Feng, W.; Bao, L. Evolution of overmature marine shale porosity and implication to the free gas volume. *Petroleum Exploration and Development* **2013**, *40* (6), 819–824.
- (60) Romero-Sarmiento, M.-F.; Ducros, M.; Carpentier, B.; Lorant, F.; Cacas, M.-C.; Pegaz-Fiornet, S.; Wolf, S.; Rohais, S.; Moretti, I. Quantitative evaluation of TOC, organic porosity and gas retention distribution in a gas shale play using petroleum system modeling: Application to the Mississippian Barnett Shale. *Mar. Pet. Geol.* **2013**, *45*, 315–330.
- (61) Zhao, P.; Ma, H.; Rasouli, V.; Liu, W.; Cai, J.; Huang, Z. An improved model for estimating the TOC in shale formations. *Mar. Pet. Geol.* **2017**, *83*, 174–183.
- (62) Witte, E.; Schenk, H.; Müller, P.; Schwochau, K. Structural modifications of kerogen during natural evolution as derived from ¹³C CP/MAS NMR, IR spectroscopy and Rock-Eval pyrolysis of Toarcian shales. *Org. Geochem.* **1988**, *13* (4–6), 1039–1044.
- (63) Liao, L.; Wang, Y.; Chen, C.; Shi, S.; Deng, R. Kinetic study of marine and lacustrine shale grains using Rock-Eval pyrolysis: Implications to hydrocarbon generation, retention and expulsion. *Mar. Pet. Geol.* **2018**, *89*, 164–173.
- (64) Rimmer, S. M.; Cantrell, D.; Gooding, P. J. Rock-Eval pyrolysis and vitrinite reflectance trends in the Cleveland Shale Member of the Ohio Shale, eastern Kentucky. *Org. Geochem.* **1993**, *20* (6), 735–745.
- (65) Romero-Sarmiento, M.-F.; Pillot, D.; Letort, G.; Lamoureux-Var, V.; Beaumont, V.; Huc, A.-Y.; Garcia, B. New Rock-Eval method for characterization of unconventional shale resource systems. *Oil Gas Sci. Technol.* **2016**, *71* (3), 37.
- (66) Bai, B.; Elgmati, M.; Zhang, H.; Wei, M. Rock characterization of Fayetteville shale gas plays. *Fuel* **2013**, *105*, 645–652.
- (67) Hupp, B. N.; Donovan, J. J. Quantitative mineralogy for facies definition in the Marcellus Shale (Appalachian Basin, USA) using XRD-XRF integration. *Sediment. Geol.* **2018**, *371*, 16–31.
- (68) Fan, C.; Yan, J.; Huang, Y.; Han, X.; Jiang, X. XRD and TG-FTIR study of the effect of mineral matrix on the pyrolysis and combustion of organic matter in shale char. *Fuel* **2015**, *139*, 502–510.
- (69) Tong, J.; Han, X.; Wang, S.; Jiang, X. Evaluation of structural characteristics of Huadian oil shale kerogen using direct techniques (solid-state ¹³C NMR, XPS, FT-IR, and XRD). *Energy Fuels* **2011**, *25* (9), 4006–4013.
- (70) Zhang, T.; Ellis, G. S.; Ruppel, S. C.; Milliken, K.; Yang, R. Effect of organic-matter type and thermal maturity on methane adsorption in shale-gas systems. *Org. Geochem.* **2012**, *47*, 120–131.
- (71) Wu, X.; Ning, Z.; Qi, R.; Wang, Q.; Huang, L. Pore characterization and inner adsorption mechanism investigation for methane in organic and inorganic matters of shale. *Energy Fuels* **2020**, *34* (4), 4106–4115.

- (72) Gasparik, M.; Bertier, P.; Gensterblum, Y.; Ghanizadeh, A.; Krooss, B. M.; Littke, R. Geological controls on the methane storage capacity in organic-rich shales. *Int. J. Coal Geol.* **2014**, *123*, 34–51.
- (73) Li, X.; Krooss, B. M. Influence of grain size and moisture content on the high-pressure methane sorption capacity of Kimmeridge Clay. *Energy Fuels* **2017**, *31* (11), 11548–11557.
- (74) Wang, C.; Wang, F.; Du, H.; Zhang, X. Is China really ready for shale gas revolution—Re-evaluating shale gas challenges. *Environ. Sci. Policy* **2014**, *39*, 49–55.
- (75) Zou, C.; Dong, D.; Wang, S.; Li, J.; Li, X.; Wang, Y.; Li, D.; Cheng, K. Geological characteristics and resource potential of shale gas in China. *Petroleum exploration and development* **2010**, *37* (6), 641–653.
- (76) Yang, F.; Ning, Z.; Wang, Q.; Zhang, R.; Krooss, B. M. Pore structure characteristics of lower Silurian shales in the southern Sichuan Basin, China: Insights to pore development and gas storage mechanism. *Int. J. Coal Geol.* **2016**, *156*, 12–24.
- (77) Li, T.; Jiang, Z.; Li, Z.; Wang, P.; Xu, C.; Liu, G.; Su, S.; Ning, C. Continental shale pore structure characteristics and their controlling factors: A case study from the lower third member of the Shahejie Formation, Zhanhua Sag, Eastern China. *J. Nat. Gas Sci. Eng.* **2017**, *45*, 670–692.
- (78) Feng, G.; Zhu, Y.; Chen, S.; Wang, Y.; Ju, W.; Hu, Y.; You, Z.; Wang, G. G. Supercritical Methane Adsorption on Shale over Wide Pressure and Temperature Ranges: Implications for Gas-in-Place Estimation. *Energy Fuels* **2020**, *34* (3), 3121–3134.
- (79) Yuan, W.; Pan, Z.; Li, X.; Yang, Y.; Zhao, C.; Connell, L. D.; Li, S.; He, J. Experimental study and modelling of methane adsorption and diffusion in shale. *Fuel* **2014**, *117*, 509–519.
- (80) Li, J.; Wu, K.; Chen, Z.; Wang, W.; Yang, B.; Wang, K.; Luo, J.; Yu, R. Effects of energetic heterogeneity on gas adsorption and gas storage in geologic shale systems. *Appl. Energy* **2019**, *251*, 113368.
- (81) Wang, K.; Zhang, B.; Kang, T. Effect of Geological Depths on CH₄ Adsorption, Diffusion, and Swelling in Kaolinite by Molecular Simulations. *Energy Fuels* **2020**, *34* (2), 1620–1626.
- (82) Liu, X.-Q.; Li, M.; Zhang, C.; Fang, R.; Zhong, N.; Xue, Y.; Zhou, Y.; Jiang, W.; Chen, X.-Y. Mechanistic insight into the optimal recovery efficiency of CBM in sub-bituminous coal through molecular simulation. *Fuel* **2020**, *266*, 117137.
- (83) Zou, C.; Dong, D.; Wang, Y.; Li, X.; Huang, J.; Wang, S.; Guan, Q.; Zhang, C.; Wang, H.; Liu, H.; Bai, W.; Liang, F.; Lin, W.; Zhao, Q.; Liu, D.; Yang, Z.; Liang, P.; Sun, S.; Qiu, Z. Shale gas in China: Characteristics, challenges and prospects (I). *Petroleum Exploration and Development* **2015**, *42* (6), 753–767.
- (84) Cipolla, C. L.; Lolon, E.; Erdle, J.; Tathed, V. Modeling Well Performance in Shale-Gas Reservoirs. In *SPE/EAGE Reservoir Characterization & Simulation Conference*; European Association of Geoscientists & Engineers, 2009; pp cp-170–00045.
- (85) Duan, X.; Hu, Z.; Gao, S.; Shen, R.; Liu, H.; Chang, J.; Wang, L. Shale high pressure isothermal adsorption curve and the production dynamic experiments of gas well. *Petroleum Exploration and Development* **2018**, *45* (1), 127–135.
- (86) Curtis, J. B. Fractured shale-gas systems. *AAPG Bull.* **2002**, *86* (11), 1921–1938.
- (87) Zhou, S.; Xue, H.; Ning, Y.; Guo, W.; Zhang, Q. Experimental study of supercritical methane adsorption in Longmaxi shale: Insights into the density of adsorbed methane. *Fuel* **2018**, *211*, 140–148.
- (88) Pang, W.; Ye, Y.; Jin, Z. Assessment of Various Approaches in the Prediction of Methane Absolute Adsorption in Kerogen Nanoporous Media. *Energy Fuels* **2019**, *33*, 6258–6263.
- (89) Gensterblum, Y.; Van Hemert, P.; Billefont, P.; Busch, A.; Charrier, D.; Li, D.; Krooss, B. M.; De Weireld, G.; Prinz, D.; Wolf, K.-H. European inter-laboratory comparison of high pressure CO₂ sorption isotherms. I: Activated carbon. *Carbon* **2009**, *47* (13), 2958–2969.
- (90) Zhou, L.; Bai, S.; Su, W.; Yang, J.; Zhou, Y. Comparative study of the excess versus absolute adsorption of CO₂ on superactivated carbon for the near-critical region. *Langmuir* **2003**, *19* (7), 2683–2690.
- (91) Zhou, L.; Zhou, Y.; Li, M.; Chen, P.; Wang, Y. Experimental and modeling study of the adsorption of supercritical methane on a high surface activated carbon. *Langmuir* **2000**, *16* (14), 5955–5959.
- (92) Khosrokhavar, R.; Wolf, K.-H.; Bruining, H. Sorption of CH₄ and CO₂ on a carboniferous shale from Belgium using a manometric setup. *Int. J. Coal Geol.* **2014**, *128*, 153–161.
- (93) Zhang, J.; Clennell, M. B.; Liu, K.; Pervukhina, M.; Chen, G.; Dewhurst, D. N. Methane and carbon dioxide adsorption on Illite. *Energy Fuels* **2016**, *30* (12), 10643–10652.
- (94) Gasparik, M.; Ghanizadeh, A.; Bertier, P.; Gensterblum, Y.; Bouw, S.; Krooss, B. M. High-pressure methane sorption isotherms of black shales from the Netherlands. *Energy Fuels* **2012**, *26* (8), 4995–5004.
- (95) Tian, H.; Li, T.; Zhang, T.; Xiao, X. Characterization of methane adsorption on overmature Lower Silurian–Upper Ordovician shales in Sichuan Basin, southwest China: Experimental results and geological implications. *Int. J. Coal Geol.* **2016**, *156*, 36–49.
- (96) Rexer, T. F.; Mathia, E. J.; Aplin, A. C.; Thomas, K. M. High-Pressure Methane Adsorption and Characterization of Pores in Posidonia Shales and Isolated Kerogens. *Energy Fuels* **2014**, *28* (5), 2886–2901.
- (97) Chen, L.; Jiang, Z.; Liu, K.; Ji, W.; Wang, P.; Gao, F.; Hu, T. Application of Langmuir and Dubinin–Radushkevich models to estimate methane sorption capacity on two shale samples from the Upper Triassic Chang 7 Member in the southeastern Ordos Basin, China. *Energy Explor. Exploit.* **2017**, *35* (1), 122–144.
- (98) Sakurovs, R.; Day, S.; Weir, S.; Duffy, G. Application of a modified Dubinin–Radushkevich equation to adsorption of gases by coals under supercritical conditions. *Energy Fuels* **2007**, *21* (2), 992–997.
- (99) Tian, Y.; Yan, C.; Jin, Z. Characterization of Methane Excess and Absolute Adsorption in Various Clay Nanopores from Molecular Simulation. *Sci. Rep.* **2017**, *7* (1), 12040.
- (100) Pang, W.; Jin, Z. Methane Absolute Adsorption in Kerogen Nanoporous Media with Realistic Continuous Pore Size Distributions. *Energy Fuels* **2020**, *34* (10), 12158–12172.
- (101) Yu, W.; Sepehrmoori, K.; Patzek, T. W. Modeling gas adsorption in Marcellus shale with Langmuir and BET isotherms. *SPE J.* **2016**, *21* (02), 589.
- (102) Merey, S.; Sinayuc, C. Analysis of carbon dioxide sequestration in shale gas reservoirs by using experimental adsorption data and adsorption models. *J. Nat. Gas Sci. Eng.* **2016**, *36*, 1087–1105.
- (103) Zhou, S.; Zhang, D.; Wang, H.; Li, X. A modified BET equation to investigate supercritical methane adsorption mechanisms in shale. *Mar. Pet. Geol.* **2019**, *105*, 284–292.
- (104) Liu, Y.; Hou, J.; Wang, C. Absolute adsorption of CH₄ on shale with the simplified local-density theory. *SPE J.* **2020**, *25* (01), 212–225.
- (105) Pang, Y.; Hu, X.; Wang, S.; Chen, S.; Soliman, M. Y.; Deng, H. Characterization of adsorption isotherm and density profile in cylindrical nanopores: modeling and measurement. *Chem. Eng. J.* **2020**, *396*, 125212.
- (106) Mohammad, S. A.; Sudibandriyo, M.; Fitzgerald, J. E.; Liang, X.; Robinson, R. L., Jr; Gasem, K. A. Measurements and modeling of excess adsorption of pure and mixed gases on wet coals. *Energy Fuels* **2012**, *26* (5), 2899–2910.
- (107) Sudibandriyo, M.; Mohammad, S. A.; Robinson, R. L.; Gasem, K. A. Ono–Kondo lattice model for high-pressure adsorption: Pure gases. *Fluid Phase Equilib.* **2010**, *299* (2), 238–251.
- (108) Xiong, F.; Rother, G.; Tomasko, D.; Pang, W.; Moortgat, J. On the pressure and temperature dependence of adsorption densities and other thermodynamic properties in gas shales. *Chem. Eng. J.* **2020**, *395*, 124989.
- (109) Hwang, J.; Pini, R. Supercritical CO₂ and CH₄ uptake by Illite-smectite clay minerals. *Environ. Sci. Technol.* **2019**, *53* (19), 11588–11596.
- (110) Memon, A.; Li, A.; Memon, B. S.; Muther, T.; Han, W.; Kashif, M.; Tahir, M. U.; Akbar, I. Gas adsorption and controlling factors of shale: review, application, comparison and challenges. *Nat. Resour. Res.* **2021**, *30*, 827–848.

- (111) Etminan, S. R.; Javadpour, F.; Maini, B. B.; Chen, Z. Measurement of gas storage processes in shale and of the molecular diffusion coefficient in kerogen. *Int. J. Coal Geol.* **2014**, *123*, 10–19.
- (112) Wu, T.; Zhao, H.; Tesson, S.; Firoozabadi, A. Absolute adsorption of light hydrocarbons and carbon dioxide in shale rock and isolated kerogen. *Fuel* **2019**, *235*, 855–867.
- (113) Zhao, H.; Wu, T.; Firoozabadi, A. High pressure sorption of various hydrocarbons and carbon dioxide in Kimmeridge Blackstone and isolated kerogen. *Fuel* **2018**, *224*, 412–423.
- (114) Xiong, J.; Liu, X.; Liang, L.; Zeng, Q. Adsorption of methane in organic-rich shale nanopores: An experimental and molecular simulation study. *Fuel* **2017**, *200*, 299–315.
- (115) Wang, T.; Tian, S.; Li, G.; Sheng, M.; Ren, W.; Liu, Q.; Zhang, S. Molecular simulation of CO₂/CH₄ competitive adsorption on shale kerogen for CO₂ sequestration and enhanced gas recovery. *J. Phys. Chem. C* **2018**, *122* (30), 17009–17018.
- (116) Mosher, K.; He, J.; Liu, Y.; Rupp, E.; Wilcox, J. Molecular simulation of methane adsorption in micro- and mesoporous carbons with applications to coal and gas shale systems. *Int. J. Coal Geol.* **2013**, *109*, 36–44.
- (117) Liu, J.; Xi, S.; Chapman, W. G. Competitive Sorption of CO₂ with Gas Mixtures in Nanoporous Shale for Enhanced Gas Recovery from Density Functional Theory. *Langmuir* **2019**, *35* (24), 8144–8158.
- (118) Song, W.; Yao, J.; Ma, J.; Li, A.; Li, Y.; Sun, H.; Zhang, L. Grand canonical Monte Carlo simulations of pore structure influence on methane adsorption in micro-porous carbons with applications to coal and shale systems. *Fuel* **2018**, *215*, 196–203.
- (119) Huang, L.; Ning, Z.; Wang, Q.; Qi, R.; Zeng, Y.; Qin, H.; Ye, H.; Zhang, W. Molecular simulation of adsorption behaviors of methane, carbon dioxide and their mixtures on kerogen: Effect of kerogen maturity and moisture content. *Fuel* **2018**, *211*, 159–172.
- (120) Zhou, J.; Jin, Z.; Luo, K. H. The role of brine in gas adsorption and dissolution in kerogen nanopores for enhanced gas recovery and CO₂ sequestration. *Chem. Eng. J.* **2020**, *399*, 125704.
- (121) Huang, L.; Ning, Z.; Wang, Q.; Qi, R.; Cheng, Z.; Wu, X.; Zhang, W.; Qin, H. Molecular Insights into Kerogen Deformation Induced by CO₂/CH₄ Sorption: Effect of Maturity and Moisture. *Energy Fuels* **2019**, *33*, 4792–4805.
- (122) Pang, W.; He, Y.; Yan, C.; Jin, Z. Tackling the challenges in the estimation of methane absolute adsorption in kerogen nanoporous media from molecular and analytical approaches. *Fuel* **2019**, *242*, 687–698.
- (123) Wang, H.; Qu, Z.; Yin, Y.; Bai, J.; Yu, B. Review of molecular simulation method for gas adsorption/desorption and diffusion in shale matrix. *J. Therm. Sci.* **2019**, *28* (1), 1–16.
- (124) Striolo, A.; Cole, D. R. Understanding shale gas: Recent progress and remaining challenges. *Energy Fuels* **2017**, *31* (10), 10300–10310.
- (125) Tang, X.; Ripepi, N.; Luxbacher, K.; Pitcher, E. Adsorption models for methane in shales: Review, comparison, and application. *Energy Fuels* **2017**, *31* (10), 10787–10801.
- (126) Yu, H.; Xu, H.; Fan, J.; Zhu, Y.-B.; Wang, F.; Wu, H. Transport of Shale Gas in Microporous/Nanoporous Media: Molecular to Pore-Scale Simulations. *Energy Fuels* **2021**, *35* (2), 911–943.
- (127) Lan, Y.; Yang, Z.; Wang, P.; Yan, Y.; Zhang, L.; Ran, J. A review of microscopic seepage mechanism for shale gas extracted by supercritical CO₂ flooding. *Fuel* **2019**, *238*, 412–424.
- (128) Ma, L.; Fauchille, A.-L.; Dowey, P. J.; Pilz, F. F.; Courtois, L.; Taylor, K. G.; Lee, P. D. Correlative Multi-Scale Imaging of Shales: A Review and Future Perspectives. *Geol. Soc. Spec. Publ.* **2017**, *454* (1), 175–199.
- (129) Topór, T.; Derkowski, A.; Ziemiański, P.; Szczerowski, J.; McCarty, D. K. The effect of organic matter maturation and porosity evolution on methane storage potential in the Baltic Basin (Poland) shale-gas reservoir. *Int. J. Coal Geol.* **2017**, *180*, 46–56.
- (130) Milliken, K. L.; Rudnicki, M.; Awwiller, D. N.; Zhang, T. Organic matter-hosted pore system, Marcellus formation (Devonian), Pennsylvania. *AAPG Bull.* **2013**, *97* (2), 177–200.
- (131) Hu, Q.; Ewing, R. P.; Dultz, S. Low pore connectivity in natural rock. *J. Contam. Hydrol.* **2012**, *133*, 76–83.
- (132) Curtis, M. E.; Ambrose, R. J.; Sondergeld, C. H.; Rai, C. S. Transmission and Scanning Electron Microscopy Investigation of Pore Connectivity of Gas Shales on the Nanoscale. In *North American Unconventional Gas Conference and Exhibition*; Society of Petroleum Engineers, 2011.
- (133) King, H. E., Jr.; Eberle, A. P.; Walters, C. C.; Kliever, C. E.; Ertas, D.; Huynh, C. Pore architecture and connectivity in gas shale. *Energy Fuels* **2015**, *29* (3), 1375–1390.
- (134) Loucks, R. G.; Reed, R. M.; Ruppel, S. C.; Hammes, U. Spectrum of pore types and networks in mudrocks and a descriptive classification for matrix-related mudrock pores. *AAPG Bull.* **2012**, *96* (6), 1071–1098.
- (135) Loucks, R. G.; Reed, R. M.; Ruppel, S. C.; Jarvie, D. M. Morphology, genesis, and distribution of nanometer-scale pores in siliceous mudstones of the Mississippian Barnett Shale. *J. Sediment. Res.* **2009**, *79* (12), 848–861.
- (136) Giffin, S.; Littke, R.; Klaver, J.; Urai, J. Application of BIB-SEM technology to characterize macropore morphology in coal. *Int. J. Coal Geol.* **2013**, *114*, 85–95.
- (137) Nie, B.; Liu, X.; Yang, L.; Meng, J.; Li, X. Pore structure characterization of different rank coals using gas adsorption and scanning electron microscopy. *Fuel* **2015**, *158*, 908–917.
- (138) Elgmati, M. M.; Zhang, H.; Bai, B.; Flori, R. E.; Qu, Q. Submicron-Pore Characterization of Shale Gas Plays. In *North American Unconventional Gas Conference and Exhibition*; Society of Petroleum Engineers, 2011.
- (139) Klaver, J.; Desbois, G.; Littke, R.; Urai, J. L. BIB-SEM pore characterization of mature and post mature Posidonia Shale samples from the Hils area, Germany. *Int. J. Coal Geol.* **2016**, *158*, 78–89.
- (140) Yang, F.; Ning, Z.; Liu, H. Fractal characteristics of shales from a shale gas reservoir in the Sichuan Basin, China. *Fuel* **2014**, *115*, 378–384.
- (141) Ma, Y.; Pan, Z.; Zhong, N.; Connell, L. D.; Down, D. I.; Lin, W.; Zhang, Y. Experimental study of anisotropic gas permeability and its relationship with fracture structure of Longmaxi Shales, Sichuan Basin, China. *Fuel* **2016**, *180*, 106–115.
- (142) Gou, Q.; Xu, S.; Hao, F.; Yang, F.; Zhang, B.; Shu, Z.; Zhang, A.; Wang, Y.; Lu, Y.; Cheng, X.; Qing, J.; Gao, M. Full-scale pores and micro-fractures characterization using FE-SEM, gas adsorption, nano-CT and micro-CT: A case study of the Silurian Longmaxi Formation shale in the Fuling area, Sichuan Basin, China. *Fuel* **2019**, *253*, 167–179.
- (143) Yang, B.; Kang, Y.; Lu, X.; You, L.; Zhang, H.; Chen, Z. Experimental investigation of the pore shape factor in fluid imbibition model—taking the Longmaxi shale in Sichuan Basin as examples. *J. Pet. Sci. Eng.* **2020**, *193*, 107327.
- (144) Guo, X.; Shen, Y.; He, S. Quantitative pore characterization and the relationship between pore distributions and organic matter in shale based on Nano-CT image analysis: a case study for a lacustrine shale reservoir in the Triassic Chang 7 member, Ordos Basin, China. *J. Nat. Gas Sci. Eng.* **2015**, *27*, 1630–1640.
- (145) Tang, X.; Jiang, Z.; Jiang, S.; Li, Z. Heterogeneous nanoporosity of the Silurian Longmaxi Formation shale gas reservoir in the Sichuan Basin using the QFMSCAN, FIB-SEM, and nano-CT methods. *Mar. Pet. Geol.* **2016**, *78*, 99–109.
- (146) Cao, T.; Song, Z.; Wang, S.; Xia, J. Characterization of pore structure and fractal dimension of Paleozoic shales from the northeastern Sichuan Basin, China. *J. Nat. Gas Sci. Eng.* **2016**, *35*, 882–895.
- (147) Chen, Z.; Song, Y.; Li, Z.; Liu, S.; Li, Y.; Liu, G.; Yang, W.; Wang, Q.; Yang, Y.; Gao, F. The occurrence characteristics and removal mechanism of residual water in marine shales: A case study of Wufeng-Longmaxi shale in Changning-Weiyuan area, Sichuan basin. *Fuel* **2019**, *253*, 1056–1070.
- (148) Xue, S.; Lu, S.; Xue, H.; Yang, J.; Tang, M.; Liu, S. Similarities and Differences between Marine and Continental Shale Gas. *Acta Geol. Sin. (Engl. Ed.)* **2015**, *89*, 288–289.

- (149) Guo, S.; Fu, J.; Gao, D.; Li, H.; Huang, J. Research status and prospects for marine-continental shale gases in China. *Petroleum Geology Experiment* **2015**, *37* (5), 535–540.
- (150) Xiong, F.; Jiang, Z.; Li, P.; Wang, X.; Bi, H.; Li, Y.; Wang, Z.; Amooie, M. A.; Soltanian, M. R.; Moortgat, J. Pore structure of transitional shales in the Ordos Basin, NW China: Effects of composition on gas storage capacity. *Fuel* **2017**, *206*, 504–515.
- (151) Han, H.; Pang, P.; Zhong, N.; Luo, Q.; Ma, Y.; Gao, Y. The pore characteristics and gas potential of the Jurassic continental shales in the middle-small basins, northwest China. *J. Pet. Sci. Eng.* **2020**, *188*, 106873.
- (152) Wu, Y.; Fan, T.; Jiang, S.; Yang, X.; Ding, H.; Meng, M.; Wei, D. Methane adsorption capacities of the lower paleozoic marine shales in the Yangtze Platform, South China. *Energy Fuels* **2015**, *29* (7), 4160–4167.
- (153) Cheng, A.-L.; Huang, W.-L. Selective adsorption of hydrocarbon gases on clays and organic matter. *Org. Geochem.* **2004**, *35* (4), 413–423.
- (154) Zhai, Z.; Wang, X.; Jin, X.; Sun, L.; Li, J.; Cao, D. Adsorption and diffusion of shale gas reservoirs in modeled clay minerals at different geological depths. *Energy Fuels* **2014**, *28* (12), 7467–7473.
- (155) Chávez-Páez, M.; Van Workum, K.; De Pablo, L.; de Pablo, J. J. Monte Carlo simulations of Wyoming sodium montmorillonite hydrates. *J. Chem. Phys.* **2001**, *114* (3), 1405–1413.
- (156) Pang, Y.; He, Y.; Chen, S. An innovative method to characterize sorption-induced kerogen swelling in organic-rich shales. *Fuel* **2019**, *254*, 115629.
- (157) Hu, H. Methane adsorption comparison of different thermal maturity kerogens in shale gas system. *Chin. J. Geochem.* **2014**, *33* (4), 425–430.
- (158) Yang, B.; Kang, Y.; You, L.; Li, X.; Chen, Q. Measurement of the surface diffusion coefficient for adsorbed gas in the fine mesopores and micropores of shale organic matter. *Fuel* **2016**, *181*, 793–804.
- (159) Liu, K.; Ostadhassan, M.; Zou, J.; Gentzis, T.; Rezaee, R.; Bubach, B.; Carvajal-Ortiz, H. Nanopore structures of isolated kerogen and bulk shale in Bakken Formation. *Fuel* **2018**, *226*, 441–453.
- (160) Yuan, Y.; Rezaee, R.; Al-Khdheawi, E. A.; Hu, S.-Y.; Verrall, M.; Zou, J.; Liu, K. Impact of Composition on Pore Structure Properties in Shale: Implications for Micro-/Mesopore Volume and Surface Area Prediction. *Energy Fuels* **2019**, *33* (10), 9619–9628.
- (161) Kuila, U.; Prasad, M. Specific surface area and pore-size distribution in clays and shales. *Geophys. Prospect.* **2013**, *61* (2), 341–362.
- (162) Modica, C. J.; Lapierre, S. G. Estimation of kerogen porosity in source rocks as a function of thermal transformation: Example from the Mowry Shale in the Powder River Basin of Wyoming. Estimation of Kerogen Porosity as a Function of Thermal Transformation. *AAPG Bull.* **2012**, *96* (1), 87–108.
- (163) Curtis, M. E.; Cardott, B. J.; Sondergeld, C. H.; Rai, C. S. Development of organic porosity in the Woodford Shale with increasing thermal maturity. *Int. J. Coal Geol.* **2012**, *103*, 26–31.
- (164) Heller, R.; Zoback, M. Adsorption of methane and carbon dioxide on gas shale and pure mineral samples. *Journal of Unconventional Oil and Gas Resources* **2014**, *8*, 14–24.
- (165) Handwerger, D. A.; Willberg, D. M.; Pagels, M.; Rowland, B.; Keller, J. F. Reconciling Retort versus Dean Stark Measurements on Tight Shales. In *SPE Annual Technical Conference and Exhibition*; Society of Petroleum Engineers, 2012.
- (166) Wang, F. P.; Reed, R. M. Pore Networks and Fluid Flow in Gas Shales. In *SPE Annual Technical Conference and Exhibition*; Society of Petroleum Engineers, 2009.
- (167) Sondergeld, C. H.; Newsham, K. E.; Comisky, J. T.; Rice, M. C.; Rai, C. S. In *Petrophysical Considerations in Evaluating and Producing Shale Gas Resources*. In *SPE Unconventional Gas Conference*; Society of Petroleum Engineers, 2010.
- (168) Passey, Q. R.; Bohacs, K.; Esch, W. L.; Klimentidis, R.; Sinha, S. From Oil-Prone Source Rock to Gas-Producing Shale Reservoir-Geologic and Petrophysical Characterization of Unconventional Shale Gas Reservoirs. In *International Oil and Gas Conference and Exhibition in China*; Society of Petroleum Engineers, 2010.
- (169) Li, Z.; Jin, Z.; Firoozabadi, A. Phase Behavior and Adsorption of Pure Substances and Mixtures and Characterization in Nanopore Structures by Density Functional Theory. *SPE J.* **2014**, *19* (6), 1096–1109.
- (170) Gu, X.; Mildner, D. F.; Cole, D. R.; Rother, G.; Slingerland, R.; Brantley, S. L. Quantification of organic porosity and water accessibility in Marcellus shale using neutron scattering. *Energy Fuels* **2016**, *30* (6), 4438–4449.
- (171) Yuan, Y.; Rezaee, R. Fractal analysis of the pore structure for clay bound water and potential gas storage in shales based on NMR and N₂ gas adsorption. *J. Pet. Sci. Eng.* **2019**, *177*, 756–765.
- (172) Zou, J.; Rezaee, R.; Xie, Q.; You, L.; Liu, K.; Saeedi, A. Investigation of moisture effect on methane adsorption capacity of shale samples. *Fuel* **2018**, *232*, 323–332.
- (173) Li, J.; Li, X.; Wang, X.; Li, Y.; Wu, K.; Shi, J.; Yang, L.; Feng, D.; Zhang, T.; Yu, P. Water distribution characteristic and effect on methane adsorption capacity in shale clay. *Int. J. Coal Geol.* **2016**, *159*, 135–154.
- (174) Zou, J.; Rezaee, R.; Xie, Q.; You, L. Characterization of the combined effect of high temperature and moisture on methane adsorption in shale gas reservoirs. *J. Pet. Sci. Eng.* **2019**, *182*, 106353.
- (175) Chalmers, G. R.; Bustin, R. M. Lower Cretaceous gas shales in northeastern British Columbia, Part I: geological controls on methane sorption capacity. *Bull. Can. Pet. Geol.* **2008**, *56* (1), 1–21.
- (176) Liu, H.; Wang, H. Adsorptivity and influential factors of marine shales in South China. *Natural Gas Industry* **2012**, *32* (9), 5–9.
- (177) Joubert, J. I.; Grein, C. T.; Bienstock, D. Effect of moisture on the methane capacity of American coals. *Fuel* **1974**, *53* (3), 186–191.
- (178) Cao, T.; Song, Z.; Wang, S.; Xia, J. A comparative study of the specific surface area and pore structure of different shales and their kerogens. *Sci. China: Earth Sci.* **2015**, *58* (4), 510–522.
- (179) Kibria, M. G.; Hu, Q.; Liu, H.; Zhang, Y.; Kang, J. Pore structure, wettability, and spontaneous imbibition of Woodford shale, Permian Basin, West Texas. *Mar. Pet. Geol.* **2018**, *91*, 735–748.
- (180) Gao, Z.; Yang, S.; Jiang, Z.; Zhang, K.; Chen, L. Investigating the spontaneous imbibition characteristics of continental Jurassic Ziliujing Formation shale from the northeastern Sichuan Basin and correlations to pore structure and composition. *Mar. Pet. Geol.* **2018**, *98*, 697–705.
- (181) Wang, Y.; Zhu, Y.; Liu, S.; Zhang, R. Pore characterization and its impact on methane adsorption capacity for organic-rich marine shales. *Fuel* **2016**, *181*, 227–237.
- (182) Bahadur, J.; Melnichenko, Y.; Mastalerz, M.; Furmann, A.; Clarkson, C. R. Hierarchical pore morphology of cretaceous shale: a small-angle neutron scattering and ultrasmall-angle neutron scattering study. *Energy Fuels* **2014**, *28* (10), 6336–6344.
- (183) Yao, Y.; Liu, D.; Che, Y.; Tang, D.; Tang, S.; Huang, W. Petrophysical characterization of coals by low-field nuclear magnetic resonance (NMR). *Fuel* **2010**, *89* (7), 1371–1380.
- (184) Kleinberg, R. L. Utility of NMR T₂ distributions, connection with capillary pressure, clay effect, and determination of the surface relaxivity parameter ρ_2 . *Magn. Reson. Imaging* **1996**, *14* (7–8), 761–767.
- (185) Wang, Y.; Zhu, Y.; Chen, S.; Li, W. Characteristics of the Nanoscale Pore Structure in Northwestern Hunan Shale Gas Reservoirs Using Field Emission Scanning Electron Microscopy, High-Pressure Mercury Intrusion, and Gas Adsorption. *Energy Fuels* **2014**, *28*, 945–955.
- (186) Wei, M.; Xiong, Y.; Zhang, L.; Li, J.; Peng, P. The effect of sample particle size on the determination of pore structure parameters in shales. *Int. J. Coal Geol.* **2016**, *163*, 177–185.
- (187) Bahadur, J.; Radlinski, A. P.; Melnichenko, Y. B.; Mastalerz, M.; Schimmelmann, A. Small-angle and ultrasmall-angle neutron scattering (SANS/USANS) study of New Albany Shale: a treatise on microporosity. *Energy Fuels* **2015**, *29* (2), 567–576.
- (188) Melnichenko, Y.; Radlinski, A.; Mastalerz, M.; Cheng, G.; Rupp, J. Characterization of the CO₂ fluid adsorption in coal as a function of

- pressure using neutron scattering techniques (SANS and USANS). *Int. J. Coal Geol.* **2009**, *77* (1–2), 69–79.
- (189) Radlinski, A.; Mastalerz, M.; Hinde, A.; Hainbuchner, M.; Rauch, H.; Baron, M.; Lin, J.; Fan, L.; Thiyagarajan, P. Application of SAXS and SANS in evaluation of porosity, pore size distribution and surface area of coal. *Int. J. Coal Geol.* **2004**, *59* (3–4), 245–271.
- (190) Radliński, A.; Boreham, C.; Lindner, P.; Randl, O.; Wignall, G.; Hinde, A.; Hope, J. Small angle neutron scattering signature of oil generation in artificially and naturally matured hydrocarbon source rocks. *Org. Geochem.* **2000**, *31* (1), 1–14.
- (191) Sigal, R. F. Pore-size distributions for organic-shale-reservoir rocks from nuclear-magnetic-resonance spectra combined with adsorption measurements. *SPE J.* **2015**, *20* (04), 824–830.
- (192) Li, J.; Lu, S.; Jiang, C.; Wang, M.; Chen, Z.; Chen, G.; Li, J.; Lu, S. Characterization of shale pore size distribution by NMR considering the influence of shale skeleton signals. *Energy Fuels* **2019**, *33* (7), 6361–6372.
- (193) Washburn, E. W. Note on a method of determining the distribution of pore sizes in a porous material. *Proc. Natl. Acad. Sci. U. S. A.* **1921**, *7* (4), 115.
- (194) Giesche, H. Mercury porosimetry: a general (practical) overview. *Particle & particle systems characterization* **2006**, *23* (1), 9–19.
- (195) Penumadu, D.; Dean, J. Compressibility effect in evaluating the pore-size distribution of kaolin clay using mercury intrusion porosimetry. *Can. Geotech. J.* **2000**, *37* (2), 393–405.
- (196) Diamond, S. Pore size distributions in clays. *Clays Clay Miner.* **1970**, *18* (1), 7–23.
- (197) Gao, Z.; Hu, Q.; Hamamoto, S. Using Multicycle Mercury Intrusion Porosimetry to Investigate Hysteresis Phenomenon of Different Porous Media. *J. Porous Media* **2018**, *21* (7), 607.
- (198) Sang, G.; Liu, S.; Zhang, R.; Elsworth, D.; He, L. Nanopore characterization of mine roof shales by SANS, nitrogen adsorption, and mercury intrusion: Impact on water adsorption/retention behavior. *Int. J. Coal Geol.* **2018**, *200*, 173–185.
- (199) Zhang, P.; Lu, S.; Li, J.; Zhang, J.; Xue, H.; Chen, C. Comparisons of SEM, low-field NMR, and mercury intrusion capillary pressure in characterization of the pore size distribution of lacustrine shale: a case study on the Dongying Depression, Bohai Bay Basin, China. *Energy Fuels* **2017**, *31* (9), 9232–9239.
- (200) Lowell, S.; Shields, J. E.; Thomas, M. A.; Thommes, M. *Characterization of Porous Solids and Powders: Surface Area, Pore Size and Density*; Springer Science & Business Media, 2012; Vol. 16.
- (201) Xi, Z.; Tang, S.; Zhang, S.; Sun, K. Pore structure characteristics of marine–continental transitional shale: A case study in the Qinshui Basin, China. *Energy Fuels* **2017**, *31* (8), 7854–7866.
- (202) Labani, M. M.; Rezaee, R.; Saeedi, A.; Al Hinai, A. Evaluation of pore size spectrum of gas shale reservoirs using low pressure nitrogen adsorption, gas expansion and mercury porosimetry: A case study from the Perth and Canning Basins, Western Australia. *J. Pet. Sci. Eng.* **2013**, *112*, 7–16.
- (203) ALOthman, Z. A. A review: fundamental aspects of silicate mesoporous materials. *Materials* **2012**, *5* (12), 2874–2902.
- (204) Sun, S.; Liang, F.; Tang, L.; Wu, J.; Ma, C. Microstructural investigation of gas shale in Longmaxi Formation, Lower Silurian, NE Sichuan Basin, China. *Energy Explor. Exploit.* **2017**, *35* (4), 406–429.
- (205) Cychosz, K. A.; Thommes, M. Progress in the physisorption characterization of nanoporous gas storage materials. *Engineering* **2018**, *4* (4), 559–566.
- (206) Wei, M.; Zhang, L.; Xiong, Y.; Li, J.; Peng, P. Nanopore structure characterization for organic-rich shale using the non-local-density functional theory by a combination of N₂ and CO₂ adsorption. *Microporous Mesoporous Mater.* **2016**, *227*, 88–94.
- (207) Brunauer, S.; Emmett, P. H.; Teller, E. Adsorption of gases in multimolecular layers. *J. Am. Chem. Soc.* **1938**, *60* (2), 309–319.
- (208) Barrett, E. P.; Joyner, L. G.; Halenda, P. P. The Determination of Pore Volume and Area Distributions in Porous Substances. I. Computations from Nitrogen Isotherms. *J. Am. Chem. Soc.* **1951**, *73* (1), 373–380.
- (209) Joewondo, N. *Pore Structure of Micro- and Mesoporous Mudrocks Based on Nitrogen and Carbon Dioxide sorption*; Colorado School of Mines, Arthur Lakes Library, 2018.
- (210) Shi, K.; Santiso, E. E.; Gubbins, K. E. Current Advances in Characterization of Nano-porous Materials: Pore Size Distribution and Surface Area. In *Porous Materials: Theory and Its Application for Environmental Remediation*; Moreno-Piraján, J. C., Giraldo-Gutierrez, L., Gómez-Granados, F., Eds.; Springer International Publishing, 2021; pp 315–340.
- (211) Coasne, B.; Di Renzo, F.; Galarneau, A.; Pellenq, R. J. Adsorption of simple fluid on silica surface and nanopore: effect of surface chemistry and pore shape. *Langmuir* **2008**, *24* (14), 7285–7293.
- (212) Tian, Y.; Wu, J. A comprehensive analysis of the BET area for nanoporous materials. *AIChE J.* **2018**, *64* (1), 286–293.
- (213) Adamson, A. W.; Adamson, T. A.; Gast, A. P. *Physical Chemistry of Surfaces*; Wiley, 1997.
- (214) Ohba, T.; Kaneko, K. Internal surface area evaluation of carbon nanotube with GCMC simulation-assisted N₂ adsorption. *J. Phys. Chem. B* **2002**, *106* (29), 7171–7176.
- (215) Walton, K. S.; Snurr, R. Q. Applicability of the BET method for determining surface areas of microporous metal–organic frameworks. *J. Am. Chem. Soc.* **2007**, *129* (27), 8552–8556.
- (216) Bae, Y.-S.; Yazaydin, A. O.; Snurr, R. Q. Evaluation of the BET method for determining surface areas of MOFs and zeolites that contain ultra-micropores. *Langmuir* **2010**, *26* (8), 5475–5483.
- (217) Sing, K. The use of nitrogen adsorption for the characterisation of porous materials. *Colloids Surf., A* **2001**, *187*, 3–9.
- (218) Gómez-Gualdrón, D. A.; Moghadam, P. Z.; Hupp, J. T.; Farha, O. K.; Snurr, R. Q. Application of consistency criteria to calculate BET areas of micro- and mesoporous metal–organic frameworks. *J. Am. Chem. Soc.* **2016**, *138* (1), 215–224.
- (219) Gelb, L. D.; Gubbins, K. Characterization of porous glasses: Simulation models, adsorption isotherms, and the Brunauer–Emmett–Teller analysis method. *Langmuir* **1998**, *14* (8), 2097–2111.
- (220) Zou, J.; Fan, C.; Liu, X. Effects of Molecular Cross-Sectional Areas of Adsorbed Nitrogen on the Brunauer–Emmett–Teller Analysis for Carbon-Based Slit Pores. *Langmuir* **2020**, *36* (48), 14656–14665.
- (221) Rouquerol, J.; Llewellyn, P.; Rouquerol, F. Is the BET equation applicable to microporous adsorbents. *Stud. Surf. Sci. Catal.* **2007**, *160*, 49–56.
- (222) Coasne, B.; Gubbins, K. E.; Pellenq, R. J. M. A grand canonical Monte Carlo study of adsorption and capillary phenomena in nanopores of various morphologies and topologies: testing the BET and BJH characterization methods. *Particle & Particle Systems Characterization: Measurement and Description of Particle Properties and Behavior in Powders and Other Disperse Systems* **2004**, *21* (2), 149–160.
- (223) Mastalerz, M.; Hampton, L.; Drobnik, A.; Loope, H. Significance of analytical particle size in low-pressure N₂ and CO₂ adsorption of coal and shale. *Int. J. Coal Geol.* **2017**, *178*, 122–131.
- (224) Tesson, S. P.; Firoozabadi, A. Methane adsorption and self-diffusion in shale kerogen and slit nanopores by molecular simulations. *J. Phys. Chem. C* **2018**, *122* (41), 23528–23542.
- (225) Qi, R.; Ning, Z.; Wang, Q.; Huang, L.; Wu, X.; Cheng, Z.; Zhang, W. Measurements and modeling of high-pressure adsorption of CH₄ and CO₂ on shales. *Fuel* **2019**, *242*, 728–743.
- (226) Li, J.; Yin, J.; Zhang, Y.; Lu, S.; Wang, W.; Li, J.; Chen, F.; Meng, Y. A comparison of experimental methods for describing shale pore features—A case study in the Bohai Bay Basin of eastern China. *Int. J. Coal Geol.* **2015**, *152*, 39–49.
- (227) Wang, Y.; Shardt, N.; Lu, C.; Li, H.; Elliott, J. A. W.; Jin, Z. Validity of the Kelvin equation and the equation-of-state-with-capillary-pressure model for the phase behavior of a pure component under nanoconfinement. *Chem. Eng. Sci.* **2020**, *226*, 115839.
- (228) Webb, P. A.; Orr, C. *Analytical methods in fine particle technology*; Micromeritics Instrument Corp, 1997.

- (229) De Boer, J.; Lippens, B.; Linsen, B.; Broekhoff, J.; Van den Heuvel, A.; Osinga, T. J. Thet-curve of multimolecular N₂-adsorption. *J. Colloid Interface Sci.* **1966**, *21* (4), 405–414.
- (230) Lippens, B.; Linsen, B.; De Boer, J. Studies on pore systems in catalysts I. The adsorption of nitrogen; apparatus and calculation. *J. Catal.* **1964**, *3* (1), 32–37.
- (231) Kruk, M.; Jaroniec, M.; Sayari, A. Application of Large Pore MCM-41 Molecular Sieves To Improve Pore Size Analysis Using Nitrogen Adsorption Measurements. *Langmuir* **1997**, *13* (23), 6267–6273.
- (232) Kuila, U.; Prasad, M.; Derkowski, A.; McCarty, D. K. Compositional Controls on Mudrock Pore-Size Distribution: An Example from Niobrara Formation. In *SPE Annual Technical Conference and Exhibition*; Society of Petroleum Engineers, 2012.
- (233) Groen, J. C.; Peffer, L. A.; Pérez-Ramírez, J. Pore size determination in modified micro- and mesoporous materials. Pitfalls and limitations in gas adsorption data analysis. *Microporous Mesoporous Mater.* **2003**, *60* (1–3), 1–17.
- (234) Ravikovitch, P. I.; Haller, G. L.; Neimark, A. V. Density functional theory model for calculating pore size distributions: pore structure of nanoporous catalysts. *Adv. Colloid Interface Sci.* **1998**, *76*, 203–226.
- (235) Mastalerz, M.; Schimmelmann, A.; Drobniak, A.; Chen, Y. Porosity of Devonian and Mississippian New Albany Shale across a maturation gradient: Insights from organic petrology, gas adsorption, and mercury intrusion. *AAPG Bull.* **2013**, *97* (10), 1621–1643.
- (236) Thommes, M.; Kaneko, K.; Neimark, A. V.; Olivier, J. P.; Rodriguez-Reinoso, F.; Rouquerol, J.; Sing, K. S. Physisorption of gases, with special reference to the evaluation of surface area and pore size distribution (IUPAC Technical Report). *Pure Appl. Chem.* **2015**, *87* (9–10), 1051–1069.
- (237) Ojeda, M. L.; Esparza, J. M.; Campero, A.; Cordero, S.; Kornhauser, I.; Rojas, F. On comparing BJH and NLDFT pore-size distributions determined from N₂ sorption on SBA-15 substrata. *Phys. Chem. Chem. Phys.* **2003**, *5* (9), 1859–1866.
- (238) Ravikovitch, P. I.; Domhnaill, S. C. O.; Neimark, A. V.; Schueth, F.; Unger, K. K. Capillary Hysteresis in Nanopores: Theoretical and Experimental Studies of Nitrogen Adsorption on MCM-41. *Langmuir* **1995**, *11* (12), 4765–4772.
- (239) Ravikovitch, P. I.; Jagiello, J.; Tolles, D.; Neimark, A. V. Improved DFT methods for micropore size characterization of activated carbons: role of pore wall heterogeneity, 2001.
- (240) Ravikovitch, P. I.; Vishnyakov, A.; Russo, R.; Neimark, A. V. Unified Approach to Pore Size Characterization of Microporous Carbonaceous Materials from N₂, Ar, and CO₂ Adsorption Isotherms. *Langmuir* **2000**, *16* (5), 2311–2320.
- (241) Cimino, R. T.; Kowalczyk, P.; Ravikovitch, P. I.; Neimark, A. V. Determination of Isothermic Heat of Adsorption by Quenched Solid Density Functional Theory. *Langmuir* **2017**, *33* (8), 1769–1779.
- (242) Ravikovitch, P. I.; Vishnyakov, A.; Neimark, A. V. Density functional theories and molecular simulations of adsorption and phase transitions in nanopores. *Phys. Rev. E: Stat. Phys., Plasmas, Fluids, Relat. Interdiscip. Top.* **2001**, *64* (1), 011602.
- (243) Rosenfeld, Y. Free-energy model for the inhomogeneous hard-sphere fluid mixture and density-functional theory of freezing. *Phys. Rev. Lett.* **1989**, *63* (9), 980–983.
- (244) Ravikovitch, P. I.; Neimark, A. V. Density Functional Theory Model of Adsorption on Amorphous and Microporous Silica Materials. *Langmuir* **2006**, *22* (26), 11171–11179.
- (245) Neimark, A. V.; Lin, Y.; Ravikovitch, P. I.; Thommes, M. Quenched solid density functional theory and pore size analysis of micro-mesoporous carbons. *Carbon* **2009**, *47* (7), 1617–1628.
- (246) Roth, R.; Evans, R.; Lang, A.; Kahl, G. Fundamental measure theory for hard-sphere mixtures revisited: the White Bear version. *J. Phys.: Condens. Matter* **2002**, *14* (46), 12063–12078.
- (247) Sauer, E.; Gross, J. Classical Density Functional Theory for Liquid–Fluid Interfaces and Confined Systems: A Functional for the Perturbed-Chain Polar Statistical Associating Fluid Theory Equation of State. *Ind. Eng. Chem. Res.* **2017**, *56* (14), 4119–4135.
- (248) Wang, Y.; Jin, Z. Effect of pore size distribution on hydrocarbon mixtures adsorption in shale nanoporous media from engineering density functional theory. *Fuel* **2019**, *254*, 115650.
- (249) Li, Z.; Firoozabadi, A. Interfacial tension of nonassociating pure substances and binary mixtures by density functional theory combined with Peng–Robinson equation of state. *J. Chem. Phys.* **2009**, *130* (15), 154108.
- (250) Ravikovitch, P. I.; Neimark, A. V. Characterization of micro- and mesoporosity in SBA-15 materials from adsorption data by the NLDFT method. *J. Phys. Chem. B* **2001**, *105* (29), 6817–6823.
- (251) Weeks, J. D.; Chandler, D.; Andersen, H. C. Role of repulsive forces in determining the equilibrium structure of simple liquids. *J. Chem. Phys.* **1971**, *54* (12), 5237–5247.
- (252) Lucena, S. M.; Paiva, C. A. S.; Silvino, P. F.; Azevedo, D. C.; Cavalcante, C. L., Jr The effect of heterogeneity in the randomly etched graphite model for carbon pore size characterization. *Carbon* **2010**, *48* (9), 2554–2565.
- (253) Bardestani, R.; Patience, G. S.; Kaliaguine, S. Experimental methods in chemical engineering: specific surface area and pore size distribution measurements—BET, BJH, and DFT. *Can. J. Chem. Eng.* **2019**, *97* (11), 2781–2791.
- (254) Yang, K.; Lu, X.; Zhang, L.; Hu, W.; Zhang, X. Laboratory Simulation of Shale Gas Adsorption under Geological Conditions. In *Beijing: AAPG Hedberg Research Conference*; 2011; pp 9–12.
- (255) Firouzi, M.; Rupp, E. C.; Liu, C. W.; Wilcox, J. Molecular simulation and experimental characterization of the nanoporous structures of coal and gas shale. *Int. J. Coal Geol.* **2014**, *121*, 123–128.
- (256) Landers, J.; Gor, G. Y.; Neimark, A. V. Density functional theory methods for characterization of porous materials. *Colloids Surf., A* **2013**, *437*, 3–32.
- (257) Jin, Z.; Firoozabadi, A. Methane and carbon dioxide adsorption in clay-like slit pores by Monte Carlo simulations. *Fluid Phase Equilib.* **2013**, *360*, 456–465.
- (258) Gor, G. Y.; Thommes, M.; Cychosz, K. A.; Neimark, A. V. Quenched solid density functional theory method for characterization of mesoporous carbons by nitrogen adsorption. *Carbon* **2012**, *50* (4), 1583–1590.
- (259) Holmes, R.; Aljamaan, H.; Vishal, V.; Wilcox, J.; Kovscek, A. R. Idealized Shale Sorption Isotherm Measurements To Determine Pore Capacity, Pore Size Distribution, and Surface Area. *Energy Fuels* **2019**, *33* (2), 665–676.
- (260) Liu, J.; Wang, L.; Xi, S.; Asthagiri, D.; Chapman, W. G. Adsorption and Phase Behavior of Pure/Mixed Alkanes in Nanoslit Graphite Pores: An iSAFT Application. *Langmuir* **2017**, *33* (42), 11189–11202.
- (261) Yu, Y.-X.; Wu, J. Structures of hard-sphere fluids from a modified fundamental-measure theory. *J. Chem. Phys.* **2002**, *117* (22), 10156–10164.
- (262) Wertheim, M. S. Fluids with highly directional attractive forces. I. Statistical thermodynamics. *J. Stat. Phys.* **1984**, *35* (1), 19–34.
- (263) Chen, S. S.; Kreglewski, A. Applications of the Augmented van der Waals Theory of Fluids.: I. Pure Fluids. *Berichte der Bunsengesellschaft für physikalische Chemie* **1977**, *81* (10), 1048–1052.
- (264) Maddox, M. W.; Olivier, J. P.; Gubbins, K. E. Characterization of MCM-41 Using Molecular Simulation: Heterogeneity Effects. *Langmuir* **1997**, *13* (6), 1737–1745.
- (265) Sweatman, M. B.; Quirke, N. Characterization of Porous Materials by Gas Adsorption: Comparison of Nitrogen at 77 K and Carbon Dioxide at 298 K for Activated Carbon. *Langmuir* **2001**, *17* (16), 5011–5020.
- (266) Do, D. D.; Do, H. D. Adsorption of Quadrupolar, Diatomic Nitrogen onto Graphitized Thermal Carbon Black and in Slit-Shaped Carbon Pores. Effects of Surface Mediation. *Adsorpt. Sci. Technol.* **2005**, *23* (4), 267–288.
- (267) Potoff, J. J.; Siepmann, J. I. Vapor–liquid equilibria of mixtures containing alkanes, carbon dioxide, and nitrogen. *AIChE J.* **2001**, *47* (7), 1676–1682.

- (268) Yang, F.; Ning, Z.; Zhang, R.; Zhao, H.; Krooss, B. M. Investigations on the methane sorption capacity of marine shales from Sichuan Basin, China. *Int. J. Coal Geol.* **2015**, *146*, 104–117.
- (269) Dang, W.; Zhang, J.; Nie, H.; Wang, F.; Tang, X.; Wu, N.; Chen, Q.; Wei, X.; Wang, R. Isotherms, thermodynamics and kinetics of methane-shale adsorption pair under supercritical condition: Implications for understanding the nature of shale gas adsorption process. *Chem. Eng. J.* **2020**, *383*, 123191.
- (270) Zou, J.; Rezaee, R.; Liu, K. Effect of Temperature on Methane Adsorption in Shale Gas Reservoirs. *Energy Fuels* **2017**, *31*, 12081–12092.
- (271) Yang, F.; Xie, C.; Ning, Z.; Krooss, B. M. High-pressure methane sorption on dry and moisture-equilibrated shales. *Energy Fuels* **2017**, *31* (1), 482–492.
- (272) Rani, S.; Padmanabhan, E.; Prusty, B. K. Review of gas adsorption in shales for enhanced methane recovery and CO₂ storage. *J. Pet. Sci. Eng.* **2019**, *175*, 634–643.
- (273) Pang, Y.; Tian, Y.; Soliman, M. Y.; Shen, Y. Experimental measurement and analytical estimation of methane absorption in shale kerogen. *Fuel* **2019**, *240*, 192–205.
- (274) Chen, T.; Feng, X.-T.; Pan, Z. Experimental study of swelling of organic rich shale in methane. *Int. J. Coal Geol.* **2015**, *150*, 64–73.
- (275) Huang, L.; Khoshnood, A.; Firoozabadi, A. Swelling of Kimmeridge kerogen by normal-alkanes, naphthenes and aromatics. *Fuel* **2020**, *267*, 117155.
- (276) Ho, T. A.; Wang, Y.; Criscenti, L. J. Chemo-mechanical coupling in kerogen gas adsorption/desorption. *Phys. Chem. Chem. Phys.* **2018**, *20* (18), 12390–12395.
- (277) Yu, X.; Li, J.; Chen, Z.; Wu, K.; Zhang, L.; Yang, S.; Hui, G.; Yang, M. Determination of CH₄, C₂H₆ and CO₂ adsorption in shale kerogens coupling sorption-induced swelling. *Chem. Eng. J.* **2021**, *410*, 127690.
- (278) Huang, L.; Ning, Z.; Wang, Q.; Qi, R.; Cheng, Z.; Wu, X.; Zhang, W.; Qin, H. Kerogen deformation upon CO₂/CH₄ competitive sorption: Implications for CO₂ sequestration and enhanced CH₄ recovery. *J. Pet. Sci. Eng.* **2019**, *183*, 106460.
- (279) Pang, W.; Jin, Z. Revisiting methane absolute adsorption in organic nanopores from molecular simulation and Ono-Kondo lattice model. *Fuel* **2019**, *235*, 339–349.
- (280) Tang, X.; Ripepi, N.; Stadie, N. P.; Yu, L.; Hall, M. R. A dual-site Langmuir equation for accurate estimation of high pressure deep shale gas resources. *Fuel* **2016**, *185*, 10–17.
- (281) Chen, G.; Lu, S.; Zhang, J.; Xue, Q.; Han, T.; Xue, H.; Tian, S.; Li, J.; Xu, C.; Pervukhina, M. Keys to linking GCMC simulations and shale gas adsorption experiments. *Fuel* **2017**, *199*, 14–21.
- (282) Wang, S.; Feng, Q.; Zha, M.; Lu, S.; Qin, Y.; Xia, T.; Zhang, C. Molecular dynamics simulation of liquid alkane occurrence state in pores and slits of shale organic matter. *Petroleum Exploration and Development* **2015**, *42* (6), 844–851.
- (283) Jiang, W.; Lin, M. Molecular dynamics investigation of conversion methods for excess adsorption amount of shale gas. *J. Nat. Gas Sci. Eng.* **2018**, *49*, 241–249.
- (284) Fakher, S.; Imqam, A. A review of carbon dioxide adsorption to unconventional shale rocks methodology, measurement, and calculation. *SN Applied Sciences* **2020**, *2* (1), 5.
- (285) Belmabkhout, Y.; Frere, M.; De Weireld, G. High-pressure adsorption measurements. A comparative study of the volumetric and gravimetric methods. *Meas. Sci. Technol.* **2004**, *15* (5), 848.
- (286) Myers, A. L.; Monson, P. A. Physical adsorption of gases: the case for absolute adsorption as the basis for thermodynamic analysis. *Adsorption* **2014**, *20* (4), 591–622.
- (287) Aljamaan, H.; Al Ismail, M.; Koyseck, A. R. Experimental investigation and Grand Canonical Monte Carlo simulation of gas shale adsorption from the macro to the nano scale. *J. Nat. Gas Sci. Eng.* **2017**, *48*, 119–137.
- (288) Zhao, H.; Lai, Z.; Firoozabadi, A. Sorption Hysteresis of Light Hydrocarbons and Carbon Dioxide in Shale and Kerogen. *Sci. Rep.* **2017**, *7* (1), 16209.
- (289) Chareonsuppanimit, P.; Mohammad, S. A.; Robinson, R. L., Jr; Gasem, K. A. High-pressure adsorption of gases on shales: Measurements and modeling. *Int. J. Coal Geol.* **2012**, *95*, 34–46.
- (290) McCarty, R. D. *Thermophysical Properties of Helium-4 from 2 to 1500 K with Pressures to 1000 Atmospheres*; National Bureau of Standards Technical Note 631; U.S. Department of Commerce, 1972.
- (291) Span, R.; Wagner, W. A new equation of state for carbon dioxide covering the fluid region from the triple-point temperature to 1100 K at pressures up to 800 MPa. *J. Phys. Chem. Ref. Data* **1996**, *25* (6), 1509–1596.
- (292) Do, D.; Do, H.; Fan, C.; Nicholson, D. On the existence of negative excess isotherms for argon adsorption on graphite surfaces and in graphitic pores under supercritical conditions at pressures up to 10,000 atm. *Langmuir* **2010**, *26* (7), 4796–4806.
- (293) Li, J.; Wu, K.; Chen, Z.; Wang, K.; Luo, J.; Xu, J.; Li, R.; Yu, R.; Li, X. On the Negative Excess Isotherms for Methane Adsorption at High Pressure: Modeling and Experiment. *SPE J.* **2019**, *24* (06), 2504–2525.
- (294) Ross, D. J.; Bustin, R. M. Impact of mass balance calculations on adsorption capacities in microporous shale gas reservoirs. *Fuel* **2007**, *86* (17–18), 2696–2706.
- (295) Mohammad, S.; Fitzgerald, J.; Robinson, R. L., Jr; Gasem, K. A. Experimental uncertainties in volumetric methods for measuring equilibrium adsorption. *Energy Fuels* **2009**, *23* (5), 2810–2820.
- (296) Sircar, S.; Wang, C.-Y.; Lueking, A. D. Design of high pressure differential volumetric adsorption measurements with increased accuracy. *Adsorption* **2013**, *19* (6), 1211–1234.
- (297) Li, J.; Yan, X.; Wang, W.; Zhang, Y.; Yin, J.; Lu, S.; Chen, F.; Meng, Y.; Zhang, X.; Chen, X.; Yan, Y.; Zhu, J. Key factors controlling the gas adsorption capacity of shale: A study based on parallel experiments. *Appl. Geochem.* **2015**, *58*, 88–96.
- (298) Wang, J.; Wang, B.; Li, Y.; Yang, Z.; Gong, H.; Dong, M. Measurement of dynamic adsorption–diffusion process of methane in shale. *Fuel* **2016**, *172*, 37–48.
- (299) Yang, Y.; Liu, J.; Yao, J.; Kou, J.; Li, Z.; Wu, T.; Zhang, K.; Zhang, L.; Sun, H. Adsorption behaviors of shale oil in kerogen slit by molecular simulation. *Chem. Eng. J.* **2020**, *387*, 124054.
- (300) Sharma, A.; Namsani, S.; Singh, J. K. Molecular simulation of shale gas adsorption and diffusion in inorganic nanopores. *Mol. Simul.* **2015**, *41* (5–6), 414–422.
- (301) Zhang, W.; Feng, Q.; Wang, S.; Xing, X.; Jin, Z. CO₂-regulated octane flow in calcite nanopores from molecular perspectives. *Fuel* **2021**, *286*, 119299.
- (302) Zhan, S.; Su, Y.; Jin, Z.; Wang, W.; Cai, M.; Li, L.; Hao, Y. Molecular insight into the boundary conditions of water flow in clay nanopores. *J. Mol. Liq.* **2020**, *311*, 113292.
- (303) Wang, S.; Javadpour, F.; Feng, Q. Molecular dynamics simulations of oil transport through inorganic nanopores in shale. *Fuel* **2016**, *171*, 74–86.
- (304) Liu, Y.; Zhu, Y.; Li, W.; Xiang, J.; Wang, Y.; Li, J.; Zeng, F. Molecular simulation of methane adsorption in shale based on grand canonical Monte Carlo method and pore size distribution. *J. Nat. Gas Sci. Eng.* **2016**, *30*, 119–126.
- (305) Liu, Y.; Wilcox, J. Molecular simulation of CO₂ adsorption in micro- and mesoporous carbons with surface heterogeneity. *Int. J. Coal Geol.* **2012**, *104*, 83–95.
- (306) Jin, Z.; Firoozabadi, A. Effect of water on methane and carbon dioxide sorption in clay minerals by Monte Carlo simulations. *Fluid Phase Equilib.* **2014**, *382*, 10–20.
- (307) Chen, L.; Zuo, L.; Jiang, Z.; Jiang, S.; Liu, K.; Tan, J.; Zhang, L. Mechanisms of shale gas adsorption: Evidence from thermodynamics and kinetics study of methane adsorption on shale. *Chem. Eng. J.* **2019**, *361*, 559–570.
- (308) Zhu, H.; Ju, Y.; Huang, C.; Chen, F.; Chen, B.; Yu, K. Microcosmic gas adsorption mechanism on clay-organic nanocomposites in a marine shale. *Energy* **2020**, *197*, 117256.
- (309) Zhang, J.; Tang, Y.; He, D.; Sun, P.; Zou, X. Full-scale nanopore system and fractal characteristics of clay-rich lacustrine shale combining

FE-SEM, nano-CT, gas adsorption and mercury intrusion porosimetry. *Appl. Clay Sci.* **2020**, *196*, 105758.

(310) Tian, H.; Pan, L.; Zhang, T.; Xiao, X.; Meng, Z.; Huang, B. Pore characterization of organic-rich lower Cambrian shales in Qiannan depression of Guizhou province, Southwestern China. *Mar. Pet. Geol.* **2015**, *62*, 28–43.

(311) Huang, H.; Li, R.; Jiang, Z.; Li, J.; Chen, L. Investigation of variation in shale gas adsorption capacity with burial depth: Insights from the adsorption potential theory. *J. Nat. Gas Sci. Eng.* **2020**, *73*, 103043.

(312) Ji, W.; Song, Y.; Jiang, Z.; Wang, X.; Bai, Y.; Xing, J. Geological controls and estimation algorithms of lacustrine shale gas adsorption capacity: A case study of the Triassic strata in the southeastern Ordos Basin, China. *Int. J. Coal Geol.* **2014**, *134*, 61–73.

(313) Ji, W.; Song, Y.; Jiang, Z.; Chen, L.; Li, Z.; Yang, X.; Meng, M. Estimation of marine shale methane adsorption capacity based on experimental investigations of Lower Silurian Longmaxi formation in the Upper Yangtze Platform, south China. *Mar. Pet. Geol.* **2015**, *68*, 94–106.

(314) Feng, G.; Zhu, Y.; Wang, G. G.; Chen, S.; Wang, Y.; Ju, W. Supercritical methane adsorption on overmature shale: effect of pore structure and fractal characteristics. *Energy Fuels* **2019**, *33* (9), 8323–8337.

(315) Gai, H.; Li, T.; Wang, X.; Tian, H.; Xiao, X.; Zhou, Q. Methane adsorption characteristics of overmature Lower Cambrian shales of deepwater shelf facies in Southwest China. *Mar. Pet. Geol.* **2020**, *120*, 104565.

(316) Cao, Y.; Han, H.; Liu, H.-w.; Jia, J.-c.; Zhang, W.; Liu, P.-w.; Ding, Z.-g.; Chen, S.-j.; Lu, J.-g.; Gao, Y. Influence of solvents on pore structure and methane adsorption capacity of lacustrine shales: An example from a Chang 7 shale sample in the Ordos Basin, China. *J. Pet. Sci. Eng.* **2019**, *178*, 419–428.

(317) Li, J.; Zhou, S.; Gaus, G.; Li, Y.; Ma, Y.; Chen, K.; Zhang, Y. Characterization of methane adsorption on shale and isolated kerogen from the Sichuan Basin under pressure up to 60 MPa: Experimental results and geological implications. *Int. J. Coal Geol.* **2018**, *189*, 83–93.

(318) Fan, E.; Tang, S.; Zhang, C.; Guo, Q.; Sun, C. Methane sorption capacity of organics and clays in high-over matured shale-gas systems. *Energy Explor. Exploit.* **2014**, *32* (6), 927–942.

(319) Liu, D.; Yuan, P.; Liu, H.; Li, T.; Tan, D.; Yuan, W.; He, H. High-pressure adsorption of methane on montmorillonite, kaolinite and Illite. *Appl. Clay Sci.* **2013**, *85*, 25–30.

(320) Zhou, J.; Mao, Q.; Luo, K. H. Effects of moisture and salinity on methane adsorption in kerogen: a molecular simulation study. *Energy Fuels* **2019**, *33* (6), 5368–5376.

(321) Zhao, T.; Li, X.; Zhao, H.; Li, M. Molecular simulation of adsorption and thermodynamic properties on type II kerogen: Influence of maturity and moisture content. *Fuel* **2017**, *190*, 198–207.

(322) Zhao, T.; Li, X.; Ning, Z.; Zhao, H.; Li, M. Molecular simulation of methane adsorption on type II kerogen with the impact of water content. *J. Pet. Sci. Eng.* **2018**, *161*, 302–310.

(323) Hu, Y.; Devegowda, D.; Striolo, A.; Van Phan, A. T.; Ho, T. A.; Civan, F.; Sigal, R. Microscopic dynamics of water and hydrocarbon in shale-kerogen pores of potentially mixed wettability. *SPE J.* **2015**, *20* (01), 112–124.

(324) Huang, L.; Ning, Z.; Wang, Q.; Zhang, W.; Cheng, Z.; Wu, X.; Qin, H. Effect of organic type and moisture on CO₂/CH₄ competitive adsorption in kerogen with implications for CO₂ sequestration and enhanced CH₄ recovery. *Appl. Energy* **2018**, *210*, 28–43.

(325) Zhou, J.; Jin, Z.; Luo, K. H. Insights into recovery of multi-component shale gas by CO₂ injection: A molecular perspective. *Fuel* **2020**, *267*, 117247.

(326) Wang, Q.; Huang, L. Molecular insight into competitive adsorption of methane and carbon dioxide in montmorillonite: Effect of clay structure and water content. *Fuel* **2019**, *239*, 32–43.

(327) Zhou, B.; Xu, R.; Jiang, P. Novel molecular simulation process design of adsorption in realistic shale kerogen spherical pores. *Fuel* **2016**, *180*, 718–726.

(328) Collell, J.; Ungerer, P.; Galliero, G.; Yiannourakou, M.; Montel, F. o.; Pujol, M. Molecular simulation of bulk organic matter in type II shales in the middle of the oil formation window. *Energy Fuels* **2014**, *28* (12), 7457–7466.

(329) Liu, X.; Zhang, D. A review of phase behavior simulation of hydrocarbons in confined space: Implications for shale oil and shale gas. *J. Nat. Gas Sci. Eng.* **2019**, *68*, 102901.

(330) Martin, M. G.; Siepmann, J. I. Transferable Potentials for Phase Equilibria. I. United-Atom Description of n-Alkanes. *J. Phys. Chem. B* **1998**, *102* (14), 2569–2577.

(331) Kruk, M.; Jaroniec, M.; Ko, C. H.; Ryoo, R. Characterization of the Porous Structure of SBA-15. *Chem. Mater.* **2000**, *12* (7), 1961–1968.

(332) Rahmani Didar, B.; Akkutlu, I. Pore-Size Dependence of Fluid Phase Behavior and the Impact on Shale Gas Reserves. In *Unconventional Resources Technology Conference*; Society of Exploration Geophysicists, American Association of Petroleum, 2013; pp 1793–1814.

(333) Clarkson, C. R.; Haghshenas, B. Modeling of Supercritical Fluid Adsorption on Organic-Rich Shales and Coal. In *SPE Unconventional Resources Conference-USA*; Society of Petroleum Engineers, 2013.

(334) Chen, L.; Liu, K.; Jiang, S.; Huang, H.; Tan, J.; Zuo, L. Effect of adsorbed phase density on the correction of methane excess adsorption to absolute adsorption in shale. *Chem. Eng. J.* **2020**, 127678.

(335) Gensterblum, Y.; Van Hemert, P.; Billefont, P.; Battistutta, E.; Busch, A.; Krooss, B.; De Weireld, G.; Wolf, K.-H. European inter-laboratory comparison of high pressure CO₂ sorption isotherms II: Natural coals. *Int. J. Coal Geol.* **2010**, *84* (2), 115–124.

(336) Do, D.; Do, H. Adsorption of supercritical fluids in non-porous and porous carbons: analysis of adsorbed phase volume and density. *Carbon* **2003**, *41* (9), 1777–1791.

(337) Riewchotisakul, S.; Akkutlu, I. Y. Adsorption-enhanced transport of hydrocarbons in organic nanopores. *SPE J.* **2016**, *21* (06), 1960–1969.

(338) Wang, S.; Feng, Q.; Javadpour, F.; Hu, Q.; Wu, K. Competitive adsorption of methane and ethane in montmorillonite nanopores of shale at supercritical conditions: A grand canonical Monte Carlo simulation study. *Chem. Eng. J.* **2019**, *355*, 76–90.

(339) Azizian, S.; Eris, S.; Wilson, L. D. Re-evaluation of the century-old Langmuir isotherm for modeling adsorption phenomena in solution. *Chem. Phys.* **2018**, *513*, 99–104.

(340) Xiong, F.; Rother, G.; Gong, Y.; Moortgat, J. Reexamining supercritical gas adsorption theories in nano-porous shales under geological conditions. *Fuel* **2021**, *287*, 119454.

(341) Wang, J.; Wei, Y.; Ma, Z. Modified Dual-Site Langmuir Adsorption Equilibrium Models from A GCMC Molecular Simulation. *Appl. Sci.* **2020**, *10* (4), 1311.

(342) Builes, S.; Sandler, S. I.; Xiong, R. Isothermic heats of gas and liquid adsorption. *Langmuir* **2013**, *29* (33), 10416–10422.

(343) Masel, R. I. *Principles of Adsorption and Reaction on Solid Surfaces*; John Wiley & Sons, 1996; Vol. 3.

(344) Klemm, M.; Laverntovich, O. D. *Soft Matter Physics: An Introduction*; Springer Science & Business Media, 2007.

(345) Fowler, R. A Statistical Derivation of Langmuir's Adsorption Isotherm. In *Mathematical Proceedings of the Cambridge Philosophical Society*; Cambridge University Press, 1935; pp 260–264.

(346) Dang, W.; Zhang, J.; Wei, X.; Tang, X.; Chen, Q.; Li, Z.; Zhang, M.; Liu, J. Geological controls on methane adsorption capacity of Lower Permian transitional black shales in the Southern North China Basin, Central China: Experimental results and geological implications. *J. Pet. Sci. Eng.* **2017**, *152*, 456–470.

(347) Hu, H.; Hao, F.; Guo, X.; Dai, F.; Lu, Y.; Ma, Y. Investigation of methane sorption of overmature Wufeng-Longmaxi shale in the Jiaoshiba area, Eastern Sichuan Basin, China. *Mar. Pet. Geol.* **2018**, *91*, 251–261.

(348) Xi, Z.; Tang, S.; Wang, J.; Yi, J.; Guo, Y.; Wang, K. Pore structure and fractal characteristics of Niutitang shale from China. *Minerals* **2018**, *8* (4), 163.

(349) Chen, S.; Li, X.; Wang, Y.; Zuo, Z.; Han, Y., Evolution Mechanism of Material Composition–Pore Structure–Adsorption

Property in Marine Shale Based on Pyrolysis Experiments: A Typical Case of the Mesoproterozoic Xiamaling Formation. *Energy Fuels* **2021**, *35*, 1090

(350) Wang, Z.; Li, Y.; Guo, P.; Meng, W. Analyzing the adaption of different adsorption models for describing the shale gas adsorption law. *Chem. Eng. Technol.* **2016**, *39* (10), 1921–1932.

(351) Tang, X.; Ripepi, N.; Stadie, N. P.; Yu, L. Thermodynamic analysis of high pressure methane adsorption in Longmaxi shale. *Fuel* **2017**, *193*, 411–418.

(352) Lee, L. L. *Molecular Thermodynamics of Nonideal Fluids*; Butterworth-Heinemann, 2016.

(353) Ye, Z.; Chen, D.; Pan, Z.; Zhang, G.; Xia, Y.; Ding, X. An improved Langmuir model for evaluating methane adsorption capacity in shale under various pressures and temperatures. *J. Nat. Gas Sci. Eng.* **2016**, *31*, 658–680.

(354) Dubinin, M. The potential theory of adsorption of gases and vapors for adsorbents with energetically nonuniform surfaces. *Chem. Rev.* **1960**, *60* (2), 235–241.

(355) Hu, Q.; Zhang, Z. Application of Dubinin–Radushkevich isotherm model at the solid/solution interface: a theoretical analysis. *J. Mol. Liq.* **2019**, *277*, 646–648.

(356) Nguyen, C.; Do, D. The Dubinin–Radushkevich equation and the underlying microscopic adsorption description. *Carbon* **2001**, *39* (9), 1327–1336.

(357) Gil, A.; Grange, P. Application of the Dubinin–Radushkevich and Dubinin–Astakhov equations in the characterization of microporous solids. *Colloids Surf., A* **1996**, *113* (1–2), 39–50.

(358) Song, X.; Lü, X.; Shen, Y.; Guo, S.; Guan, Y. A modified supercritical Dubinin–Radushkevich model for the accurate estimation of high pressure methane adsorption on shales. *Int. J. Coal Geol.* **2018**, *193*, 1–15.

(359) Wang, Y.; Liu, L.; Sheng, Y.; Wang, X.; Zheng, S.; Luo, Z. Investigation of supercritical methane adsorption of overmature shale in Wufeng-Longmaxi Formation, southern Sichuan Basin, China. *Energy Fuels* **2019**, *33* (3), 2078–2089.

(360) Ambrose, R. J.; Hartman, R. C.; Diaz-Campos, M.; Akkutlu, I. Y.; Sondergeld, C. H. Shale gas-in-place calculations part I: new pore-scale considerations. *SPE J.* **2012**, *17* (01), 219–229.

(361) Wang, Y.; Zhu, Y.; Liu, S.; Zhang, R. Methane adsorption measurements and modeling for organic-rich marine shale samples. *Fuel* **2016**, *172*, 301–309.

(362) Clarkson, C.; Bustin, R.; Levy, J. Application of the mono/multilayer and adsorption potential theories to coal methane adsorption isotherms at elevated temperature and pressure. *Carbon* **1997**, *35* (12), 1689–1705.

(363) Hao, S.; Chu, W.; Jiang, Q.; Yu, X. Methane adsorption characteristics on coal surface above critical temperature through Dubinin–Astakhov model and Langmuir model. *Colloids Surf., A* **2014**, *444*, 104–113.

(364) Riewchotisakul, S.; Akkutlu, I. Y. Adsorption Enhanced Transport of Hydrocarbons in Organic Nanopores. In *SPE Annual Technical Conference and Exhibition*; Society of Petroleum Engineers, 2015.

(365) Ono, S.; Kondo, S. Molecular Theory of Surface Tension in Liquids. In *Structure of Liquids/Struktur der Flüssigkeiten*; Springer, 1960; pp 134–280.

(366) Aranovich, G.; Donohue, M. Vapor adsorption on microporous adsorbents. *Carbon* **2000**, *38* (5), 701–708.

(367) Aranovich, G. L.; Donohue, M. D. Adsorption of supercritical fluids. *J. Colloid Interface Sci.* **1996**, *180* (2), 537–541.

(368) Aranovich, G.; Donohue, M. Predictions of multilayer adsorption using lattice theory. *J. Colloid Interface Sci.* **1997**, *189* (1), 101–108.

(369) Aranovich, G. L.; Donohue, M. D. Adsorption isotherms for microporous adsorbents. *Carbon* **1995**, *33* (10), 1369–1375.

(370) Benard, P.; Chahine, R. Modeling of high-pressure adsorption isotherms above the critical temperature on microporous adsorbents: application to methane. *Langmuir* **1997**, *13* (4), 808–813.

(371) Bi, H.; Jiang, Z.; Li, J.; Xiong, F.; Li, P.; Chen, L. Ono–Kondo model for supercritical shale gas storage: A case study of Silurian Longmaxi shale in southeast Chongqing, China. *Energy Fuels* **2017**, *31* (3), 2755–2764.

(372) Bi, H.; Jiang, Z.; Li, J.; Li, P.; Chen, L.; Pan, Q.; Wu, Y. The Ono–Kondo model and an experimental study on supercritical adsorption of shale gas: A case study on Longmaxi shale in southeastern Chongqing, China. *J. Nat. Gas Sci. Eng.* **2016**, *35*, 114–121.

(373) Qin, C.; Jiang, Y.; Luo, Y.; Zhou, J.; Liu, H.; Song, X.; Li, D.; Zhou, F.; Xie, Y. Effect of supercritical CO₂ saturation pressures and temperatures on the methane adsorption behaviours of Longmaxi shale. *Energy* **2020**, *206*, 118150.

(374) Rangarajan, B.; Lira, C. T.; Subramanian, R. Simplified local density model for adsorption over large pressure ranges. *AIChE J.* **1995**, *41* (4), 838–845.

(375) Kong, S.; Huang, X.; Li, K.; Song, X. Adsorption/desorption isotherms of CH₄ and C₂H₆ on typical shale samples. *Fuel* **2019**, *255*, 115632.

(376) Wang, C.; Liu, Y.; Gao, Y. Comparison of the Absolute Adsorption of CH₄, n-C₄H₁₀, and CO₂ on Shale. *Energy Fuels* **2020**, *34* (4), 4466–4473.

(377) Zhang, J.; Tang, Y.; Chen, D. Prediction of methane adsorption content in continental coal-bearing shale reservoir using SLD model. *Pet. Sci. Technol.* **2019**, *37* (15), 1839–1845.

(378) Wang, X.; Sheng, J. J. Understanding oil and gas flow mechanisms in shale reservoirs using SLD–PR transport model. *Transp. Porous Media* **2017**, *119* (2), 337–350.

(379) Jiang, Z.; Zhao, L.; Zhang, D. Study of adsorption behavior in shale reservoirs under high pressure. *J. Nat. Gas Sci. Eng.* **2018**, *49*, 275–285.

(380) Peng, D.-Y.; Robinson, D. B. A New Two-Constant Equation of State. *Ind. Eng. Chem. Fundam.* **1976**, *15* (1), 59–64.

(381) Gasem, K.; Gao, W.; Pan, Z.; Robinson, R., Jr A modified temperature dependence for the Peng–Robinson equation of state. *Fluid Phase Equilib.* **2001**, *181* (1–2), 113–125.

(382) Chen, J. H.; Wong, D. S. H.; Tan, C. S.; Subramanian, R.; Lira, C. T.; Orth, M. Adsorption and desorption of carbon dioxide onto and from activated carbon at high pressures. *Ind. Eng. Chem. Res.* **1997**, *36* (7), 2808–2815.

(383) Fitzgerald, J.; Sudibandriyo, M.; Pan, Z.; Robinson, R., Jr; Gasem, K. Modeling the adsorption of pure gases on coals with the SLD model. *Carbon* **2003**, *41* (12), 2203–2216.

(384) Fitzgerald, J. E. *Adsorption of Pure and Multi-Component Gases of Importance to Enhanced Coalbed Methane Recovery: Measurements and Simplified Local Density Modeling*. Dissertation, Oklahoma State University, 2005.

(385) Wu, X.-J.; Ning, Z.-F.; Cheng, Z.-L.; Wang, Q.; Qi, R.-R.; Huang, L.; Zhang, W.-T. Simplified local density model for gas adsorption in cylindrical carbon pores. *Appl. Surf. Sci.* **2019**, *491*, 335–349.

(386) Chen, Y.; Jiang, S.; Zhang, D.; Liu, C. An adsorbed gas estimation model for shale gas reservoirs via statistical learning. *Appl. Energy* **2017**, *197*, 327–341.

(387) Meng, M.; Zhong, R.; Wei, Z. Prediction of methane adsorption in shale: Classical models and machine learning based models. *Fuel* **2020**, *278*, 118358.

(388) Meng, M.; Qiu, Z.; Zhong, R.; Liu, Z.; Liu, Y.; Chen, P. Adsorption characteristics of supercritical CO₂/CH₄ on different types of coal and a machine learning approach. *Chem. Eng. J.* **2019**, *368*, 847–864.